

**EXCITON DYNAMICS IN NANOMETER SIZE POLYOXOTITANATE
CLUSTERS AND EXCITED STATES DYNAMICS OF P3HT FILMS IN
PROXIMITY TO METALLIC NANOSTRUCTURES**

By Jianhua Bao

A dissertation submitted to the Graduate School-Newark

Rutgers, The State University of New Jersey

in partial fulfillment of requirements

for the degree of

Doctor of Philosophy

Graduate Program in Chemistry

Written under the direction of

Professor Piotr Piotrowiak

And approved by

Newark, New Jersey

October, 2015

© 2015

Jianhua Bao

ALL RIGHTS RESERVED

ABSTRACT OF THE THESIS

Exciton Dynamics in Nanometer Size Polyoxotitanate Clusters and Excited States

Dynamics of P3HT Films in Proximity to Metallic Nanostructures

By Jianhua Bao

Thesis director: Professor Piotr Piotrowiak

The dissertation consists of two sections, each of which addresses the excited state dynamics, charge separation and recombination in two classes of nano-structured materials. While the materials are different, the underlying theoretical background, as well as the experimental techniques which were employed in the course of these investigations is closely related.

Project 1: A series of crystalline nanometer size polyoxotitanate cluster offers a good opportunity to study the structure-dynamics correlations. Its core-ligand interface, the presence of non-equivalent metal sites and quantum size supply us attractive, experimentally and theoretically tractable models to study exciton dynamics and charge carrier localization. The charge-transfer (CT), exciton dynamics and electronic structure of Ti/O clusters were studied by comprehensive approaches including ultrafast time-dependent spectroscopy, fast pulse radiolysis, ground state spectroscopy and theoretical calculations. The factors which can influence exciton dynamics are discussed individually, e.g., cluster size, surface modification, and solvent polarity. Through dynamics study of exciton in Ti/O cluster we have better understanding about the

reactions occurring on the TiO_2 nanoparticles, which serve as a potent photocatalyst for hydrogen production and pollutant remediation.

Project 2: Surface enhanced fluorescence (SEF) of P3HT was measured in a tailored environment from silver surface with and without gold nanocones on it, and rough gold surface (Klarite substrate). The accelerated fluorescence dynamics and emission spectra were recorded through Kerr-gated ultrafast fluorescence microscope with 100 fs resolution. Competitive radiative, electron transfer processes are studied in various thickness P3HT films; and enhanced interchain electronic energy transfer was confirmed by fluorescence anisotropy measurements.

ACKNOWLEDGEMENTS

I would like to express my deepest gratitude to my adviser Dr. Piotrowiak for his full support, expert guidance, understanding and encouragement throughout my study and research. Without his unlimited patience and timely wisdom, I could not have finished my research and thesis work.

I would like to acknowledge my committee members, Prof. John Miller, Prof. Phillip Husky, Prof. Pavanello for spending their time reading and correcting my thesis, and for their helpful advice and encouragement.

I would like to thank Prof. Philip Coppens and Prof. Jason B. Benedict from Buffalo University to supply the cluster samples for us to study their optical and dynamic properties.

I would like to thank Prof. Victor Batista and Dr. Robert Snoeberger from Yale University for their calculation work on Ti17cat4 cluster.

I would also like to thank all the chemistry faculty and staff for their help over the past six years. My thanks also go to the former and current members in the Piotrowiak group, and especially I would like to thank Dr. Lars Gundlach and Dr. Zhihao Yu for their prompt problem solving suggestions.

Finally, I would like to thank my family, especially my father who teach me the principles to conduct myself, my son who give me an opportunity to rediscover and correct myself, my husband, my parents in law and my sisters who always give me the understanding and support. You are truly the most important part of my life.

Table of Contents

Abstract of Thesis	ii
Acknowledgement	iv
Table of Contents	v
List of Tables	x
List of Figures and Schemes	xi
Chapter 1. Introduction to Exciton Dynamics in Nanoscale Materials	1
1.1 Introduction of exciton	1
1.2 Size confinement on exciton in QDs	3
1.2.1 Size-tunable band gap energy, exciton size	3
1.2.2 Size dependence of exciton binding energy in QDs	6
1.2.3 Exciton dynamics of QDs	7
1.3 Size confinement on exciton in conjugated polymer	9
1.3.1 Conjugated polymers	9
1.3.2 Size-tunable band gap energy	10
1.3.3 Localization and delocalization of exciton	11
1.3.4 Exciton binding energy	13
1.3.5 Exciton diffusion	13
1.4 The approaches used to study exciton dynamics	15
1.5 References	18
Chapter 2. Techniques and Instrumentation	22
2.1 Materials and preparation procedures	22
2.1.1 Ti/O clusters preparations	22
2.1.2 P3HT films preparations on Klarite	23
2.1.3 P3HT film with gold nanocones on silvered slide	23
2.2 Techniques and instruments	23
2.2.1 Steady state absorption	23
2.2.2 Fluorescence spectroscopy	24
2.2.3 Raman micro-spectroscopy	24
2.2.4 Scanning electron microscope (SEM)	24

2.2.5 Pump-probe transient absorption measurement	24
2.2.4 Pulse radiolysis measurement	26
2.2.7 Femtosecond Kerr-gated fluorescence microscopy	28
2.2.8 Chemical quantum calculation	30
2.3 References	32
 Chapter 3. Exciton and Excess Electrons in Nanometer Size Molecular	 33
Polyoxotitanate Cluster Ti17	
3.1 Introduction	33
3.2 Results and discussion	37
3.2.1 Steady state absorption	37
3.2.2 Fluorescence and Raman spectra of Ti17	38
3.2.3 Raman spectra of Ti17	39
3.2.4 Pump-probe transient absorption measurement	42
3.2.5 Pulse radiolysis measurement	45
3.2.6 Pump-probe transient dynamics measurement	50
3.3 Conclusions	53
3.4 References	56
 Chapter 4. Charge Transfer and Hole Hopping in Ti17cat4	 59
4.1 Introduction	59
4.2 Results and discussions	62
4.2.1 Raman spectrum of Ti17cat4	62
4.2.2 UV-Vis spectrum	63
4.2.3 The ligand-core electronic coupling	64
4.2.4 Transient absorption spectrum of Ti17cat4	66
4.2.5 Dynamic depolarization measurements on Ti17cat4 in acetonitrile	68
4.2.6 Quantum mechanics calculation of hole hopping dynamics	73
4.2.7 The discussion on dynamics of electron transfer, relaxation and recombination	77
4.3 Conclusions	80
4.4 References	82
 Chapter 5. Exciton Dynamics in Molucular Ti6 Cluster	 84
5.1 Introduction	84
5.2 Results and discussions	85

5.2.1 UV-Vis spectrum	85
5.2.2 Emission spectrum	86
5.2.3 Raman spectrum	89
5.2.4 The transient absorption spectrum of Ti6	91
5.2.5 The transient absorption dynamics at different probe wavelengths	94
5.2.6 Excitation power dependence of transient absorption dynamics	96
5.2.7 Calculations on the Ti6 cluster	98
5.3 Conclusions	99
5.4 Reference	101

Chapter 6. Enhancement of Fluorescence of P3HT Films on Nanostructured Gold Substrates 103

6.1 Introduction	103
6.2 Results and discussion	109
6.2.1 P3HT film on glass	109
6.2.1.1 The ground state absorption spectrum	109
6.2.1.2 The fluorescence decay profiles of varying thickness P3HT films on glass	111
6.2.2 P3HT film on smooth silver surface	112
6.2.2.1 The steady-state absorption spectrum	112
6.2.2.2 The fluorescence dynamics of P3HT film on flat silver surface	113
6.2.2.3 The competition process between radiative and electron transfer	115
6.2.3 P3HT film with gold nanocone array (Au NCs) on silvered glass	117
6.2.3.1 SEM image of gold NC/P3HT/silver	117
6.2.3.2 Time-resolved fluorescence dynamics of 30 nm P3HT with and without gold NCs	117
6.2.3.3 Time-resolved fluorescence dynamics of 50 nm P3HT with and without gold NCs	120
6.2.3.4 Fluorescence Anisotropy Measurement	123
6.2.3.5 Time-Resolved Fluorescence Spectra	126
6.2.4 Results and discussion on the fluorescence enhancement of P3HT film on Klarite	129
6.2.4.1 SEM Results	130
6.2.4.2 Fluorescence lifetime measurement results and discussion	130
6.2.4.3 Dependence of the fluorescence enhancement of film thickness	133
6.2.4.4 Time-resolved fluorescence spectra of P3HT on Klarite	134
6.2.4.5 Time-Resolved Fluorescence Images	137
6.2.4.6 Comparison of enhanced fluorescence on two substrates	138
6.3 Conclusions	140
6.4 References	142

List of Tables

Table 3-1. Raman mode comparison	40
Table 3-2. Time constants of exciton decay of Ti17 cluster	50
Table 4-1. Constant of acetonitrile and propylene carbonate	66
Table 4-2. Time constants of transient dynamics at 495 and 530 nm	72
Table 4-3. Multiexponential kinetic parameters for the charge relaxation & recombination measured at different wavelengths and at parallel vs. perpendicular pump-probe polarization.	80
Table 4-4. Multiexponential kinetic parameters for the charge relaxation & recombination at a longer time scale	80
Table 5-1. Frequency of emission peaks and frequency difference	88
Table 5-2. Assignment of the Raman peaks	90
Table 5-3. Exciton decay parameters measurement for Ti6 in dibutyl ether, excitation at 300 nm	94
Table 6-1. P3HT films on different metallic substrates	107
Table 6-2. Decay parameters of fluorescence dynamics of 30 nm P3HT film on silver	114
Table 6-3. Time constants for 30 nm P3HT film with and without Au NCs	119
Table 6-4. A double exponential function fitting parameters for emission of P3HT film with and without Au NCs on it	123
Table 6-5. The fitting parameters for polarization-sensitive measurement	126
Table 6-6. The fitting parameters for 20 nm P3HT film on Klarite	131
Table 6-7. Time constant of 4 layers P3HT film	134
Table 6-8. Fluorescence kinetics of P3HT film on Klarite	135

List of Figures and Schemes

Scheme 1-1. Excitons in a semiconductor and an organic molecule	1
Figure 1-1. Illustration of the quantum confinement effect in different systems ranging from atoms to clusters and finally to bulk materials	3
Figure 1-2. Size-tunable excitation energy for various QD materials	5
Figure 1-3. Exciton binding energy	7
Figure 1-4. Molecular orbital picture for confined systems	10
Figure 1-5. The size dependence of exciton energy versus confinement length of a range of organic materials	11
Figure 1-6. Typical conformations of a 100-segment homopolymer generated by Monte Carlo simulations	12
Scheme 2-1. Transient absorption measurement setup	26
Scheme 2-2. The layout of the LEAF at Brookhaven national lab	27
Scheme 2-3. Setup for the Kerr-gated fluorescence microscopy	30
Figure 3-1. Two representation of the Ti17 cluster	34
Figure 3-2. Tentative energy level diagrams of: (a) The neutral Ti17 polyoxotitanate cluster and (b) the Ti17 ⁻ reduced species carrying the excess electron	36
Figure 3-3. The UV-Vis spectrum of Ti17 in dibutyl ether	38
Figure 3-4. Room temperature fluorescence spectrum of Ti17 in ditutyl ether	39
Figure 3-5. Raman spectrum of solid Ti17 (black) and Ti17cat4 (red)	39
Figure 3-6. Calculated Raman (a) and IR (b) spectra of the isopropoxide anion (blue) and the oxo isopropoxyl radical (red). Calculations were performed at the B#LYP DFT level (Spartan'10) without frequency scaling.	41

Figure 3-7. Femtosecond pump-probe transient absorption spectra of the Ti17* excited state in (a) benzonitrile, $\epsilon = 25.6$; (b) dibutyl ether, $\epsilon = 4.3$ 44

Figure 3-8. (a) Absorption spectra of the **Ti17^{•+}** species at different delay times obtained by picosecond pulse radiolysis in benzonitrile. (b) Gaussian (green) and stretched Gaussian (blue) line shape fitting of the **Ti17^{•+}** absorption band obtained at 50 ns delay. The solid red line is the sum of the three Gaussian functions calculated only at the frequencies of the experimental data. 48

Figure 3-9. Overlaid normalized transients collected at several wavelengths from 550 to 680 nm showing homogeneous decay kinetics. (b) Decay of the excited state of Ti17 in dibutyl ether monitored at 680 nm fitted with a biexponential function. (c) IR transient responses of the Ti17 cluster and anatase film 52

Figure 4-1. Structure of Ti17cat4 cluster 60

Figure 4-2. From left to right: (a) the mononuclear $[\text{Ti}(\text{cat})_3]^{2-}$ complex; (b) Ti17cat4 polyoxotitanate cluster; (c) schematic representation of a dye-sensitized TiO_2 nanoparticle. 61

Scheme 4-1. Possible sequential events on Ti17cat4 after excitation 62

Scheme 4-2. Dynamic depolarization measurement 69

Figure 4-3. UV-Vis spectrum of Ti17cat4, Ti17 and catechol in acetonitrile 64

Figure 4-4. Transient absorption spectrum in acetonitrile 67

Figure 4-5. Transient dynamics measured at long wavelengths 69

Figure 4-6. Depolarization measurements at short wavelengths in acetonitrile 72

Scheme 4-2 Catechol modified cluster 74

Figure 4-7. Time-dependent occupation of the photogenerated hole on each of the four catechol adsorbates during the first 40 ps of dynamics. The hole was initially localized on catechol 1. 75

Figure 4-8. Ti17cat4 in acetonitrile : (a) transient dynamics in 25 ps time window, (b) dynamics in 200 ps time window	79
Figure 5-1. Structure of Ti6 cluster	84
Figure 5-2. UV-Vis spectra of Ti6 (black) and Ti17 (red) in acetonitrile at room temperature	86
Figure 5-3. Fluorescence spectrum of Ti6 in acetonitrile at room temperature	88
Figure 5-4. Low temperature fluorescence of Ti6 in acetonitrile	89
Figure 5-5. Raman spectra of Ti6	90
Figure 5-6. Transient absorption spectrum of Ti6 in (a) visible range and (b) near IR rang	91
Figure 5-7. Potential energy description of an electron-transfer reaction with $\Delta G^0=0$	92
Figure 5-8. The electronic absorption diagram of Ti6	93
Figure 5-9. Absorption dynamics of Ti6 at 530, 600, 900 nm in (a) 30 ps time window; and (b) the absorption dynamics at 600 nm in 100 ps time window	95
Figure 5-10. The excitation power dependence of transient dynamics at different probe wavelengths : (a)the normalized dynamics of 600 and 650 nm at 50 and 200 μ W pump power, in 30 and 100 ps time window; (b)the transient dynamics of 530, 600 and 900 nm at 300 μ W pump power	97
Figure 5-10. The calculated HOMO and LUMO obitals of Ti6 cluster	100
Scheme 6-1. Schematic diagrams: (a) flat metal surface plasmon; (b) localized plasmon of gold nanoparticle	103
Figure 6-1. The structure of P3HT	105
Scheme 6-2. Schematic diagram of P3HT film with gold nanocone on silver	108
Figure 6-2. SEM image of Klarite	108
Figure 6-3. The SEM image of P3HT film on glass	109

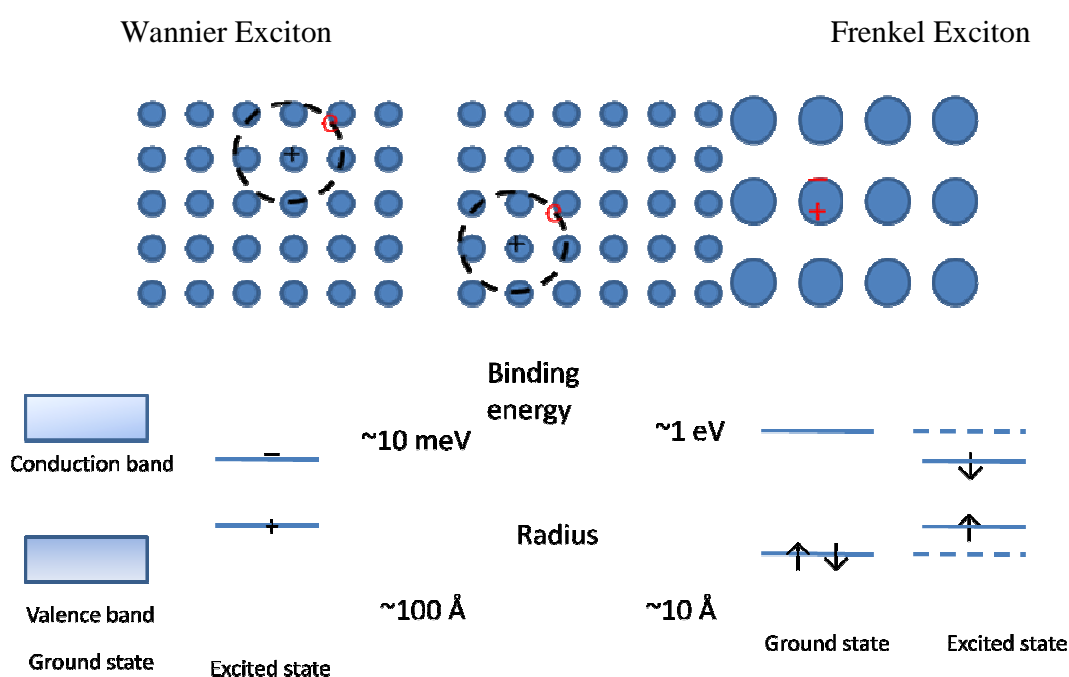
Figure 6-4. The steady-state absorption (a) and fluorescence spectrum (b) of P3HT in chlorobenzene and a 50 nm P3HT on glass	110
Figure 6-5. Time-resolved fluorescence: (a) 30 and (b) 10 nm P3HT films on glass	112
Figure 6-6. Absorption spectrum of P3HT on silvered glass and with gold nanocone	113
Figure 6-7. Fluorescence dynamics of (a) 30 and (b) 10nm P3HT film on silver	114
Figure 6-8. Simulated relative radiative and quenching rate as a function of distance between P3HT and silver film	116
Figure 6-9. The SEM image of the top view of gold nanocone and Al ₂ O ₃ template	117
Figure 6-10. The fluorescence decays of 30 nm P3HT film on silver with and without 100 nm Au NC on it	119
Figure 6-11. The fluorescence decay of 50 nm P3HT film on gold film with (a) and without (b) 100 nm Au NC on it, the comparison of original fluorescence data (c) and the normalized emission decays (d)	123
Figure 6-12. Anisotropy measurement of 50 nm P3HT film with Au NC on silver modified glass	126
Figure 6-13. (a) Time-resolved fluorescence spectrum of P3HT with Au NC at different time; (b) the decay kinetics based on the time-resolved emission spectra	127
Figure 6-14. Simplified Jablonski diagrams: (a) Standard fluorescence, (b) Surface-enhanced fluorescence in slow dynamic regime, (c) Surface-enhanced fluorescence in fast dynamic regime	128
Figure 6-15. The SEM image of the cross-section of Klarite with P3HT film on it	130
Figure 6-16. The fluorescence time profile of P3HT on Klarite 2a, the normalized time profile with fitting parameters	132
Figure 6-17. Fluorescence decay profiles of various P3HT films on Klarite	134
Figure 6-18. (a) Time-resolved fluorescence spectrum of P3HT on Klarite at different times; (b) the decay kinetics based on the emission spectra	135
Figure 6-19. The microscope image of P3HT on Klarite at time: (a) 0 ps;	

(b) 2 ps and (c) the difference image	137
Figure 6-20. Comparison of emission spectrum of P3HT on different substrates	139
Figure 6-21. The comparison of fluorescence kinetics of P3HT film on (a) silver and (b) Klarite	140

Chapter 1. Introduction to Excitons in Nanoscale Materials

1.1 Exciton

An exciton is an electrically neutral quasi-particle which is a bound state of an electron and hole through the electrostatic Coulomb force. Excitons exist in insulators, semiconductors and some liquids. Numerous studies on excitons have been carried in polymers, organic molecules, and semiconductors.



Scheme 1. Excitons in a semiconductor and an organic molecule

Excitons formed in different materials are characterized by different features. Wannier and Frenkel exciton models are used to describe the excitons created in semiconductors and molecules, respectively, as shown in Scheme 1. An exciton in a semiconductor has relatively large exciton diameter and weak binding energy, the electron-hole pair easily dissociates into free carriers, and thus it is relevant to photovoltaic and solar cell

devices.[1] In contrast to Wannier exciton, the Frenkel exciton formed in a molecule has strong binding energy and short exciton radius. It is difficult for a molecular exciton to dissociate. The electron-hole pair recombines and emits photon, which makes the excitons play a critical role in light-emitter device (LED) and be ideal to laser media[2]. The exciton state as an energy form is efficiently used in photosynthetic light harvesting by the photosynthetic complex[3], and it also has been converted into current in solar cells based on QDs[4] and organic semiconductors[5]. A deciding property of exciton in nanoscale systems is that the exciton size is dictated not only by the electron-hole Coulomb interaction, but by the physical dimensions of the material or the arrangement of distinct building blocks. The exciton and excited state formation, the energy transporting and other influential processes are critical for energy conversion in a nanosystem.

Currently inorganic and organic semiconductors are mostly employed in the nanoscale solar cell systems. The special advantages of using nanoscale QDs and polymers are their tunable visible response, the relative alignment of the energy bands at a semiconductor heterojunction, i.e. the band offset, which modulate the charge transfer in heteromaterials and generate multiple charge carriers with a single photon [6]. The electronic states of nanoparticles are different from the excitons in bulk materials, and molecules. The excited nanoparticle or conjugated polymer presents one unique class of an exciton that can be thought as either molecular excitation or a confined bulk-type exciton. Electronic spectroscopy is very sensitive to the electronic structures of materials and provides us with an insight into the collective absorption and redistribution of electrons and energy. Hence, recent effort to synthesize the diverse nanostructures with

well defined structures expands the possibility of developing new strategies for light conversion. Nanoscale devices are the promising ones including light-emitting devices and organic solar cells.

1.2 Exciton in QDs

1.2.1 The size-confinement of excitons in QDs

The behavior of excitons in QDs and conjugated polymer will change with the size and structure of the system, and the environment of the exciton existing. Among the influential elements the size effect plays the most significant role in exciton dynamics. When the size of the semiconductor decreases to nanoscale, the periodic arranged atoms are strongly coupled, which results in a high density delocalized orbitals in the valence and conduction bands as shown in the Figure 1 [6].

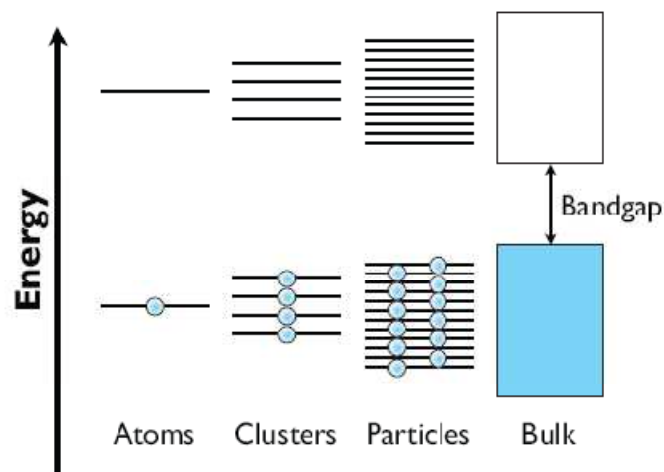


Figure 1. Illustration of the quantum confinement effect in different systems ranging from atoms to clusters and finally to bulk materials. [7]

In early 1980 researchers predicted that QDs should possess discrete energy levels, the electronic properties are more like molecules than bulk semiconductors[8, 9]. The difference can be seen from the band gap energy increasing with size diminishing. This prediction was proved through other experimental work[10, 11]. Therefore, the shape and size will strongly influence the dynamics of electronic state which governs the photophysical behavior of nanoscale systems. The size not only influences band gap energy but the exciton size, the electron-hole binding energy and exchange interaction.

$$E_{g,\text{effective}}(R) = E_g(\infty) + \frac{\hbar^2 \pi^2}{2R^2} \left(\frac{1}{m_e} + \frac{1}{m_h} \right) - \frac{1.8e^2}{\epsilon R} \quad (1)$$

The band gap energy change with size can be accounted for in eq 1 with the particle-in-a-sphere model for a sphere particle with radius R. The first term in right hand side is the bulk bandgap; the second term shows the effective bandgap is inversely proportional to the square of the particle radius; and the third term is the Columbic attraction between electron and hole which results in a decrease in the bandgap with increasing particle radius. However, quantum confinement also alters the density of states (DOS) toward a more discrete distribution. The DOS variation can explain the size-dependence of electron-phonon coupling and carrier relaxation.

Size dependence of spectroscopic properties of nanoparticles has been great interest for more than half a century[11]. The size tunable property in QDs is ascribed to the confinement of exciton in nanocrystal considerably smaller than in bulk, especially when the particle size becomes comparable to or smaller than the Bohr exciton radius. For example the exciton Bohr radius (the most probable radial distance of electron) of PbS is

18 nm, the corresponding bandgap is 0.4 eV, while the exciton energies in ~ 1.3 and ~ 3.5 nm PbS QDs are 1.5 and 0.7 eV[12]. The Bohr radius of a semiconductor exciton provides a reference as to the exciton size in the bulk. The exciton transition energy scaling with the size is observed for QDs [46-49], conjugated oligomers and polymers [30,45]. The size dependence of exciton transition energies for a range of QDs particles is displayed in Figure 2. The bandgap is the energy difference between HOMO and LUMO orbitals.

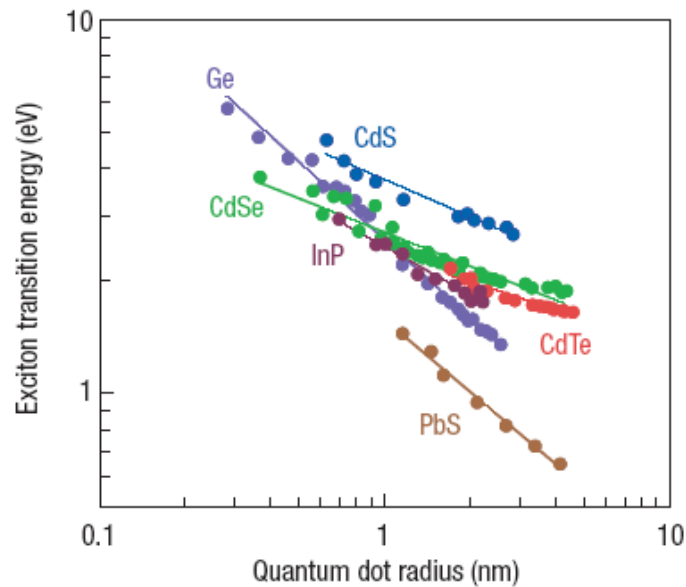


Figure 2. Size-tunable excitation energy for various QD materials[6]

Exchange interaction in QDs raises the energy of singlet state and lowers the energy of three degenerate triplet states. The exchange interaction increases when the exciton is spatially compressed which provides an opportunity to learn about the excited state and electronic structure of a nanoscale system with spectroscopy [14-16]. For QDs the challenge is that their spectra are obscured by inhomogeneous line broadening. In this case we need special technique to probe the singlet-triplet split state.

The magnitudes of the splitting for QDs are much smaller than in organic materials. The reason for this is that QDs possess high dielectric constant which attenuates the long-range electron repulsion compared with organic materials. For the conjugated oligomers [53-56] the singlet-triplet splitting are closely comparable to those for the aromatic [57] molecules and polyene series [58].

1.2.2 Exciton binding energy in QDs

In a quantum confined system the energy difference between the electronic bandgap and the exciton transition energy can be taken as the exciton binding energy as shown in Figure 3. The binding energy is the difference of exciton transition energy and the electronic bandgap. Without considering structural relaxation of the material or its surroundings the bandgap energy can be written as the difference between the ionization potential and electron affinity[17].

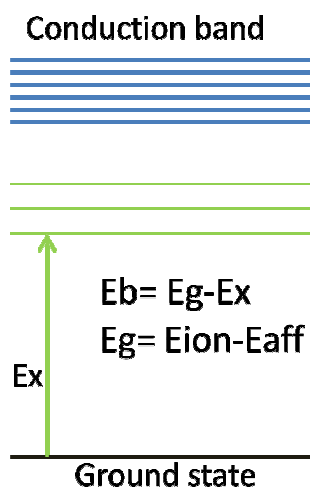


Figure 3. Exciton binding energy

The exciton binding energy is usually small in a bulk semiconductor material with high dielectric constant: 4.9 meV for GaAs, 5.1 meV for InP, 15 meV for CdSe, and 27 meV for CdSe[6]. At room temperature the excitons are easily disturbed and dissociate into free carriers, therefore, these bulk semiconductors are ideal for photovoltaic applications. For the nanoscale materials the exciton binding energies are significant in magnitude and size tunable.

1.2.3 Exciton dynamics in QDs

The dynamics of excitons is always of interest for researchers. Due to the presence of surface states or trap states dynamic processes in QDs are generally more complex than in the bulk. In addition to size dependence of optical properties, strong quantum confinement in semiconductor nanoparticles also affects their exciton relaxation, annihilation and dissociation dynamics. We can find characteristic features in particular materials, e.g. photosynthetic complex, QDs, conjugated polymers and thin nanotubes. One of the most studied natural systems photosynthetic proteins presents us with an excellent example to measure and investigate electronic energy transfer. The energy transfer or migration in conjugated polymer has been studied, since it is a key process in working mechanism for many opto-electric devices based on conjugated materials[18]. For QDs the relaxation process including radiative and non-radiative processes is always a continued interest.

Electronic dephasing occurs on a time scale of a few to a few tens of fs[19]. The electron and hole undergo intraband relaxation to the bottom of the CB and the top of VB, respectively[20]. This relaxation is ascribed to the electron-phonon interactions and

occurs on the time scale of several tens to hundreds of fs. The relaxed electron and hole may radiatively recombine through the emission of a photon. The electron and hole can recombine nonradiatively. Due to surface defects the electrons or holes trapping into these states becomes important and occurs on a time scale of a few ps to a few tens of ps. The time scale for trapping of charge carriers is usually faster than that for bandedge radiative recombination[7].

QDs can support multiple exciton populations, such as biexcitons, triexcitons and so on. The recombination time of biexciton in CdSe QDs is the order of tens of picoseconds, depending on the size[21, 22].

1.3 Exciton in conjugated polymers

1.3.1 Conjugated polymer

The electroluminescence property of highly conjugated linear macromolecules has been widely studied in the condensed phase due to its state in many solar cell devices. Its properties are characterized by strong intramolecular and weak intermolecular interactions. Two basic types of exciton have been identified: intrachain and interchain. Intrachain excitons are delocalized on the extended π -conjugation along the sections of the polymer backbone. Interchain excitons are formed by chains segments coupling due to so close to each other in space. The chain segments are either from different chains or same chain folded back on itself. Consequently, some researchers take polymer electronical behavior as quasi-one-dimensional system. The optical properties of polymer are the combined effect of electron-electron interaction, electron-nuclear coupling and structure disorder. Since the length of the polymer is in the nanoscale, the electron-

electron interaction and electron-nuclear coupling will be enhanced, which makes the spectroscopy of conjugated polymer a challenge, but fascinating.

The electronic levels of conjugated polymers have been established as the “conventional” band gap semiconductors. Electronic excitation promotes an electron to an empty orbital and leaves a hole behind in the HOMO orbital, the linear combination of all pairs of electron-hole excitations is a bound state, as shown in Figure 3, the excitation energy lies below the conduction band threshold. Excitons are the primary photoexcited states of conjugated polymers [2].

1.3.2 The size dependence of excitons and their spectra

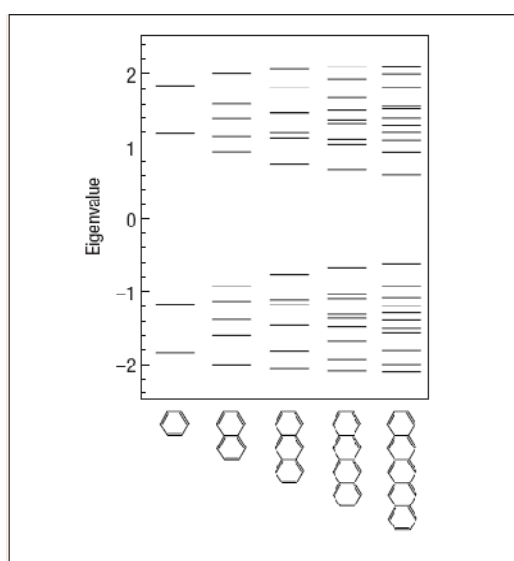


Figure 4. Molecular orbital picture for confined systems[6]

Figure 4 shows the ground states and excited states for a series of polyacenes. As shown in the picture the band gap decreases and the density of states increases with the increase of the conjugation size. The band gap and state density change originate from

the electron-electron interaction change which is related to the molecular orbital wavefunction delocalization. Single-excitation configuration is delocalized over the extent of the molecules, which is consistent with the exciton in an extended system in which the excitation configuration is mixed by exchange interactions.

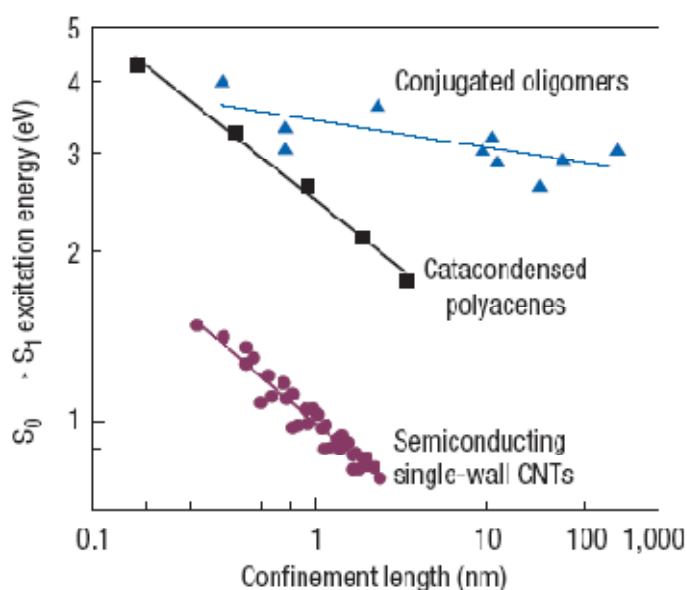


Figure 5. The size dependence of exciton energy versus confinement length of a range of organic materials[6, 12, 16, 23-25]

1.3.3 Localization and delocalization of exciton dynamics in conjugated polymers

Exciton localization or delocalization is related to the molecular structure. In reality, polymers are rarely free from some kind of disorder. The conformation disorders of conjugated polymer in solution are necessarily from a consequence of thermal fluctuations. Polymers usually display glassy and disordered conformations in the condensed phase as consequence of being quenched from solution. Generally disorder and large separation distance of interchain in solid state will minimize the

interchromophore coupling and produce localized excitons. Torsion, kinks and chemical defects serve to create a random distribution of chain lengths and localization of the exciton. The dielectric environments around the exciton will change from position to position which leads to a distribution of energy levels.

In Hu's paper[26] they use a single molecule approach to study the conformational properties of poly[2-methoxy-5-(2'-ethylhexyl)oxy-1,4-phenylene-vinylene] (MEH-PPV) and demonstrate that the optical, electronic and mechanical properties of materials containing polymer chains depend sensitively on the conformation adopted by the chain. The absorption and fluorescence studies of π -conjugated polymers or oligomers[27] show that the optical properties highly depends on the polymer chain conformation[28, 29]. The reason is the disorder resulting from π -conjugation disruption along the backbone.



Figure 6. Typical conformations of a 100-segment homopolymer generated by Monte Carlo simulations[26]

In one dimensional system the exciton couples to the nuclei and undergoes vibrational relaxation with a barrierless process to the formation of self-localization exciton polarons. The interaction between excitons and nuclear motions (phonon) also can produce exciton

self-trapping, which results in a lattice distortion around it. The sources of nuclear vibration are contributed by intramolecular vibrations and the environment. Exciton self-trapping occurs through a local collective structural change, resulting in a polaron-exciton. Exciton self-trapping leads to the exciton localization. The size and electronic make-up of an organic exciton can change markedly on short timescales after photoexcitation. That can be explained by the tendency of molecules to change their equilibrium geometry in the excited state compared with the ground state. The precise excited state dynamics is dictated by competition between the delocalizing effect of electronic coupling and the localizing influence of electron-phonon coupling.

1.3.3 Exciton binding energy

In molecular materials, the electron-hole coupling is on the order of a few electronvolts. For a conjugated polymer the size dependence of the binding energy, and extent of exciton localization complicates matters. Exciton self-trapping in conjugated polymers leads to a strongly bound exciton (hundreds meV).

The binding energy is influenced by the disorder of the material, or the strong coupling between electronic and nuclear degrees of freedom. In addition, low frequency vibrations couple to the exciton. The relationship between the binding energy and precise nature of the excited state are still needed for discussion. Electron-lattice coupling in conjugated compounds is demonstrated by the appearance of vibronic progressions in the optical absorption spectra.

1.3.3 Exciton diffusion

The motivation to achieve high energy conversion efficiency stimulates researchers to understand the exciton migration in conjugated polymer systems experimentally and theoretically. In photovoltaic devices[30, 31], large exciton diffusion lengths are necessary so that the exciton can migrate to the regions before charge separation can occur. Singlet exciton diffusion is a Coulomb-induced, Förster-like process of exciton transfer between donors and acceptors[32]. The point-dipole approximation in Förster energy transfer model was used to explain the exciton diffusion in earlier times. It reproduces some experimental features, such as time dependence of spectral diffusion, but is inappropriate to quantitatively analyze energy transfer observed in conjugated polymers.

$$D = \eta \left(\frac{4\pi C}{3} \right)^{\frac{4}{3}} \frac{R_0^6}{\tau_{fl}} \quad (2)$$

$$L_D = \sqrt{6D\tau_{fl}} = \sqrt{6\eta \left(\frac{4\pi C}{3} \right)^{\frac{2}{3}} R_0^3} = 6.36\sqrt{\eta C^{2/3} R_0^3} \quad (3)$$

D is exciton diffusion constant, C is the chromophore number density, τ_{fl} is the fluorescence lifetime of donor in the absence of electronic energy transfer, R_0 is the Förster radius. η is a correction factor ranging from 0.32 to 0.56, which depends on the theoretical method used for its estimation. L_D is the diffusion length.

Recent approximation models [33-35] employ the concept of a chromophore to build a link between random polymer conformations and the energetic and spatial distributions of the donor and acceptors. The approximation is based on the general finding that conjugated polymer is highly disordered in solid state, and twists of chain π -conjugation into basic chromophores, also called conformational subunits. In the model a chromophore is defined via a minimum threshold in the π -orbital overlaps, and an energy distribution is obtained by assuming the excitons delocalize on the defined chromophore.

The twists and kinks of the polymer backbone lead to inhomogeneous chromophore distribution. To employ this model we need to apply Condon approximation. Generally the time interval for exciton hopping is much longer than vibrational relaxation times. In addition, the time taken for exciton transfer is much faster than the above processes. These time scales justify the assumption that donor chromophores and acceptor chromophores are in their excited state and ground state relaxed geometries, respectively. The chain conformation and disorder influence the electronic energy transfer and the time scale of the evolution of electronic excited states.

1.4 The approaches used to study the exciton dynamics:

The exciton dynamics study on semiconductor QDs and conjugated polymers allows a deeper understanding of their fundamental properties by providing complementary information to that from static measurements. This can in turn guide the design, synthesis, and implementation of nanomaterials for photocatalysis, photoelectrochemistry and photovoltaics.

The electron transfer, and subsequent charge-carrier relaxation and recombination occur from hundred femtosecond to hundred picosecond or nanosecond in nanoscale QDs and conjugated polymers. To study the formation of instantaneous species and gain the dynamic properties of charge carrier, the ultra-fast pump-probe technique is one of the most powerful approaches due to its short pulse duration and high peak power that have been decisive in behavior analysis[36]. Over the last two decades the advancements in ultrafast laser technology and different monitoring based on transient absorption or time-

resolved fluorescence has made it relatively easy to study exciton dynamics[37-40]. One of most commonly used time-resolved laser techniques is transient absorption (TA).

1.4.1. Pump-probe technique:

In the pump-probe experimental setup, the pump pulse with femtosecond duration disturbs the sample first, and after a temporal delay, the second pulse with a less powerful short pulse works as probe light which overlaps with pump beam at the sample. The change in the probe light will be analyzed and detected by a monochromator and a detector. The pump beam is delayed with respect to the probe beam using a computer-controlled delay stage. There are two ways to monitor the dynamics change: transient absorption spectrum at fixed time, and transient absorption dynamics at fixed wavelength. The intensity change in absorption of probe pulse reflects change of charge carriers or exciton population in excited state [41, 42], and the temporal evolution of absorption will yield the dynamics of the transformations (chemical reaction rate). The transient absorption spectrum and transient dynamics will provide the information on the species, the population dynamics and the evolution of various species from ground, excited, reduced and oxidized forms.

Usually the assignment of the observed signal is complex; the determination of the origin of the TA signal is often accompanied by careful control experiments and other information, e.g., theoretical modeling and simulations.

1.4.2. Laser-electron accelerator facility (LEAF)

Pulse radiolysis is one of most powerful approaches of investigating the transient species such as ions, radicals, and excited states in solution and solid by employing short

pulses of electrons. The high energy electron pulse which is generated by a linear accelerator (linac), a Febetron, or a Van de Graaff accelerator initiates a sequence of reaction. The primary processes following high energy radiation absorption is quite different from those of light absorption. For the pulse radiolysis method, the role of solvent is pivotal in determining the subsequent type of species which arises. The pulse radiolysis measurements provide the information on the excited state.

1.4.3. Another technique that is often utilized is time-resolved photoluminescence (PL) measurements. The excitation mechanism is similar to that of TA, only the monitoring of the excited population is different. In TA measurement, a probe pulse is used to monitor the excited state population, while in PL, the population is monitored directly with a photo-detector, e.g., a photomultiplier tube (PMT), photodiode, or charge-coupled device (CCD) [43-45].

An even better technique to achieve fluorescence time resolution is the use of optical Kerr shutter. The optical Kerr shutter relies on the transient birefringence induced in non-linear material upon intense energy laser pulse to produce an ultrafast shutter. The recovery time of the non-linear medium determines the time resolution.

Other methodologies exist, involving luminescence upconversion[46], time-resolved photoelectron spectroscopy, time resolved fluorescence[47], four-wave mixing[48], and terahertz time-domain spectroscopy[49].

References

1. Gregg, B.A., *Excitonic solar cells*. The Journal of Physical Chemistry B, 2003. **107**(20): p. 4688-4698.
2. Friend, R., et al., *Electroluminescence in conjugated polymers*. Nature, 1999. **397**(6715): p. 121-128.
3. Sundström, V., T. Pullerits, and R. van Grondelle, *Photosynthetic light-harvesting: reconciling dynamics and structure of purple bacterial LH2 reveals function of photosynthetic unit*. The Journal of Physical Chemistry B, 1999. **103**(13): p. 2327-2346.
4. Nozik, A., *Quantum dot solar cells*. Physica E: Low-dimensional Systems and Nanostructures, 2002. **14**(1): p. 115-120.
5. Günes, S., H. Neugebauer, and N.S. Sariciftci, *Conjugated polymer-based organic solar cells*. Chemical Reviews, 2007. **107**(4): p. 1324-1338.
6. Scholes, G.D. and G. Rumbles, *Excitons in nanoscale systems*. Nature materials, 2006. **5**(9): p. 683-696.
7. Wheeler, D.A. and J.Z. Zhang, *Exciton dynamics in semiconductor nanocrystals*. Advanced Materials, 2013. **25**(21): p. 2878-2896.
8. Efros, A.L., *Interband absorption of light in a semiconductor sphere*. Soviet Physics Semiconductors-Ussr, 1982. **16**(7): p. 772-775.
9. Ekimov, A., et al., *Absorption and intensity-dependent photoluminescence measurements on CdSe quantum dots: assignment of the first electronic transitions*. JOSA B, 1993. **10**(1): p. 100-107.
10. Gaponenko, S.V., *Optical properties of semiconductor nanocrystals*. Vol. 23. 1998: Cambridge university press.
11. Kleven, H. and J. Platt, *Spectral Resemblances of Cata - Condensed Hydrocarbons*. The Journal of Chemical Physics, 1949. **17**(5): p. 470-481.
12. Hines, M.A. and G.D. Scholes, *Colloidal PbS nanocrystals with size - tunable near - infrared emission: observation of post - synthesis self - narrowing of the particle size distribution*. Advanced Materials, 2003. **15**(21): p. 1844-1849.

13. Pariser, R. and R.G. Parr, *A semi - empirical theory of the electronic spectra and electronic structure of complex unsaturated molecules. II.* The Journal of Chemical Physics, 1953. **21**(5): p. 767-776.
14. Leung, K., S. Pokrant, and K.B. Whaley, *Exciton fine structure in CdSe nanoclusters.* Physical Review B, 1998. **57**(19): p. 12291.
15. Efros, A.L., et al., *Band-edge exciton in quantum dots of semiconductors with a degenerate valence band: Dark and bright exciton states.* Physical Review B, 1996. **54**(7): p. 4843.
16. Micic, O., et al., *Size-dependent spectroscopy of InP quantum dots.* The Journal of Physical Chemistry B, 1997. **101**(25): p. 4904-4912.
17. Yaron, D., et al., *Comparison of density matrix renormalization group calculations with electron-hole models of exciton binding in conjugated polymers.* The Journal of Chemical Physics, 1998. **108**(17): p. 7451-7458.
18. Beljonne, D., et al., *Interchain vs. intrachain energy transfer in acceptor-capped conjugated polymers.* Proceedings of the National Academy of Sciences, 2002. **99**(17): p. 10982-10987.
19. Masia, F., et al., *Exciton dephasing in lead sulfide quantum dots by X-point phonons.* Physical Review B, 2011. **83**(20): p. 201309.
20. Kambhampati, P., *Unraveling the structure and dynamics of excitons in semiconductor quantum dots.* Accounts of chemical research, 2010. **44**(1): p. 1-13.
21. Klimov, V., et al., *Optical gain and stimulated emission in nanocrystal quantum dots.* Science, 2000. **290**(5490): p. 314-317.
22. Klimov, V.I., et al., *Quantization of multiparticle Auger rates in semiconductor quantum dots.* Science, 2000. **287**(5455): p. 1011-1013.
23. Yu, W.W., et al., *Experimental determination of the extinction coefficient of CdTe, CdSe, and CdS nanocrystals.* Chemistry of Materials, 2003. **15**(14): p. 2854-2860.
24. Neshet, G., L. Kronik, and J.R. Chelikowsky, *Ab initio absorption spectra of Ge nanocrystals.* Physical Review B, 2005. **71**(3): p. 035344.
25. Fu, H. and A. Zunger, *InP quantum dots: Electronic structure, surface effects, and the redshifted emission.* Physical Review B, 1997. **56**(3): p. 1496.

26. Hu, D., et al., *Collapse of stiff conjugated polymers with chemical defects into ordered, cylindrical conformations*. Nature, 2000. **405**(6790): p. 1030-1033.
27. Bässler, H. and B. Schweitzer, *Site-selective fluorescence spectroscopy of conjugated polymers and oligomers*. Accounts of chemical research, 1999. **32**(2): p. 173-182.
28. Barbara, P.F., et al., *Single-molecule spectroscopy of conjugated polymers*. Accounts of chemical research, 2005. **38**(7): p. 602-610.
29. Schindler, F., et al., *Counting chromophores in conjugated polymers*. Angewandte Chemie, 2005. **117**(10): p. 1544-1549.
30. Peumans, P., S. Uchida, and S.R. Forrest, *Efficient bulk heterojunction photovoltaic cells using small-molecular-weight organic thin films*. Nature, 2003. **425**(6954): p. 158-162.
31. Menke, S.M., W.A. Luhman, and R.J. Holmes, *Tailored exciton diffusion in organic photovoltaic cells for enhanced power conversion efficiency*. Nature materials, 2013. **12**(2): p. 152-157.
32. Hwang, I. and G.D. Scholes, *Electronic Energy Transfer and Quantum-Coherence in π -Conjugated Polymers†*. Chemistry of Materials, 2010. **23**(3): p. 610-620.
33. Krueger, B.P., G.D. Scholes, and G.R. Fleming, *Calculation of couplings and energy-transfer pathways between the pigments of LH2 by the ab initio transition density cube method*. The Journal of Physical Chemistry B, 1998. **102**(27): p. 5378-5386.
34. Singh, J., et al., *Fluorescence depolarization in poly [2-methoxy-5-((2-ethylhexyl)oxy)-1, 4-phenylenevinylene]: Sites versus eigenstates hopping*. The Journal of Chemical Physics, 2009. **131**(19): p. 194905.
35. Beljonne, D., et al., *Beyond Forster resonance energy transfer in biological and nanoscale systems*. The Journal of Physical Chemistry B, 2009. **113**(19): p. 6583-6599.
36. Rulliere, C., *Femtosecond laser pulses*. Vol. 2. 1998: Springer.
37. Zhang, J.Z., *Ultrafast studies of electron dynamics in semiconductor and metal colloidal nanoparticles: Effects of size and surface*. Accounts of chemical research, 1997. **30**(10): p. 423-429.

38. Zhang, J.Z., *Interfacial charge carrier dynamics of colloidal semiconductor nanoparticles*. The Journal of Physical Chemistry B, 2000. **104**(31): p. 7239-7253.
39. Klimov, V.I. and D.W. McBranch, *Femtosecond high-sensitivity, chirp-free transient absorption spectroscopy using kilohertz lasers*. Optics letters, 1998. **23**(4): p. 277-279.
40. Kaiser, W. and D.H. Auston, *Ultrashort laser pulses: generation and applications*. 1993: Springer.
41. Zhang, J.Z., *Interfacial charge carrier dynamics of colloidal semiconductor nanoparticles*. Journal of Physical Chemistry B, 2000. **104**(31): p. 7239-7253.
42. Zhang, J.Z., R.H. Oneil, and T.W. Roberti, *Femtosecond Studies of Photoinduced Electron Dynamics at the Liquid-Solid Interface of Aqueous Cds Colloids*. Journal of Physical Chemistry, 1994. **98**(14): p. 3859-3864.
43. Ceroni, P., *The exploration of supramolecular systems and nanostructures by photochemical techniques*. Vol. 78. 2011: Springer Science & Business Media.
44. Galland, C., et al., *Two types of luminescence blinking revealed by spectroelectrochemistry of single quantum dots*. Nature, 2011. **479**(7372): p. 203-207.
45. Kuposov, A.Y., et al., *Electronic Properties and Structure of Assemblies of CdSe Nanocrystal Quantum Dots and Ru - Polypyridine Complexes Probed by Steady State and Time - Resolved Photoluminescence*. Advanced Functional Materials, 2011. **21**(16): p. 3159-3168.
46. Wu, W., et al., *Upconversion luminescent characteristics and peak shift of CdSeS nanocrystals under different wavelength laser excitation*. Journal of Nanoparticle Research, 2011. **13**(3): p. 1049-1061.
47. Bujak, Ł., et al., *Fluorescence spectroscopy of semiconductor CdTe nanocrystals: preparation effect on photostability*. Open Physics, 2011. **9**(2): p. 287-292.
48. Meuer, C., et al., *40 Gb/s wavelength conversion via four-wave mixing in a quantum-dot semiconductor optical amplifier*. Optics Express, 2011. **19**(4): p. 3788-3798.
49. McIntosh, A.I., et al., *Terahertz spectroscopy: a powerful new tool for the chemical sciences?* Chemical Society Reviews, 2012. **41**(6): p. 2072-2082.

Chapter 2. Techniques and Instrumentation

This chapter contains the experimental details about the experiments carried out in this work. Section 2.1 describes the preparation procedures of the Ti/O polyoxometalate clusters: Ti17cat4, Ti17, and Ti6; and the procedure for P3HT film preparation on different substrates. Section 2.2 describes the typical methods used to characterize the exciton in clusters and P3HT films: UV-Vis, Fluorescence, Raman Spectroscopies, Scanning Emission Microscope, pump-probe, pulse radiolysis and chemical quantum calculations.

2.1 Materials and Procedures

2.1.1 Ti/O clusters preparations

The detail preparations of Ti17cat4, Ti17 and Ti6 clusters and X-ray structure characterization are described in the literature[1].

Ti₁₇(μ₄-O)₄(μ₃-O)₁₆(μ₂-O)₄(OPrⁱ)₂₀ [Ti17]: In air, Ti(OPri)₄ (8.4 mL, 29 mmol) was added via syringe to acetic acid (2.1 mL, 37 mmol) in a Teflon-lined Parr bomb with a 23mL capacity. The bomb was sealed, placed in a 150 °C oven for 5 days, and then cooled to room temperature, after which the bomb was opened and the solution was quickly transferred with pipet to a Schlenk flask. Colorless crystals of Ti17 precipitated immediately. The atmosphere was replaced with Ar in several pump-purge cycles.

Ti₁₇(μ₄-O)₄(μ₃-O)₁₆(μ₂-O)₄(OPrⁱ)₁₆(Catechol)₄ [Ti17cat4]: In a small glass vial, Ti17 (18.4 mg, 7.73 μmol) was dissolved in a 3 mL of toluene. To this was added dropwise a

solution of pyrocatechol (3.4 mg, 30.8 μmol) in 3 mL of toluene. Slow evaporation of the dark-red solution yield red crystals of Ti_6cat_4 .

$\text{Ti}_6(\mu_3\text{-O})_6(\text{CH}_3\text{COO})_6(\text{CH}_3\text{HCOCH}_3)_3$ [Ti6]: A solution of acetic acid in toluene (1:4) was added to titanium isopropoxide in toluene (1:20; overall $\text{CH}_3\text{COOH}:\text{TiP}:\text{toluene}$, 2:1:27). After refluxing for 15 h, the solvent was removed under vacuum and $[\text{Ti}_6\text{O}_6](\text{CH}_3\text{COO})_6(\text{OiPr})_6$ was subsequently obtained via recrystallization from CH_2Cl_2 at 0°C . All synthetic steps were performed under nitrogen using Schlenk-line techniques [2].

2.1.2 P3HT film preparation on Klarite

Regioregular P3HT (poly (3-hexylthiophene-2, 5-diyl)) was purchased from Aldrich company ($M_n=30,000\text{--}60,000$, $\text{PDI}=2.4$), anhydrous chlorobenzene was also from Aldrich. Weighed 3 mg P3HT into a vial and measured 1.5 ml chlorobenzene to the P3HT. Sealed the vial and put it in $50\text{--}60^\circ\text{C}$ water bath, until it formed the clear red orange solution. For the thin film fabrication the 2 mg/ml P3HT solution was spin coating on the Klarite substrate (Renishaw Diagnostics) at 3500 RPM (SCS G3P-8 Spincoat Specialty Coating System) for 2.5 minutes, the prepared sample was annealed at 60°C under vacuum for 1 hour and cooled down naturally, the sample is ready to use after keeping in inter gases over night.

Klarite is a commercial gold coated (thickness of gold coating is $\sim 100\text{ nm}$) silicon substrate. It consists of the pattern area and “smooth” area, the pattern area has a regular array of submicrometer pyramids holes ($1.5\times 1.5\text{ }\mu\text{m}$, $1\text{ }\mu\text{m}$ in depth) separated by 400 nm (as shown the SEM picture). The highlight of the substrate is the “bumpy” surface made

of ~50 nm gold nanoparticles with randomly spread gold nanoparticles on it. The same preparation conditions and procedure for P3HT film on glass substrate and the P3HT film with gold nanocore on silvered slide[2].

2.2 Techniques and instrumentation

2.2.1 UV-Vis absorptions

Ground state absorption was taken at a Varian Cary 500 spectrometer. A quartz cuvette containing pure solvent was used as sample blanks as needed.

2.2.2 Fluorescence spectroscopy

Fluorescence was collected on a Varian Cary Eclipse fluorometer; and the low temperature fluorescence was recorded by using a cryostat as an attachment to the fluorometer. The excitation wavelength was typically chosen based on the absorption measurement. For Ti17 cluster 300 nm excitation was used and 350 nm as emission wavelength for Ti6, the resolution is 2.5 nm.

2.2.3 Raman Microspectroscopy

Raman spectra were recorded using a Kaiser Optical Systems Confocal Raman Microprobe equipped with a 785 nm diode laser. A 100x oil immersion objective was used to focus approximately 6-10 mW of the single mode power within the sample volume of $\sim 2 \mu\text{m}^3$. The spectral coverage ranged from 100 to 3450 cm^{-1} , and the resolution was 4 cm^{-1} . The spectra were acquired using 4 accumulations of 60 s exposure time each.

Raman sample preparation: Approximately 1 mg of the Ti17 or Ti17cat4 or Ti6 cluster was spread in an indentation in a clean brass cell and covered by a glass slide with oil sealing the edges which prevent air from entering the sample.

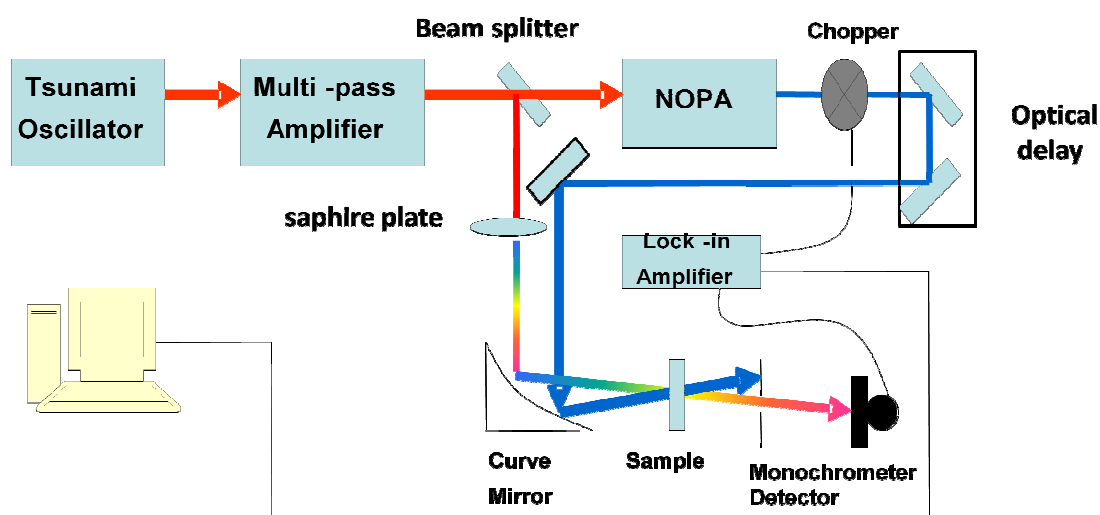
2.2.4 Scanning electron microscope (SEM)

The surface morphology and thickness of P3HT film on Klarite was measured with model S-4800 field emission scanning electron microscope (S-4800 FE SEM) from Hitachi high-technologies Corporation.

2.2.5 Pump-probe technique

Transient Absorption Spectroscopy in the Visible and IR was measured with ultra-fast pump-probe approach. The Ti:Sapphire oscillator is pumped by 530 nm, 4.5 W CW Nd:VO₄ diode laser, and produces 70 fs pulses at 795 nm with 80 MHz. The laser pulse is stretched to 100 ps after going through the stretcher, the stretched pulse is lead to a home-built multipass Ti:Sapphire amplifier which is pumped by 1.25 KHz 527 nm (Photonics Industries International). The 560 mW output of the amplified pulse was split to generate independently tunable pump and probe pulses. The pump beam (~25 fs, 3.5 mW, 300 nm) was produced by frequency doubling the output of a noncollinear optical parametric amplifier (NOPA, Topas White, Light Conversion). The pump was modulated at 17 Hz with the help of a mechanical chopper. The probe white light continuum is produced by focusing part of amplified laser pulse into a 2 mm sapphire plate to generate. The probe beam was delayed with respect to the pump using a computer-controlled delay stage, the white light and pump light was focused to a 10 mm fused silica cuvette

containing the sample by a 45° parabolic mirror with 10 cm focus length. The probe light containing absorption information was dispersed with a monochromator (Oriel MS257 with a 1200 lines/mm grating) and detected with a Si photodiode (Thorlabs, DET110). The signals from detector were sent into the lock-in amplifier (Stanford Research, SR 810), the transient absorption dynamics was recorded with the monochromator fixed at desired wavelength and scanning the time, the transient absorption spectrum was recorded by scanning the wavelength range at fixed pump–probe delay time. The relative polarization of the pump and probe beams was set at the “magic angle”. All the data were analyzed with OriginPro 8.6 software.



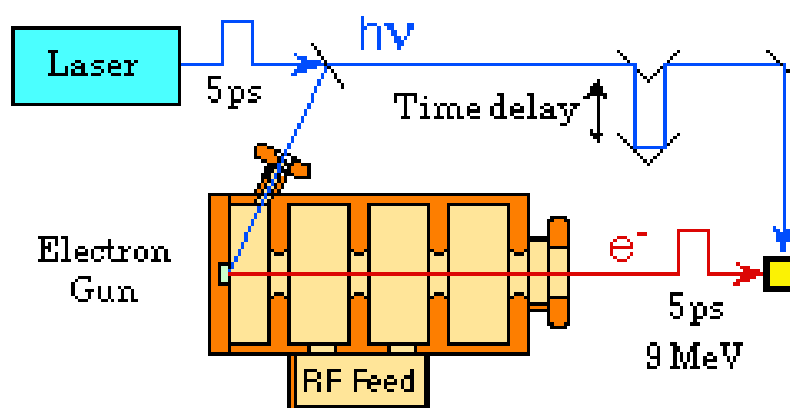
Scheme 1. Transient absorption measurement setup

The IR transients were obtained using as a probe sub-100 fs pulses produced by a home-built IR OPA based on parametric down-conversion in KNbO_3 and pumped by the same multipass Ti:sapphire amplifier as above. In order to optimize the relative duty cycles, the output of the IR detector (InAs photodiode) was sampled with a boxcar

integrator (Stanford Research 280) the analog output of which served as the input for the lock-in amplifier. Instead of using IR interference filters, we took advantage of the narrow transparency window of acetonitrile at $2.65\ \mu\text{m}$ to select the desired wavelength. The

Ti17 sample was prepared in the same fashion as described above. The anatase film on a thin silica substrate was prepared as described in the literature. It was placed in a cuvette containing acetonitrile in order to ensure comparable experimental conditions.

2.2.6 Pulse radiolysis



Scheme 2. The layout of the LEAF at Brookhaven national lab[4]

Pulse radiolysis is using electron pulses to study short-lived free radicals or excited state. The electron pulses are produce from Laser-Electron Accelerator Facility (LEAF) as shown in scheme 2. Part of the laser light is leading into a resonant cavity impinging on a photocathode, the cavity is radio frequency (RF) gun about 30 cm long. The emitted

electrons are accelerated to 9.2 MeV within the length of the gun by ~ 15 megawatt pulse of RF power from a SLAC-type 2.856 GHz klystron. The laser pulse is synchronized with the RF power to produce the electron pulse near the peak field gradient (about 1 MeV/cm). Thus the pulse length and intensity are a function of the laser pulse properties, and electron pulse lengths as short as 5 picoseconds are attainable.

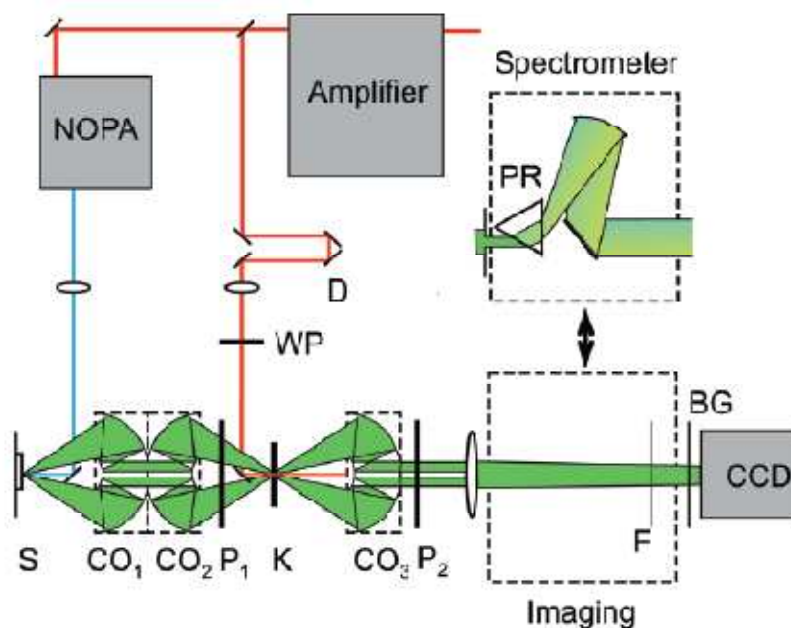
The spectra of $\text{Ti17}^{\bullet-}$ were obtained at the Laser-Electron Accelerator Facility (LEAF) at the Brookhaven National Laboratory. LEAF and the methods used are described elsewhere[4]. Briefly, an electron pulse (≤ 120 ps duration) was focused into a quartz cell with an optical path length of 20 mm containing the solution of interest. The monitoring light source was a 65 W xenon arc lamp pulsed to a few hundred times its normal intensity. Wavelengths were selected using 10 nm bandpass interference filters. Transient absorption signals were detected with either an FND-100Q silicon diode ($\lambda \leq 1000$ nm, 2 ns, EG&G) or a GAP-500L InGaAs diode ($\lambda \geq 1100$ nm, 8 ns, Germanium Power Devices) and digitized with a Tektronix TDS-680B or a LeCroy 8420A oscilloscope. The electron pulses ionized the solvent, benzonitrile, to produce its anions and cations. Electrons from the solvent anions (“excess electrons”) were transferred to Ti17, reducing it and producing $\text{Ti17}^{\bullet-}$, i.e., the radical anion of the cluster. Benzonitrile cations cannot oxidize Ti17, and as a result, the corresponding $\text{Ti17}^{\bullet+}$ species was not observed. This was confirmed by experiments on Ti17 solutions saturated with SF_6 , which selectively scavenges the excess electrons. Under these conditions, neither $\text{Ti17}^{\bullet+}$ nor $\text{Ti17}^{\bullet-}$ were observed.

2.2.7 Femtosecond Ker-gated fluorescence microscopy

The laser system consisted of a commercial Ti:Sapphire oscillator (KMLabs Griffin oscillator) which was pumped at 532 nm with 3.0 W, a repetition rate of 80 MHz seed pulse was lead to a stretcher and a commercial regenerative amplifier (the Wyvern 500 amplifier, KMLab). The main component of the regenerative amplifier is a Ti:sapphire crystal in cryogenic system with ion pump, and being pumped by 532 nm pump laser with ~100 ns duration. The seed pulse energy builds up through multiple back and forth travel in the cavity, after a sufficient number of passes the amplifier provides 50 fs, 9 μ J and a repetition rate of 100 KHz pulse at 790 nm. The amplified light is split outside the amplifier, partial of the beam serves as the gating beam, the other split beam goes through a home built NOPA. One part of the output is lead to pump a noncollinear optical parameter amplifier (NOPA) to produce the desired excitation light at 490 nm and the remaining part is utilized to drive the Kerr gate.

As shown in the scheme 3[5], the excitation pulse in blue color (tunable from 250 to 1100 nm) from NOPA is directed into the sample (S) via a small mirror in front of the first Cassegrain (CO). The fluorescence light together with the scattering light is focused into 0.5 mm fused silica the Kerr medium via a second CO, at the same time the gate beam in red color through a delay stage was focused onto the Kerr medium. Only when the emission light overlaps with the gate beam at the Kerr material spatially and temporally the fluorescence can pass through the Kerr shutter. The transmitted light turn into parallel light after the third CO and is detected by a research-grade CCD camera (Ac). By delaying the gating pulse with respect to the excitation pulse, the time evolution of the imaged object, $I(x, y; t)$, can be followed and the corresponding emission decays can be assembled. In addition to the imaging mode of operation, the Kerr-gated

microscope can be arranged in a spectrally dispersed configuration and function as a femtosecond fluorescence spectrometer. After passing a polarizer (P1) and subsequently recollimated via a third CO.



Scheme 3. Setup for the Kerr-gated fluorescence microscopy[5]. S, sample; CO₁₋₃:Cassegrain objectives; P1-2, polarizer; P1-2: Polarizers; K: Kerr material; D: Delay line; F, BG: Beam filter; CCD, charge-coupled device; WP: Waveplace; PR: Prism

2.6 Computation

The calculation of the Raman and IR absorption spectra of the isopropoxide anion and the oxo isopropoxyl radical was carried out at the DFT B3LYP level with the 6-31G* basis set using the Spartan'10 software package by Wave function, Inc. The resulting vibrational frequencies were not scaled.

The hole hopping calculation on Ti17cat4 cluster: The quantum dynamics simulations were based on a tight-binding extended-Hückel Hamiltonian. An initial electronic wave packet representing a hole formed by photo-oxidation of a catecholate adsorbate was evolved in time by integrating the time-dependent Schrodinger equation. To facilitate the integration, the wave packet was expanded in terms of the molecular orbitals of Ti17cat4. The configuration of the cluster was obtained by refining the X-ray crystal structure[1] by geometry optimization at the density functional theory (DFT) B3LYP/LANL2DZ level. The DFT calculations were performed with the Jaguar software package⁵. In order to reduce the number of atoms in the computational model of the cluster, the isopropoxy ligands were replaced by hydroxyls. Four additional protons were adsorbed to the surface O^{2-} ions to neutralize the cluster. The resulting refined structure is in quantitative agreement with the X-ray model, indicating that structural changes due to temperature or salvation can be neglected due to the rigidity of the system. Simulations of the hole propagation dynamics were performed in a frozen geometry of the cluster in vacuum and did not include nuclear reorganization.

References

1. Benedict, J. B.; Coppens, P., The Crystalline Nanocluster Phase as a Medium for Structural and Spectroscopic Studies of Light Absorption of Photosensitizer Dyes on Semiconductor Surfaces. *J Am Chem Soc* **2010**, *132* (9), 2938-2944.
2. Karatchevtseva, I., D. J. Cassidy, et al. (2008). "Crystallization of TiO₂ powders and thin films prepared from modified titanium alkoxide precursors." *Journal of the American Ceramic Society* **91**(6): 2015-2023.
3. Yu, B.; Goodman, S.; Abdelaziz, A.; O'Carroll, D. M., Light-management in ultra-thin polythiophene films using plasmonic monopole nanoantennas. *Appl Phys Lett* **2012**, *101* (15), 151106.
4. Wishart, J. F.; Cook, A. R.; Miller, J. R., The LEAF picosecond pulse radiolysis facility at Brookhaven National Laboratory. *Review of scientific instruments* **2004**, *75* (11), 4359-4366.
5. Gundlach, L.; Piotrowiak, P., Ultrafast spatially resolved carrier dynamics in single CdSSe nanobelts. *The Journal of Physical Chemistry C* **2009**, *113* (28), 12162-12166.

Chapter 3. Exciton and Excess Electrons in Nanometer Size Molecular Polyoxotitanate Cluster Ti17

3.1 Introduction

Polyoxotitanate cluster Ti17 (proper name $(\text{Ti}_{17}(\mu_4\text{-O})_4(\mu_3\text{-O})_{16}(\mu_2\text{-O})_4(\text{OPr}^i)_{20})$, MW=237.46) contains a 1.2 nm TiO core which offers a unique opportunity to investigate quantum size effects in truly homogeneous, monodisperse nanometer size systems. A view illustrated in Figure 3-1a shows the homogeneous core-shell structures, especially the details of the core-ligand interface and the presence of nonequivalent metal sites will have an influence on the exciton dynamics and charge carrier localization[1-4]. Polyoxometalates, most notably the anionic tungstates, molybdates, and vanadates, display promising photocatalytic properties[5], yet very little is known about the early excited state dynamics in this class of materials[6]. The X-ray structures of several molecular polyoxotitanate clusters were recently determined by Benedict and Coppens[7, 8] enabling studies on structure-dynamics correlations at a level that was impossible because of the inherent polydispersity and surface heterogeneity of TiO_2 nanoparticles. Well characterized polyoxotitanate clusters such as Ti17 can serve as very attractive, experimentally and theoretically tractable models for colloidal TiO_2 , the most widely studied wide band gap semiconductor substrate for hybrid photovoltaic materials[9] and a potent photocatalyst for hydrogen production[10] and pollutant remediation[11].

To study and understand the exciton dynamics, charge localization, and electron-hole coupling in the Ti17 cluster we use comprehensive methods including laser pump-probe and pulse radiolysis experiments. Optical excitation of Ti17 generates Ti17^* excitons,

i.e., electron-hole pairs in which the charges interact with one another, while pulse radiolysis places a single excess electron in the lowest empty orbital (LUMO) or the conduction band (CB) of the cluster, leading to the formation of the corresponding radical anion, $\text{Ti17}^{\cdot-}$. In the case of a single excess charge, the confinement affects only the quantized kinetic energy of electron, while for the exciton the kinetic, Coulomb, and exchange energy are all affected by the size of the nanoparticle[2-4]. The combination of pulse radiolysis and optical spectroscopy gives a more complete view of the electronic states of Ti17 and allows a better grasp of the electron-hole interaction in the confined volume of the cluster.

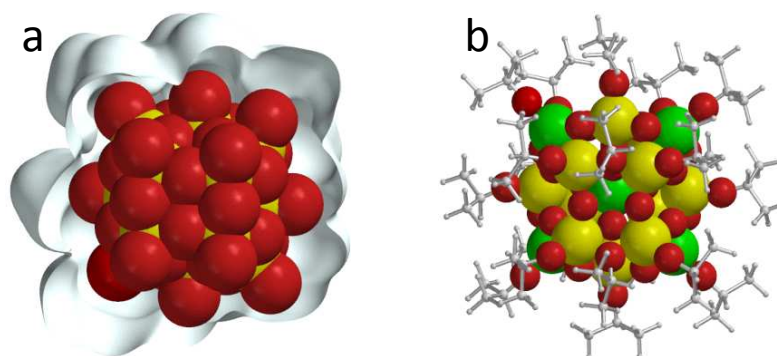


Figure 3-1. Two representation of the Ti17 cluster: (a) The homogeneous TiO core immersed in the electron density of the surface isopropoxide ligands with oxygen atoms shown in red and titanium in yellow. (b) A “molecular” view showing the central tetrahedral and the penta-coordinate Ti atoms at the corners of the cluster highlighted in green. For clarity, the radius of the oxygen atoms was reduced, while that of the Ti atoms was exaggerated. The $-\text{C}(\text{CH}_3)_2$ are shown in grey. The Spartan’10 renderings are based on the unrelaxed X-ray structure reported in reference.

The crystallographic structure of the polyoxotitanate core of Ti17 resembles most closely brookite, the least common metastable phase of crystalline TiO_2 [7]. The core of cluster is terminated by 20 isopropoxide groups (Figure 1b). As a result, outer shell of the cluster is for the most part hydrophobic, resulting in good solubility in even mildly polar

organic solvents. There are four five-coordinate titanium ions which form a square centered around the unique tetrahedral Ti ion positioned in the middle of the cluster (shown in green in Figure 1b). The remaining 12 Ti ions have most typical, 6-fold coordination. The system has an approximate S_4 rather than spherical symmetry, and there is considerable disorder in orientation of the isopropyl groups. The existence of nonequivalent and coordinatively unsaturated Ti sites has a significant influence on the electronic properties of the cluster.

Because titanium dioxide is a large band gap II-VI semiconductor with a strong ionic character[12, 13], the onset of quantum effects is expected to occur for much smaller particles than in the case of chalcogenides and other small band gap covalent solids. Serpone et al. concluded that quantum size effects were not significant in anatase particles down to 2.1 nm diameter, which corresponds to approximately 200 Ti atoms[14]; however, the oxotitanate core of Ti17 contains only 17 Ti atoms and is approximately 10 times smaller by volume. The X-ray diffraction of Ti17 confirms its unique core-shell structure, the size of the oxotitanate core of Ti17 is ~ 1 nm which contains only 17 Ti atoms and 24 O atoms, its furthest Ti centers span 8.3 \AA , and the maximum distance between the surface oxygen atoms is 11.4 \AA . At these dimensions the size confinement effect should be very obvious and will reflect on its many properties. The line shape analysis performed by Benedict and Copens placed the band edge of Ti17 at 4.3 eV ($\sim 290 \text{ nm}$) and the lowest indirect transition at 3.4 eV ($\sim 365 \text{ nm}$) [7].

We have found that the small size of the cluster has an even more dramatic influence on the spectral properties of Ti17^* and $\text{Ti17}^{\cdot\cdot}$ than on the ground state absorption. In bulk semiconductors and large nanoparticles, excitons can dissociate and form free carriers.

The exciton binding energy is as small as 4 meV and 20 meV (approximately only 1 $k_B T$) in rutile and anatase[12, 13], respectively. Due to the confinement in Ti17 the charges remain strongly coupled together and cannot fully dissociate. Classical Coulomb interaction calculated at the maximum electron-hole separation permitted by the 1 nm diameter of the TiO core of the cluster is approximately 250 meV, i.e., equivalent to 10 $k_B T$ at room temperature. Better estimates can be obtained using Brus type expressions [1, 3, 4] which account for the electron-phonon and hole-phonon coupling (nuclear reorganization in the molecular terminology) by introducing an adjustable effective mass for both charges; however, since these parameters are not known for the cluster, we will use the rough value of 0.25 eV as a convenient zeroth-order reference point.

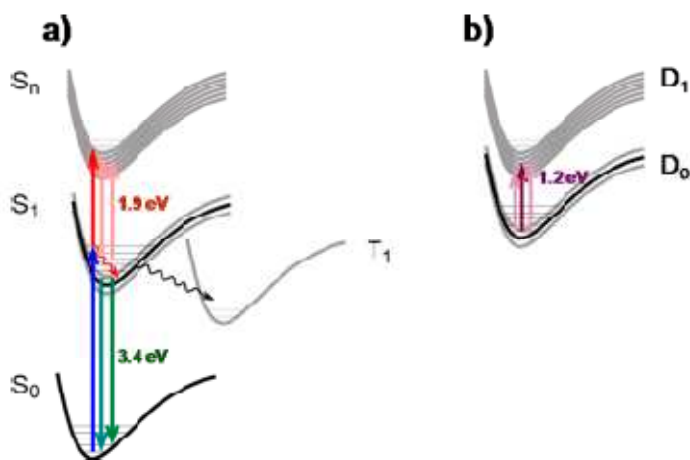


Figure 3-2. Tentative energy level diagrams of: (a) The neutral Ti17 polyoxotitanate cluster and (b) the $Ti17^{\bullet-}$ reduced species carrying the excess electron

The simple core-shell picture presented in Figure 1a cannot fully account for the behavior of Ti17 and that a molecular view of the cluster is more appropriate. We propose tentative energy level diagrams for Ti17 and $Ti17^{\bullet-}$ radical anion shown in

Figure 3-2. Because of the strong electron-hole coupling, the absorption spectrum of the exciton is shifted to a much higher frequency than in bulk TiO_2 . The broad spectra of $\text{Ti17}^{\cdot\cdot-}$ and Ti17^* are consistent with a sequence of closely lying higher electronic states, S_n and D_n , respectively. The existence of the T_1 triplet is inferred from the multicomponent charge recombination dynamics and from the large magnitude of the electron-hole coupling, which suggests there is sizable exchange interaction in the Ti17^* excited state. The fluorescence and Raman spectra indicate that the atomic-level structure of the core-shell interface and the vibrational modes of the ligands play a very important role in stabilizing the S_1 excited state and the manifold of S_n states as well as between the D_0 ground state and the D_n manifold of doublets is not consistent with the bulk-like picture of Ti17 . We postulate that the S_1 and D_0 states are rather tightly localized and stabilized by nuclear reorganization at the core-ligand interface, while the higher, densely spaced S_n and D_n states involve primarily the orbitals of the polyoxotitanate core and hence are of a more bulk-like character.

3.2 Results and discussion

3.2.1 Steady state absorption:

The UV-Vis spectrum of Ti17 in dibutyl ether exhibits an ~ 330 nm (3.75 eV) band edge absorption, the line shape analysis performed by Benedict and Coppens [7] placed the band edge of Ti17 at 4.3 eV (~ 290 nm) and the lowest indirect transition at 3.4 eV (~ 365 nm). The result manifests the quantum size effect on ground state absorption of Ti17 cluster by comparing to the reported band gap of 3.35 eV (370 nm) for 2.4 nm particles[15].

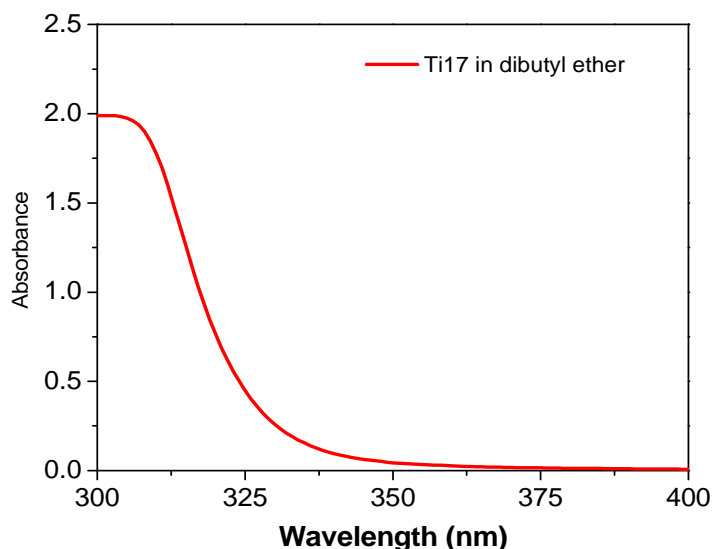


Figure 3-3. The UV-Vis spectrum of Ti17 in dibutyl ether

3.2.2 Fluorescence spectra of Ti17:

Ti17 exhibits a UV fluorescence band peaking at 365 nm. The emission is broad and extends into the violet portion of the visible spectral range. Although the emission is weak, $\Phi \leq 1\%$, it can be readily measured even at room temperature (Figure 3-4). This finding is significant because it provides additional valuable information about the electronic structure of the cluster. The position of the maximum at 365 nm is in perfect agreement with the indirect band gap of 3.36 eV deduced by Benedict and Coppens on the basis of their analysis of the absorption onset of Ti17[7]. Furthermore, the fluorescence band shows two discernible vibronic peaks separated by approximately $1290 \pm 150 \text{ cm}^{-1}$ which is very close to the value we obtained from Ti6 emission spectrum $1305 \pm 50 \text{ cm}^{-1}$. The coupling between the emissive exciton and the high frequency mode offers hints about the charge localization in the fully relaxed excited state.

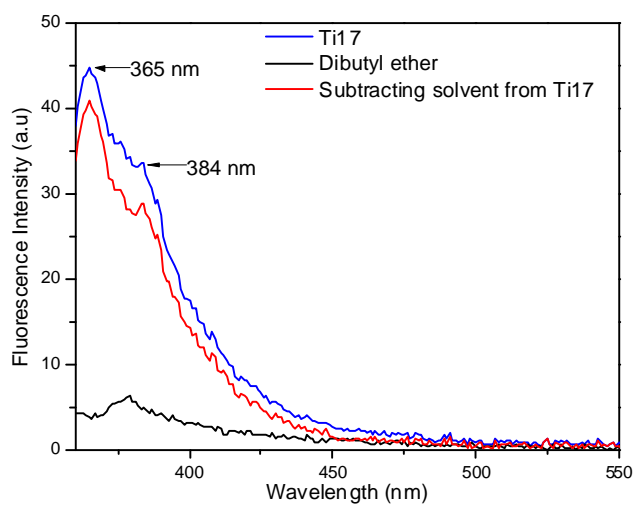


Figure 3-4. Room temperature fluorescence spectrum of Ti17 in dibutyl ether excited at 340 nm

3.2.3 Raman spectra of Ti17

The vibrational spectrum of the TiO core of the Ti17 cluster is similar to the brookite phase of TiO_2 (Table 1 and Figure 5) with a peak at a frequency of 644 cm^{-1} , i.e., much lower than the separation of the vibronic shoulders in the fluorescence spectrum.

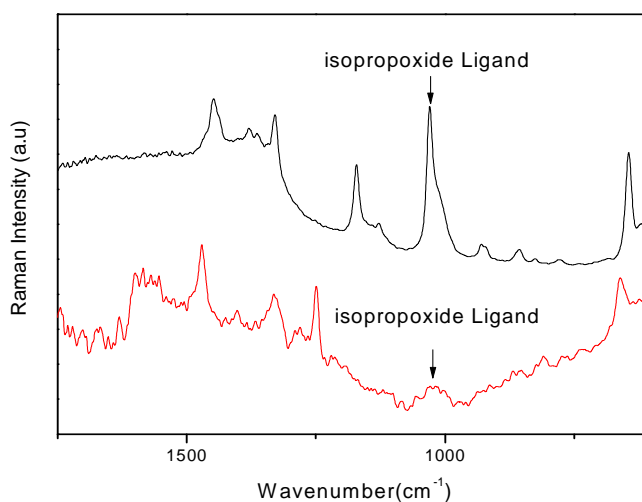


Figure 3-5. Raman spectrum of solid Ti17 (black) and Ti17cat4 (red)

Table 1. Raman mode comparison

	Ti17 cluster	brookite
Phonon frequency cm^{-1}	644, 592, 550	635, 585, 535

Therefore, it is doubtful that the vibronic structure of the fluorescence spectrum results from the coupling between the exciton and the core modes of the cluster. The involvement of the ligand modes at the organic–inorganic interface seems much more likely. Indeed, the ground state Raman spectrum of solid Ti17 shows a very prominent composite peak at 1030 cm^{-1} and another one at 1190 cm^{-1} (Figure 3-5) which correspond to the combination CO stretching and CH wagging modes of the isopropoxide ligands [16, 17] forming the organic shell of the cluster. We believe that the CO modes are responsible for the vibrational structure of the fluorescence band. If this hypothesis is correct, it would suggest at least one of the charges, most likely the hole of the relaxed exciton, is localized at the core–ligand interface, where it couples to the vibrations of the isopropoxide group.

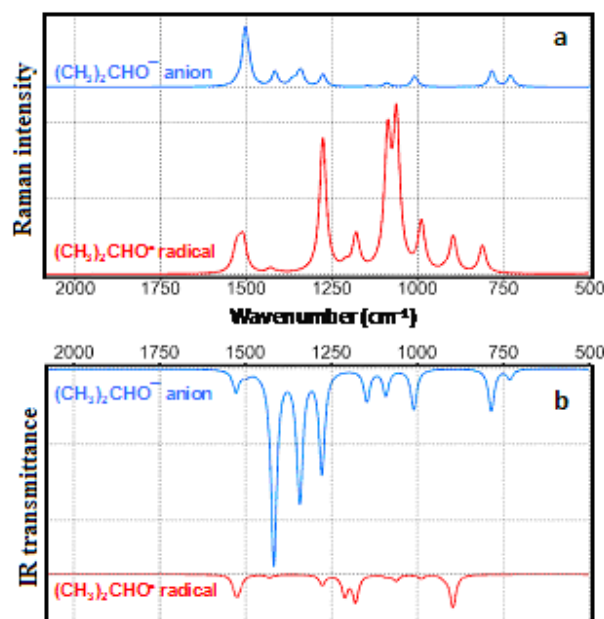


Figure 3-6. Calculated Raman (a) and IR (b) spectra of the isopropoxide anion (blue) and the oxo isopropoxyl radical (red). Calculations were performed at the B#LYP DFT level (Spartan'10) without frequency scaling.

The CO Raman bands of Ti17 originate almost exclusively from four ligands bound to the penta-coordinate Ti sites at the corners of the cluster. As it is depicted in Figure 1b and discussed in the Introduction, the cluster contains four five-coordinate and as a result coordinatively unsaturated Ti centers (shown in green) which are terminated with a single, strongly polarized isopropoxide ligand. Upon selective substitution of the five-coordinate Ti centers with bidentate catechol, all surface titanium sites of the resulting Ti17cat4 cluster become hexa-coordinate. But the strong CO band nearly completely disappears from the Raman spectrum, despite the fact that there are still 16 isopropoxide ligands which remain bound to the surface of the core. The explanation for this puzzling observation lies in the degree of the purely ionic vs. charge-transfer bonding interaction

between the ligand and the surface titanium centers. The CO modes of the closed-shell free isopropoxide ion are strong IR absorbers; however, because of the localized “hard” charge distribution, they are weak Raman scatters. This is illustrated by the calculated Raman and IR spectra shown in Figure 3-6. On the contrary, the same vibrational modes of the corresponding open-shell electroneutral oxo-radical are weak IR absorbers in the 750-1500 cm^{-1} region; however, they have much larger Raman cross sections (Figure 3-6, shown in red). This implies that any shift of electron density from the isopropoxide anion onto the metal will give rise to stronger Raman scattering in the CO region. It appears that isopropoxides bound to the hexa-coordinate Ti centers retain their primarily ionic character and that there is little charge shift between their oxygen atoms and the d-orbitals of the metals. As a result, they make only a minor contribution to the CO region of the Raman spectrum of Ti17. On the other hand, isopropoxides bound to the penta-coordinate Ti centers donate a large fraction of their charge to the d-orbitals of the titanium ions. Such electron density shift renders them considerably less ionic and increases the overall polarizability of the local -C-O-Ti- interface, leading to a strong Raman signature[18].

On the basis of the presented fluorescence and Raman data alone, it is not possible to decide whether the hole in the excited state of Ti17 becomes localized on one of the coordinatively unsaturated five-coordinate titanium centers or on one of the six-coordinate sites. High level calculations on the complete cluster will be necessary in order to settle this question. Nevertheless, it is safe to conclude that ligand modes at the interface play a more significant role in stabilizing the lowest electronic excited state of the Ti17 than either the solvent reorganization or the core frequencies. This further builds

the picture of a CT excited state with the hole localized at the core-ligand interface and the electron on the central tetrahedral titanium ion. The large ground state ligand-to-metal charge shift at the five-coordinate centers make these sites behave as reactive “hot-spots” on the surface of the cluster and for this reason the ligand substitution reactions occur with high selectivity only at these Ti centers. The charge shift must also have an influence on the redox and potential catalytic activity of the cluster both in the ground and in the excited state.

3.2.3 Pump-probe transient absorption measurement

Excitation of Ti17 with 300 nm ~70 fs pulses results in the formation of the S_1 excited state which is characterized by a broad and featureless spectrum which spans nearly the entire visible range from 500 to 750 nm (Figure 3-7). The large spectral width, lack of structure, and gradual falloff on the high energy side are consistent with a closely spaced sequence of higher electronic states of the cluster (Figure 3-2). The transition to the closely lying S_2, S_n electronic states have diminishing oscillator strength and suggest the onset of continuum (ionization of the Ti17* excited state) at around 2.5 eV. The spectra in two solvents, dibutyl ether and benzonitrile, which differ considerably in polarity ($\epsilon = 4.3$ for the former and $\epsilon = 25.6$ for the latter), are nearly indistinguishable from one another. The spectrum in dibutyl ether does appear to be somewhat broader and possibly slightly red-shifted; however, even in the presence of these minor differences, one must conclude that the influence of solvent polarity on the spectrum of Ti17* is small. This suggests that the isopropoxide ligands, which form a dense cover on the surface of the cluster, reduce the solvation effects by shielding the core of the cluster

from the surrounding medium. In essence, the ligands themselves act as solvation shell for the exciton and diminish the polarization of the bulk solvent. Alternatively, such weak solvent dependence could indicate that the relaxed S_1 state has little CT character and that the electron and hole are not spatially well separated. This explanation is unlikely given the presence of nonequivalent Ti centers and the ionic nature of the TiO core.

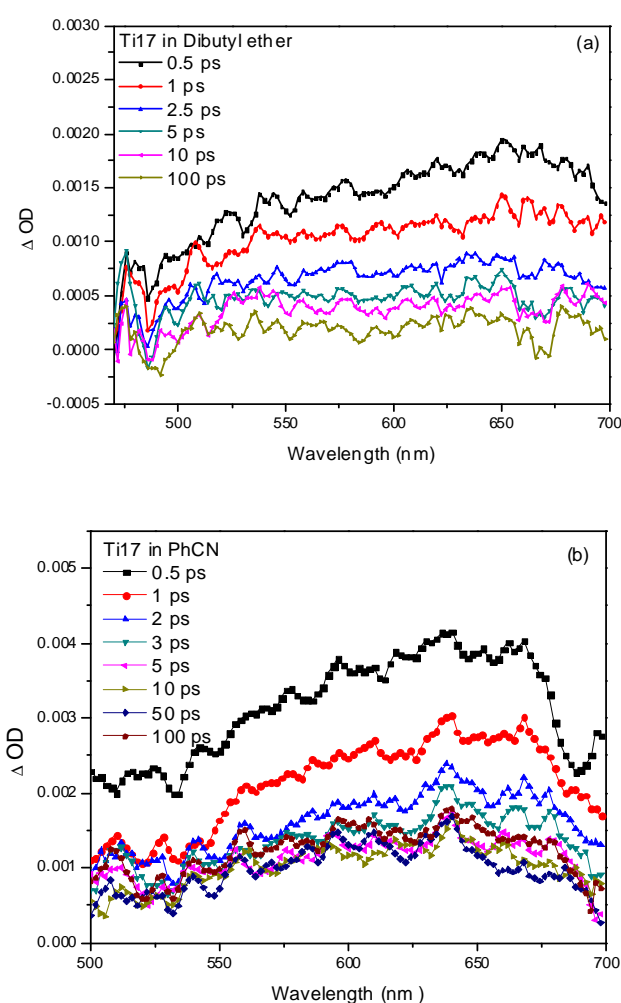


Figure 3-7. Femtosecond pump-probe transient absorption spectra of the Ti17* excited state in (a) dibutyl ether, $\epsilon = 4.3$; (b) benzonitrile, $\epsilon = 25.6$.

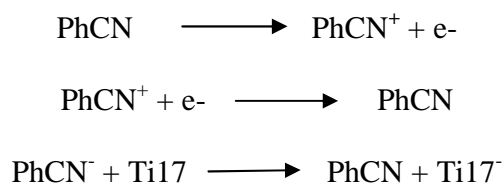
The 650 nm (1.9 eV) maximum of the Ti17* spectrum lies at a much higher energy than that for bulk exciton or conduction band electron TiO₂, which also has a very broad and featureless spectrum with $\lambda_{\text{max}} > 10\,000\text{ nm}$, i.e., $< 0.1\text{ eV}$ [12]. This dramatic blue shift of 1.8 eV points to the presence of strong quantum size effects and increased electron-hole coupling in the 1nm cluster, as discussed in the Introduction. In order to confirm that Ti17* does not have lower-lying electronic transitions, we also probed the response of the directly excited cluster and anatase in the near IR (1200-1400 nm) and IR (2650 nm) spectral regions. The transient dynamics for Ti17 and a mesoporous TiO₂ film at 2.65 μm are shown in Figure 3-9c. The TiO₂ film shows a strong absorption in agreement with the findings of Katoh *et al.*:[19] however, the only signal that we were able to detect in the case of Ti17 is the small nonlinear artifact at $t=0$. This verifies that Ti17* has no low-lying electronic transitions below the 700 nm. It should be mentioned that photoexcited Ti17, unlike rutile or anatase, does not give a response in the terahertz frequency range[20]. The lack of IR and terahertz absorption corroborates the presence of strong electron-hole coupling in Ti17* and suggests that the cluster does not have a true conduction band. It is more likely that the appearance of the spectrum of Ti17* is due to a sequence of closely spaced localized and delocalized *d-d* transitions in the core of the cluster.

3.2.4 Pulse radiolysis measurement

In bulk semiconductors the exciton binding is only 4 meV in rutile and 20 meV in anatase [12, 13]. These values contain both the direct electrostatic interaction and the lattice relaxation (phonon trapping) effects. Because the perturbation is small, the

absorption spectra of the exciton and the free conduction band electron are usually very similar to one another. Furthermore, at room temperature, the exciton rapidly dissociates into free carriers. Due to the size of Ti17, ~1 nm diameter particle, the two charges cannot fully dissociate even if the phonon effect were negligible. Since the exciton in Ti17 cannot fully dissociate, the electron and the hole remain coupled by the large Coulomb interaction and the absorption spectra of Ti17^* and Ti17^- should differ markedly. The comparison of the absorption spectra of Ti17^- and Ti17^* offers insights into the interplay between the pure “particle-in-the-box” confinement which in the zeroth-order approximation affects only the kinetic energy of the excess electron in Ti17^- and the Coulomb and exchange interactions, which are also modified by the restricted space available to the electron-hole pair in Ti17^* [2-4].

We used pulse radiolysis to generate Ti17 free radical. In this experiment we chose benzonitrile as solvent. Benzonitrile is polar solvent and the concentration of Ti17 cluster is very low (1 mg/ml). The major electrons produced by electron pulses are in solvated form, and some of solvent molecules are radiated to generate benzonitrile radical cation and electrons. The solvated electrons transfer to clusters through diffusion to produce Ti17 free radical, as shown in the series reactions.



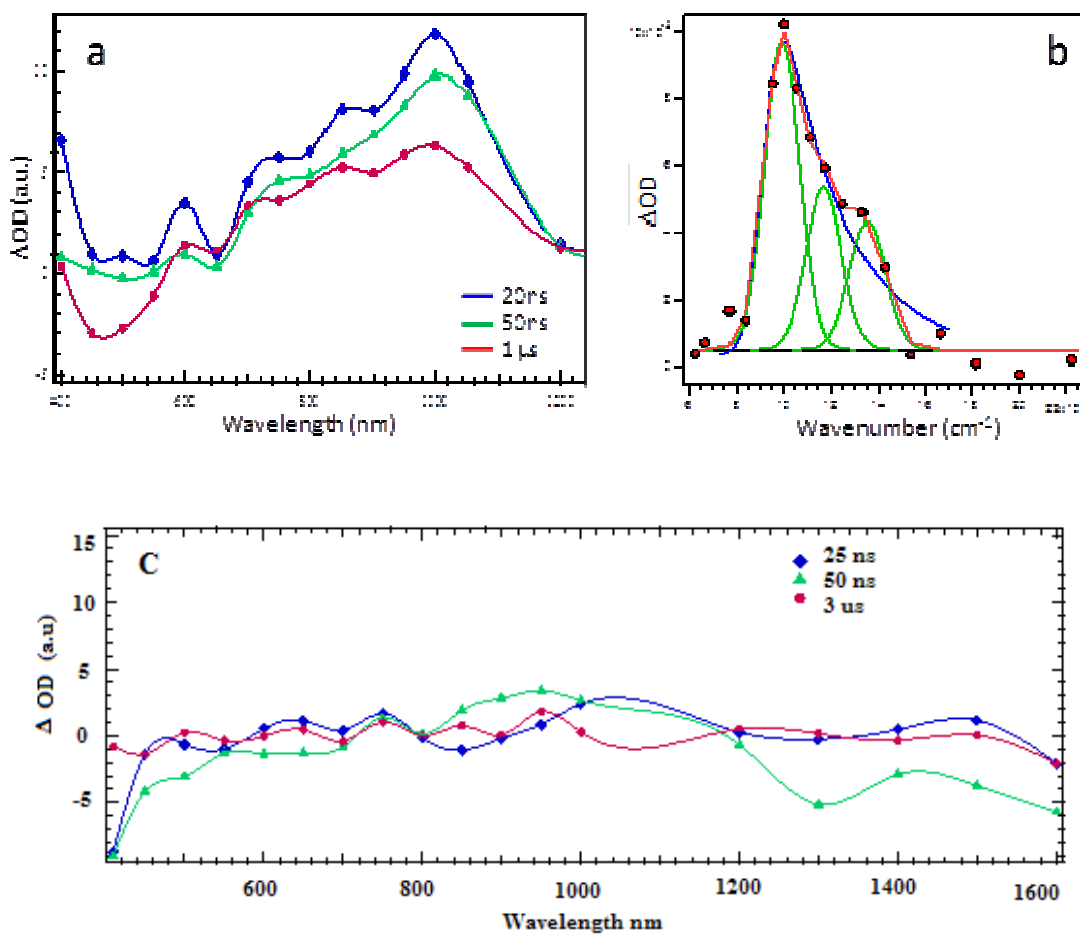


Figure 3-8. (a) Absorption spectra of the Ti17^* species at different delay times obtained by picosecond pulse radiolysis in benzonitrile. (b) Gaussian (green) and stretched Gaussian (blue) line shape fitting of the Ti17^* absorption band obtained at 50 ns delay. The solid red line is the sum of the three Gaussian functions calculated only at the frequencies of the experimental data. (c) Absorption spectra of Ti17^* solution after being purged with SF_6

The resulting spectrum of e^- in the “conduction band”, or the lowest unoccupied orbital of the cluster, is shown in Figure 3-8a. The broad and highly asymmetric absorption band of the excess electron appears at a much longer wavelength than the spectrum of Ti17^* . The absorption maximum lies at 1000 nm (1.24 eV), i.e., more than 1.1 eV higher than that of the conduction band electron in bulk TiO_2 and 0.67 eV lower than

that of the Ti17^* exciton, simultaneously confirming the presence of pronounced quantum size effects in $\text{Ti17}^{\cdot\cdot}$ and strong electrostatic interaction between the electron and the hole in Ti17^* . The rise on the low energy side is very sharp, while the high energy falloff is much more gradual. The spectrum cannot be satisfactorily fitted with a single Gaussian or Lorentzian line shape; however, a sequence of three 1900 cm^{-1} wide Gaussian peaks centered at 9920 , $11\,710$, and $13\,550\text{ cm}^{-1}$ reproduces it perfectly (Figure 3-8b, green lines). Given the low resolution of the experimental spectrum, one should not over interpret the origin of the modulation seen in Figure 3-8a; A single Gaussian convoluted with an exponential function gives a very satisfactory fit, too (Figure 3-8b, blue line). Nonetheless, the asymmetric shape of the band alone indicates that it consists of a sequence of transitions to a series of closely spaced higher states with diminishing oscillator strength, similarly as the spectrum of Ti17^* , albeit shifted to lower energy. It is more likely that these are closely lying higher electronic doublet states D_2, \dots, D_n shown in Figure 3-2b rather a vibronic progression of the same electronic transition. Indeed, the apparent $\sim 1800\text{ cm}^{-1}$ separation between the features does not correspond to any vibrational mode of the TiO core or the ligands. Better resolved spectra of $\text{Ti17}^{\cdot\cdot}$ are needed to address this point in more detail.

There is 0.67 eV energy difference between the spectra of $\text{Ti17}^{\cdot\cdot}$ and Ti17^* , the value can be used to set a rough limit for the electron-hole distance in the relaxed excited state of Ti17 . In a vacuum, 0.67 eV corresponds to the potential energy of two point charges separated by $\sim 2.1\text{ nm}$, i.e., further apart than both the diameter of the TiO core and the size of the entire Ti17 cluster. Scaled by the high frequency dielectric constant of anatase,

$\epsilon_{\text{opt}} \approx 6$, the estimated electron-hole separation is reduced to $r^{+-} = 0.35$ nm. This value is nearly identical with the 3.50 Å distance between the central tetrahedral and the outer, six-coordinate Ti atoms and it is only slightly shorter than the 4.2 Å distance between the center of the cluster and the five-coordination Ti atoms based on the X-ray diffraction structure determination[7]. This crude classical electrostatic estimation ignored the charge delocalization, the atomic structure of the medium and exchange interaction and should be taken with caution. Even the use of the bulk dielectric constant of anatase is questionable, since it has been convincingly argued that in nanoparticles the effective ϵ is lower[21]. Nevertheless, they suggest that the relaxed exciton in Ti17 has substantial charge-separated character, most likely with the electron occupying the tetrahedral center of the cluster and the hole localized at the electron-rich Ti-isopropoxide interface between the core and the ligand shell. The emerging picture of a charge transfer excited state and the involvement of the ligand-core interface are corroborated by the fluorescence and Raman spectroscopy results were already discussed. Excited states of other polyoxometalates (POMs), e.g., the $[\text{W}_{10}\text{O}_{32}]^{4-}$, are also believed to be of the LMCT (ligand-to-metal charge-transfer) character, with the electron residing at one of the metal centers [6]. Furthermore, in colloidal TiO_2 , the conduction band electron localizes on the coordinatively unsaturated Ti ions.

The large Coulomb interaction in the excited state of Ti17 suggests that the exchange coupling K between the unpaired HOMO-LUMO electrons is also substantial in this system. As mentioned earlier, the 0.67 eV spectral shift observed for the Ti17* exciton in comparison with the $\text{Ti17}^{\cdot-}$ radical anion is a composite result of both interactions. Exchange interaction K raises the energy of the singlet exciton by K and lowers the

energy of the otherwise degenerate triplet state by the same amount. Coulomb and exchange integrals have different distance dependence, with the short-range part of the latter scaling as the inverse of the common volume sampled by the unpaired spins [22-24]. If we accept the 2.35 nm Bohr radius of the free exciton in anatase deduced recently by Hormann et al[25] and combine it with the particle size dependence of the electron-hole exchange energy derived by Takagahara[22], an over 100-fold increase in the exchange interaction is predicted for the Ti17 cluster in comparison with bulk anatase TiO_2 . For a reference, in the case of the fully delocalized-electron system of C60, which is similar in size to Ti17, the singlet-triplet splitting is on the order of 0.3-0.4 eV[26, 27]. Naturally, any localization of the hole and the electron away from one another through charge separation or phonon coupling, both of which certainly take place in Ti17*, will affect these values. Nevertheless, as long as the singlet-triplet splitting remains greater than the thermal energy, $E_{S-T} = 2|K| > k_b T$, it is likely to manifest itself in the excitation recombination dynamics as a slow decay channel which should appear in the time-resolved transient absorption experiments.

The issue of the electron-hole exchange interaction and the resulting singlet-triplet splitting is of great importance for quantum confinement effects at the smallest particle size limit. One should note that the size dependence position of the triplet state in the band gap or HOMO-LUMO gap of the species has implications for the emission efficiency of quantum dots, as well as the multiple exciton generation (MEG)[19] and singlet fission (SF) processes which have been attracting a lot of attention recently because of their potential importance for solar energy conversion. Both phenomena critically depend on the spacing between the energy levels which participate in the

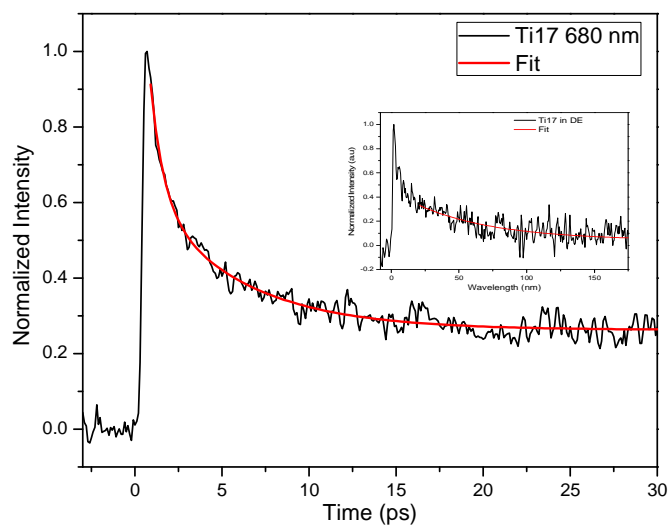
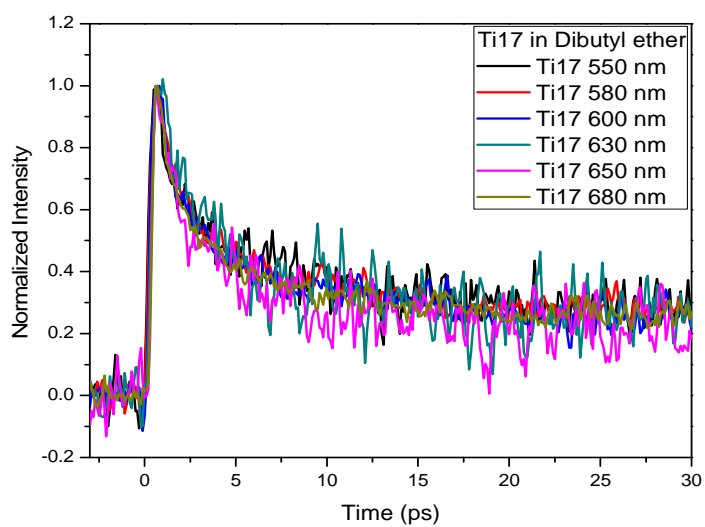
partitioning of the initial excitation. The possibility of using the size and shape of the particle to control the electron-hole exchange interaction[22, 28] and hence being able to place the triplet exciton at an arbitrary position within the band gap opens attractive possibilities for the design of light conversion materials. We plan to address the possible involvement of triplet excitons in the photophysics of Ti17 by low temperature luminescence and transient absorption studies.

3.2.5 Pump-probe transient dynamics measurement

The broad transient absorption spectra of the Ti17* excited state decay homogeneously, as shown in Figures 7. Similarly to the Ti17 absorption spectrum, its decay dynamics is weakly dependent on solvent polarity and the systematic differences between the benzonitrile and dibutyl ether results were smaller than the fitting uncertainties. This further supports the picture of an exciton shielded from the solvent by the ligand shell.

Table 3-2. Time constants of exciton decay of Ti17 cluster

τ_1 (ps)	A_1	τ_2 (ps)	A_2	τ_3 (ps)	A_3	A_∞
0.75±0.2	0.31±0.06	5.3±0.8	0.34±0.04	102±18	0.28±0.04	0.07±0.05



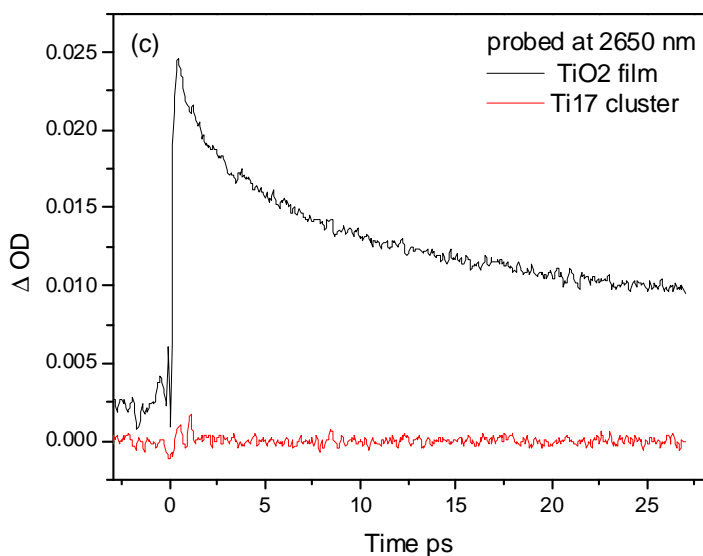


Figure 3-9. Overlaid normalized transients collected at several wavelengths from 550 to 680 nm showing homogeneous decay kinetics. (b) Decay of the excited state of Ti17 in dibutyl ether monitored at 680 nm fitted with a tri-exponential function. (c) IR transient responses of the Ti17 cluster and anatase film

The kinetics in the 0-30 ps time window is dominated by two components, $\tau_1 = 0.75$ and $\tau_2 = 5.3$ ps, which together constitute more than 60% of the overall decay (Figure 3-9 and Table 3-2). Since the pump-probe data were collected in the “magic angle” configuration and the spectral evolution is minor, these rates reflect the population decay. The fast subpicosecond rate most likely corresponds to the geminate recombination of the initial electron-hole pairs which did not fully equilibrate with the $500\text{-}640\text{ cm}^{-1}$ phonon modes of the TiO core of the cluster (Table 3-1). The surviving excitons follow two paths: they either decay with the rate τ_2 , which is consistent with vibrational cooling, or acquire charge transfer character with one of the charges stabilized at the core-ligand interface, consistent with the view that in small nanocrystallites the interaction with the surface dominates the electron and hole dynamics[1]. Skinner et al. found that in

colloidal TiO₂ the electron localizes within a picosecond on coordinatively unsaturated Ti centers[29], which in the case of Ti17* suggests the central tetrahedral Ti atom (Figure 3-1b) as the location of the negative charge in the relaxed excited state. Longer scans up to 300 ps (Figure 3-9b, Table 3-2) allow us to determine the third decay time, $\tau_3 = 102$ ps, which we ascribe to the recombination of the fully relaxed, surface-stabilized exciton. Only less than 30% of the initial excited state population reaches this stage.

Fitting of the long scan transients always returned a 5-10% A_∞ component which does not decay at the 300 ps time scale. We cannot rule out the presence of small amounts of impurities or photodamage of the cluster itself, even though precautions were taken to minimize the latter, it is plausible that the longest lived absorption originates from the “dark” intraband states, i.e., triplet excitons $^3\text{Ti17}^*$, or in the molecular terminology, simply the T_1 triplet state of the cluster (Figure 3-2). As we discussed in transient absorption, the electron-hole coupling in the confined space of Ti17 appears to be large, on the order of 6000 cm^{-1} or $30 k_bT$. This coupling consists of the Coulomb and exchange interaction, the latter of which leads to the singlet-triplet splitting of the excited state. One cannot easily determine the partitioning of the overall interaction into the Coulomb and exchange. However, if the S-T splitting is larger than k_bT , which it is very likely to be given the large magnitude of the overall electron-hole interaction, a distinct, slower recombination dynamics of the triplet exciton should be expected.

3.3 Conclusions

The 1 nm diameter $\text{Ti}_{17}(\mu_4\text{-O})_4(\mu_3\text{-O})_{16}(\mu_2\text{-O})_4(\text{OPr}^i)_{20}$ polyoxotitanate cluster with a brookite-like core displays complex photophysics which combines primarily molecular

characteristics with some traits typical of larger nanoparticles and bulk TiO_2 . The high frequency modes at the ligand-core interface were found to play a key role in the stabilization and localization of the excited state. On the basis of our results, we proposed a tentative energy level diagram of the cluster (Figure 3-2). Due to spatial confinement, the absorption spectrum of the D_0 ground state of the $\text{Ti17} \cdot^-$ radical anion is shifted from the IR range typical of the excess electron in bulk II-VI oxides [19, 30, 31] to 1000 nm. The spectrum of the S_1 excited state of the cluster is blue-shifted even further, indicating the presence of large Coulomb and exchange interactions between the spatially confined electron and hole. The appearance of the broad and featureless spectra of S_1 and D_0 states of Ti17 is consistent with band-like progressions of closely lying upper electronic states, S_n and D_n respectively. It is likely that the higher states involve primarily the TiO core of Ti17 and therefore are of more bulk-like character than the lowest states. DFT calculations show a large Ti d-orbital contribution to low-lying empty orbitals of the cluster, suggesting that the S_1 and D_1 spectra of Ti17 may be due to d-d transitions.

The electron-hole recombination in Ti17 is faster than in colloidal anatase or mesoporous films of TiO_2 , however, it does not follow single exponential decay. The fast, 0.7-5 ps components, which account for ~60% of the decay, most likely originate from the recombination of the initial excitons before they relax and become stabilized at the core-ligand interface. The slower, 100 ps component is assigned to the decay of the fully relaxed exciton. Lastly, we consistently detected a long-lived component accounting for 5-10% of the initial population which we tentatively ascribe to the formation of a lower-lying triplet state with a distinct, slower recombination dynamics.

Our finding suggest that the relaxed excited state of Ti17 has charge transfer character, with one of the charges (hole) localized at the core-ligand interface and the other on the unique tetrahedral Ti at the center of the cluster. The vibronic features of the emission spectrum as well as the ground state Raman spectra show that the ligand modes are strongly coupled to the overall electron density of the cluster. Polyoxometalates and colloidal TiO_2 have been successfully employed in a number of photocatalytic reactions[5, 6], and there are indications that the brookite phase possesses more reactive surface sites than either anatase or rutile[16, 17]. A better understanding of the localization and dynamics of electrons and holes in clusters similar to Ti17 should facilitate further development of catalytic applications of this class of materials.

References

1. Alivisatos, A., et al., *Electronic states of semiconductor clusters: Homogeneous and inhomogeneous broadening of the optical spectrum*. The Journal of Chemical Physics, 1988. **89**(7): p. 4001-4011.
2. Brus, L., *A simple model for the ionization potential, electron affinity, and aqueous redox potentials of small semiconductor crystallites*. The Journal of Chemical Physics, 1983. **79**(11): p. 5566-5571.
3. Brus, L.E., *Electron - electron and electron - hole interactions in small semiconductor crystallites: The size dependence of the lowest excited electronic state*. The Journal of Chemical Physics, 1984. **80**(9): p. 4403-4409.
4. Brus, L., *Electronic wave functions in semiconductor clusters: experiment and theory*. The Journal of Physical Chemistry, 1986. **90**(12): p. 2555-2560.
5. Pope, M., *Polyoxometalates: From Platonic Solids to Anti-Retroviral Activity: From Platonic Solids to Anti-Retroviral Activity*. Vol. 10. 1994: Springer Science & Business Media.
6. Duncan, D.C., T.L. Netzel, and C.L. Hill, *Early-time dynamics and reactivity of polyoxometalate excited states. Identification of a short-lived LMCT excited state and a reactive long-lived charge-transfer intermediate following picosecond flash excitation of [W10O32] 4-in acetonitrile*. Inorganic Chemistry, 1995. **34**(18): p. 4640-4646.
7. Benedict, J.B. and P. Coppens, *The Crystalline Nanocluster Phase as a Medium for Structural and Spectroscopic Studies of Light Absorption of Photosensitizer Dyes on Semiconductor Surfaces*. Journal of the American Chemical Society, 2010. **132**(9): p. 2938-2944.
8. Benedict, J.B., et al., *Large Polyoxotitanate Clusters: Well-Defined Models for Pure-Phase TiO₂ Structures and Surfaces*. Journal of the American Chemical Society, 2010. **132**(39): p. 13669-13671.
9. Ardo, S. and G.J. Meyer, *Photodriven heterogeneous charge transfer with transition-metal compounds anchored to TiO₂ semiconductor surfaces*. Chemical Society Reviews, 2009. **38**(1): p. 115-164.
10. Fujishima, A. and K. Honda, *Electrochemical photolysis of water at a semiconductor electrode*. Nature, 1972(238): p. 37-8.

11. Linsebigler, A.L., G. Lu, and J.T. Yates Jr, *Photocatalysis on TiO₂ surfaces: principles, mechanisms, and selected results*. Chemical Reviews, 1995. **95**(3): p. 735-758.
12. Chiodo, L., et al., *Self-energy and excitonic effects in the electronic and optical properties of TiO₂ crystalline phases*. Physical Review B, 2010. **82**(4): p. 045207.
13. Hendry, E., et al., *Electron transport in TiO₂ probed by THz time-domain spectroscopy*. PHYSICAL REVIEW-SERIES B-, 2004. **69**(8): p. 081101 (R)-081101 (R).
14. Serpone, N., D. Lawless, and R. Khairutdinov, *Size effects on the photophysical properties of colloidal anatase TiO₂ particles: size quantization versus direct transitions in this indirect semiconductor?* The Journal of Physical Chemistry, 1995. **99**(45): p. 16646-16654.
15. Kormann, C., D.W. Bahnemann, and M.R. Hoffmann, *Preparation and Characterization of Quantum-Size Titanium-Dioxide*. Journal of Physical Chemistry, 1988. **92**(18): p. 5196-5201.
16. Koelsch, M., et al., *Comparison of optical and electrochemical properties of anatase and brookite TiO₂ synthesized by the sol-gel method*. Thin Solid Films, 2002. **403**: p. 312-319.
17. Lin, H., et al., *Synthesis of high-quality brookite TiO₂ single-crystalline nanosheets with specific facets exposed: Tuning catalysts from inert to highly reactive*. Journal of the American Chemical Society, 2012. **134**(20): p. 8328-8331.
18. Moran, P.D., et al., *Vibrational spectra and molecular association of titanium tetrakisopropoxide*. Inorganic Chemistry, 1998. **37**(11): p. 2741-2748.
19. Yoshihara, T., et al., *Identification of reactive species in photoexcited nanocrystalline TiO₂ films by wide-wavelength-range (400-2500 nm) transient absorption spectroscopy*. The Journal of Physical Chemistry B, 2004. **108**(12): p. 3817-3823.
20. Schmittenmaer, C.p.c.
21. Wang, L.W. and A. Zunger, *Solving Schrödinger's equation around a desired energy: application to silicon quantum dots*. The Journal of Chemical Physics, 1994. **100**(3): p. 2394-2397.
22. Takagahara, T., *Effects of dielectric confinement and electron-hole exchange interaction on excitonic states in semiconductor quantum dots*. Physical Review B, 1993. **47**(8): p. 4569.

23. Scholes, G.D., *Insights into excitons confined to nanoscale systems: electron–hole interaction, binding energy, and photodissociation*. ACS nano, 2008. **2**(3): p. 523-537.
24. Scholes, G.D. and G. Rumbles, *Excitons in nanoscale systems*. Nature materials, 2006. **5**(9): p. 683-696.
25. Hörmann, U., et al. *Structure and luminescence of sol-gel synthesized anatase nanoparticles*. in *Journal of Physics: Conference Series*. 2010: IOP Publishing.
26. Foote, C.S., *Photophysical and photochemical properties of fullerenes*, in *Electron Transfer I*. 1994, Springer. p. 347-363.
27. Arbogast, J.W., et al., *Photophysical properties of sixty atom carbon molecule (C60)*. The Journal of Physical Chemistry, 1991. **95**(1): p. 11-12.
28. Brovelli, S., et al., *Nano-engineered electron–hole exchange interaction controls exciton dynamics in core–shell semiconductor nanocrystals*. Nature communications, 2011. **2**: p. 280.
29. Skinner, D.E., et al., *Femtosecond investigation of electron trapping in semiconductor nanoclusters*. The Journal of Physical Chemistry, 1995. **99**(20): p. 7853-7856.
30. Yamakata, A., T.-a. Ishibashi, and H. Onishi, *Time-resolved infrared absorption spectroscopy of photogenerated electrons in platinized TiO₂ particles*. Chemical Physics Letters, 2001. **333**(3): p. 271-277.
31. Yoshihara, T., et al., *Quantitative estimation of the efficiency of electron injection from excited sensitizer dye into nanocrystalline ZnO film*. The Journal of Physical Chemistry B, 2004. **108**(8): p. 2643-2647.

Chapter 4. Charge Transfer and Hole Hopping in Ti17cat4

4.1 Introduction

The Ti17cat4, a molecular polyoxotitanate cluster (proper name $\text{Ti}_{17}(\mu_4\text{-O})_4(\mu_3\text{-O})_{16}(\mu_2\text{-O})_4(\text{OPr}^i)_{16}(\text{Catechol})_4$) is a derivative of Ti17 cluster(as shown in **Figure 1.**), it is prepared via Ti17 reacting with catechol which selectively substitutes four isopropoxide ligands on penta-coordination Ti atoms[1]. The four catechol ligands locate on the circumference of the inorganic core which consists of 17 titanium and 24 oxygen atoms. The ligand replacement turns the white Ti17 cluster into dark brown particle due to the strong charge transfer (CT) absorption from catechol to Ti17 cluster. Catechol modified TiO_2 nanoparticles is the archetype of a strongly coupled interfacial electron transfer (ET) system, which results in the mixing between the empty orbitals of the molecular donor and the conduction band (CB) of TiO_2 and gives rise to a new, long wavelength transition from HOMO of the donor to the semiconductor[2, 3]. In such strongly coupled systems, the distinct steps of the formation of a localized excited state and subsequent phonon-assisted electron tunneling are bypassed in a single photoinduced ET event that is instantaneous on the timescale of nuclear motion. Because the instantaneous electron injection occurs in the Franck-Condon geometry of the system, catechol sensitized TiO_2 and similar strongly coupled assemblies are well suited for experimental and theoretical investigations of the initial dynamics of interfacial charge separation and geminate electron-hole recombination[4]. The Ti17cat4 cluster is a strict

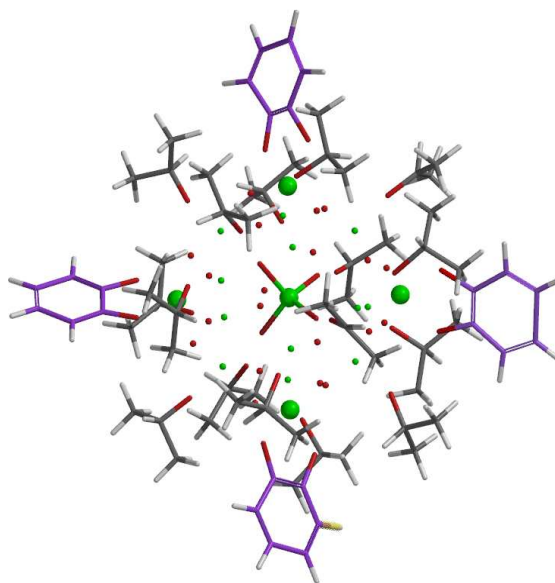


Figure 4-1. Structure of Ti17cat4 cluster

molecular analogue of cat@TiO_2 , due to the perfect monodisperse stoichiometry, geometry and ligand attachment. In this chapter, the excited state dynamics of Ti17cat4 has been studied through femtosecond transient absorption spectroscopy and quantum dynamics calculation.

In recent years, several molecular polyoxotitanate clusters containing from 2 to 48 Ti centers were synthesized and their X-ray structures were determined[5], greatly facilitating advanced studies of photophysics of these fascinating species. Ti17 cluster[6] (proper name $\text{Ti}_{17}(\mu_4\text{-O})_4(\mu_3\text{-O})_{16}(\mu_2\text{-O})_4(\text{OPr}^i)_{20}$), the parent compound of Ti17cat4, displays the quantum confinement effects on its electron-hole coupling and exciton dynamics. For both clusters they contain same size titanium oxide core, ~ 1.2 nm, and in terms of size and the complexity of the behavior Ti17cat4 lies between mononuclear LMCT complexes $[\text{Ti}(\text{cat})_3]^{2-}$ and the dye-sensitized anatase which was studied by Lian

et al[2]. In contrast with the latter, the Ti17cat4 is flawlessly homogeneous, free of traps and imperfections.

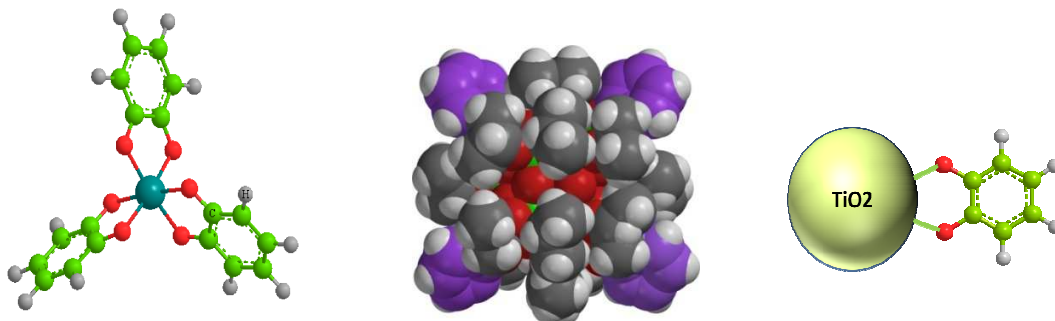
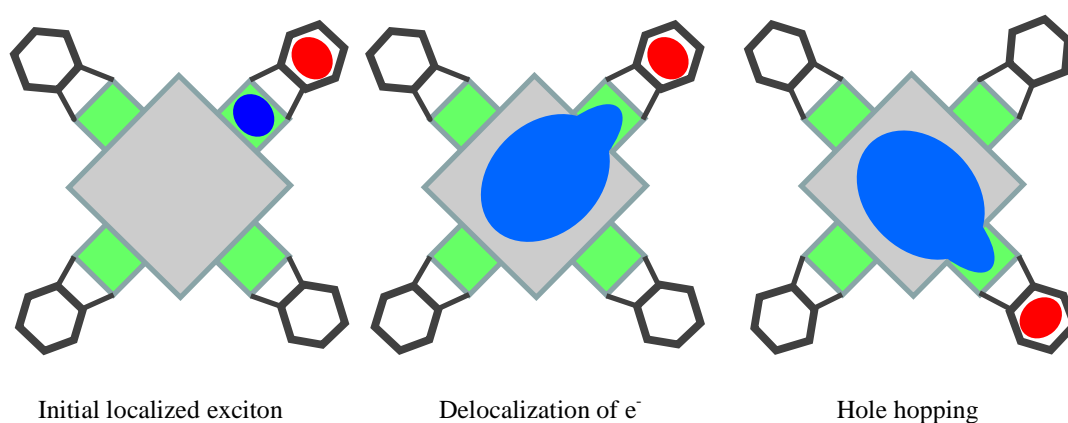


Figure 4-2. From left to right: (a) the mononuclear $[\text{Ti}(\text{cat})_3]^{2-}$ complex; (b) Ti17cat4 polyoxotitanate cluster; (c) schematic representation of a dye-sensitized TiO_2 nanoparticle.

Besides the fundamental aspects of interfacial electron transfer, the monodisperse clusters containing multiple transition metal centers are capable of reversibly accepting or donating more than one electron due to their size. As a result, these well-defined molecular “charge storage devices” could be creatively applied in light driven multi-electron catalysis[7]. Excited state behavior of large molecular clusters in solution has been little explored in the past, especially in comparison with the vast body of data on the excited state properties of colloidal nanoparticles of various materials. The literature on the photophysics of stable, monodisperse clusters has only recently begun to grow.

Based on the experimental results and the electronic states of the Ti17 cluster, we propose the sequential photophysical events which may occur in the investigated cluster. Scheme 1 is used to visualize the promising events occurring in the cluster upon the excitation. First the light absorption leads to instantaneous charge transfer from π orbital of catechol to the conduction band of cluster, and forming the localized exciton at the interface, and then followed by a charge separation process which is supported by the

transient absorption spectra in acetonitrile. The oxidized catechol and injected electron absorb at different wavelength. The injected electron will delocalize to the whole cluster from the Ti atom to which the dye bound in less 100 fs, the time resolution of our equipment; simultaneously the hot hole in catechol radical cation will hop to other dye molecules. The motion information of charge carriers in cluster is recorded in the depolarization measurement; the depolarization rate of catechol⁺ absorption presents $\tau \approx 2.17$ ps. The quantum mechanics calculation on the hole hopping to other catechols are remarkably consistent with experimental results.



Scheme 4-1. Possible sequential events on Ti17cat4 after excitation

The depolarization induced by electron delocalization was not observed at the long wavelengths because the delocalization process is finished in < 100 fs which is beyond the time resolution of our equipment.

For the migration of electrons, holes or excitons between clusters, the concentration of the cluster plays a big role in it because the distance of cluster is related to the cluster concentration, and the electrons or holes transfer is through space. The efficient electron

transfer through space requires the distance is < 2 nm. Under low concentration the clusters are more separated than in high concentration. Even under high concentration and the clusters are aggregated, due to the organic shell of the cluster the transfer distance for electron or hole is approximately 2-5 nm. Hence the chance for the intercluster electron or hole transfer is very small.

4.2 Results and discussions

4.2.1 Raman spectrum of Ti17cat4

The spectrum of Ti17 contains a characteristic progression of peaks at 644, 616 and 575 cm^{-1} (in bulk brookite 635, 585 and 535 cm^{-1})[8, 9]. In Ti17cat4 the overall appearance of the Raman peaks associated with the inorganic core of the cluster is very similar; however, the origin of the sequence is shifted from 644 to 650 cm^{-1} . Importantly, in contrast with the parent Ti17 cluster, all Ti ions on the surface of Ti17cat4 are coordinatively saturated.

The substitution of four isopropoxide ligands with catechol molecules at penta-coordinated Ti atoms is also reflected in the Raman spectrum. The huge decrease of scattering signal at 1180 and 1030 cm^{-1} [10] that corresponding to the C-O stretching and C-H wagging modes of isopropoxide ligands is related to the coordination change from penta to hexa at four corner Ti atoms. Under penta-coordination there is more electron density shift from the isopropoxide toward Ti which gives rise to stronger Raman scattering, and the detail is thoroughly discussed in the paper on Ti17. Second big change arises from the region of 1200 to 1600 cm^{-1} due to the formation of catechol-Ti complex. The sequence of peaks in this region is the result of strong vibration coupling among Ti-

O with C-O and C-C vibration of benzene ring [4], especially the vibration mode at 1331 cm^{-1} can be considered as the indicator that hydroxyl group of catechol in chelate geometry[11]. The Raman spectra of both clusters reveal that the spectrum change is intimately linked with the four corner Ti atoms.

4.2.2 UV-Vis spectrum

Figure 4-3 shows the UV-vis absorption spectra of catechol, Ti17 and Ti17cat4 in acetonitrile. The spectrum of Ti17cat4 displays a typical charge transfer (CT) absorption band with a peak at 345 nm and a discernible shoulder at approximately 400 nm, which extends well into the visible range, rendering the solid compound bright red. In contrast, the parent Ti17 cluster which contains solely isopropoxide ligands is colorless with the onset of absorption corresponding to the quasi-conduction band of the inorganic metal oxide core starting around 300 nm. The shape and position of CT band of Ti17cat4 are nearly identical with the spectra reported for cat@TiO₂, which also exhibit a CT band ~ 340 nm with a similar shoulder at 420-430 nm[2, 12, 13].

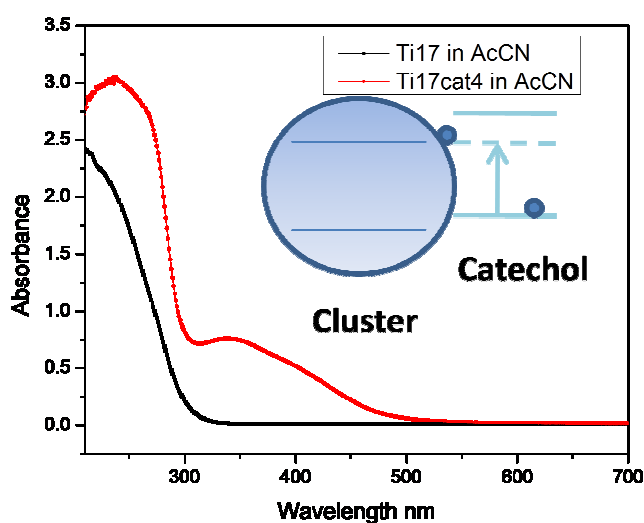


Figure 4-3. UV-Vis spectrum of Ti17cat4, Ti17 and catechol in acetonitrile

4.2.3 The ligand-core electronic coupling

The analogue LMCT band in the molecular complex $[\text{Ti}(\text{cat})_3]^{2-}$ has a maximum at 389 nm with $\epsilon_{\text{max}} = 9300 \text{ M}^{-1}\text{cm}^{-1}$. The extinction coefficient of the CT band of $\text{Ti}_{17}\text{cat}_4$ is approximately $1900 \text{ M}^{-1}\text{cm}^{-1}$ and its width 10300 cm^{-1} . The magnitude of the electronic coupling $|V_{GE}|$ between the HOMO orbital of catechol and the inorganic core of the cluster can be calculated based on the upper spectral parameters. By applying the approximate equation:[14]

$$|V_{GE}| \approx 0.0206 \cdot (\epsilon_{\text{max}} \cdot \nu_{\text{max}} \cdot \Delta\nu_{1/2})^{1/2} / r_{GE} \quad (1)$$

Which is derived from the Mulliken-Hush theory by assuming a symmetric Gaussian shape of the CT band, where $\Delta\nu_{1/2}$ is the width of the band, ν_{max} is the position of the maximum and r_{GE} is the effective displacement of the electron, one obtains $|V_{GE}| = 5160 \text{ cm}^{-1}$. Alternatively, one can view total CT absorption cross section of $\text{Ti}_{17}\text{cat}_4$ as a sum of separate CT transition between each of the four catechol moieties and the core of the cluster. In this case, the extinction coefficient of the CT band can be partitioned into four equal components of $475 \text{ M}^{-1}\text{cm}^{-1}$ for each ligand. This approach, which seems more appropriate, yields $|V_{GE}| = 2580 \text{ cm}^{-1}$ for each catechol moiety. Importantly, even this lower value remains well within the strong coupling regime, with $|V_{GE}|$ exceeding both $k_B T$, as well as the frequency of the skeletal vibrations of the ligand and the phonon modes of the core of the cluster, which are responsible for the bulk of the nuclear reorganization energy in this system.

In above calculation of the $|V_{GE}|$ we used $r_{GE}=3 \text{ \AA}$, as determined by Nawrocka *et al.* in Stark spectroscopy experiments on cat@TiO₂[15], he has demonstrated that the lowest energy CT transition in cat@TiO₂ is accompanied by a dipole moment change $|\Delta\mu|_{CT} = 15.7 \text{ D}$. The instantaneous charge separation distance of 3 \AA deduced from the $|\Delta\mu|_{CT}$ implies that the injected electron is initially localized on the Ti ion to which the catechol ligand is bound and subsequently delocalizes over the underlying bulk TiO₂. As we will see, the picture of a tightly bound initial polaronic exciton which undergoes rapid evolution into the fully stabilized charge-separated state applies also to Ti17cat4. Furthermore, the Stark effect measurements reveal that the CT transition in catechol@TiO₂ is accompanied by a reduction of polarizability, pointing to tight localization of charges in the incipient charge transfer state. This is consistent with a promotion of an electron from a delocalized π -orbital of catechol to a more compact d -orbital of an individual Ti atom. These experimental results agree very well with the quantum mechanical modeling of electron injection into bulk TiO₂ performed by several groups[13, 16-18].

4.2.4 Transient absorption spectrum of Ti17cat4

Table 4-1. Constant of acetonitrile and propylene carbonate

	μ	ϵ	η (cP)
Propylene Carbonate	4.9 D	66.14 ²⁰	2.5
Acetonitrile	3.92 D	33.64 ²⁰	0.37

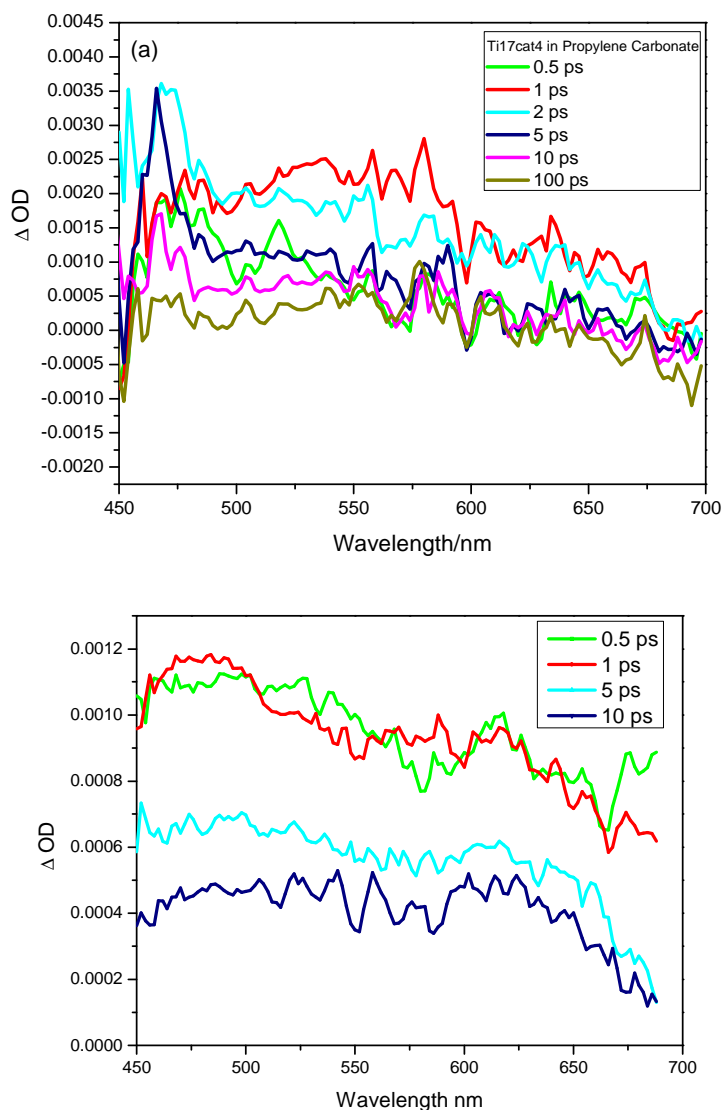


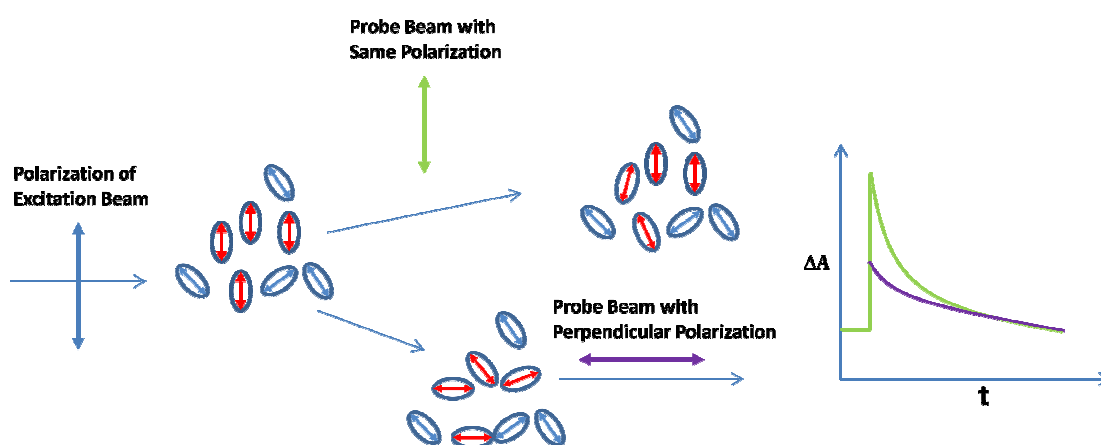
Figure 4-4. Transient absorption spectrum of Ti17cat4 in propylene carbonate and acetonitrile

In the pump-probe experiments, 370 nm excitation wavelength leads to the appearance a broad and rather featureless transient absorption spectrum as shown in Figure 4-4. The transient absorption spectra in propylene carbonate and acetonitrile display a similar transient absorption shape. In the polar acetonitrile, $\epsilon=36.6$, there are two discernible bands identified at $\sim 450\text{-}530$ and $\sim 600\text{-}650$ nm in the transient absorption spectrum. The long wavelength band originates from the electron injected into the metal

oxide core Ti17cat4, as determined in the Ti17⁺[6]. The short wavelength band is dominated by the absorbance of the catechol radical cation[4]. The absorption signal from both carriers is overlapped in region from 530-600 nm. A similar transient absorption feature shows in propylene carbonate, but the absorption band at short wavelength is narrower. The similarity can be explained by the high dielectric constant of the two solvents which favors the charge separated state; the difference originates from varying solvent viscosity and molecular structure. The high viscosity and the size of propylene carbonate molecule retard the efficient reorientation around the cluster, so we chose acetonitrile to do most measurements. The TA measurements were recorded with the polarization of the pump and probe beams set at the magic angle, the charge separated state formed in TA appears to be complete within the ~100 fs temporal resolution of our experiments. Under these polarization setting the decay of the transient absorption of charge separated state is homogeneous, with only a hint of a blue shift of the absorption at early times (1 ps), which would be consistent with the IVR (intramolecular vibrational redistribution) and solvent reorganization. Solvent reorganization may play a role in the stabilization of the hole (oxidized catechol moiety), however, it should be of little or no importance for the injected electron which is delocalized over the TiO₂ core and screened off the solvent influence by the shell of the isopropoxide ligands. The transient dynamics measured with parallel and perpendicular pump and probe polarization reveals a rich excited state dynamics of Ti17cat4 which was obscured by the broad, overlapping spectra of the conduction band electron and the oxidized catechol.

4.2.5 Dynamic depolarization measurements on Ti17cat4 in acetonitrile

Aside from the diffusion of the whole cluster, which is slow and occurs on $\tau > 200$ ps time scale, the e^- signal can depolarize due to the electron delocalization, and the cat^+ signal can also depolarize due to hole hopping. In the anisotropy measurement, a polarized pump beam excites the sample; the transition dipole moment of the molecular cluster oriented in the same polarization direction will be excited preferentially. If the polarization of probe is polarized parallel to the pump beam it will firstly probe the excited species whose transition moment oriented in the same polarization and the measurement will be perturbed by the reorientation process. If the probe beam is polarized perpendicularly to the pump beam, the measurement only affected by the molecule whose transition dipole moment reorient to the same polarization as the probe[19].



Scheme 4-2. Dynamic depolarization measurement

The long wavelength, $\lambda > 550$ nm portion of the transient spectrum, which corresponds to the absorption of the e^- in quasi-semiconduction band of the inorganic core of the cluster, shows no discernible dependence on the polarization of the probe pulse. In this wavelength range, transients collected with parallel and perpendicular probe polarization were superimposable, showing that the depolarization of the absorption and

the delocalization of the injected electron are much faster than the ~ 100 fs resolution of our experiments. This outcome is consistent with the picture of a band-like electronic structure of the TiO_2 core of the cluster, which was proposed in the Ti17 chapter[6].

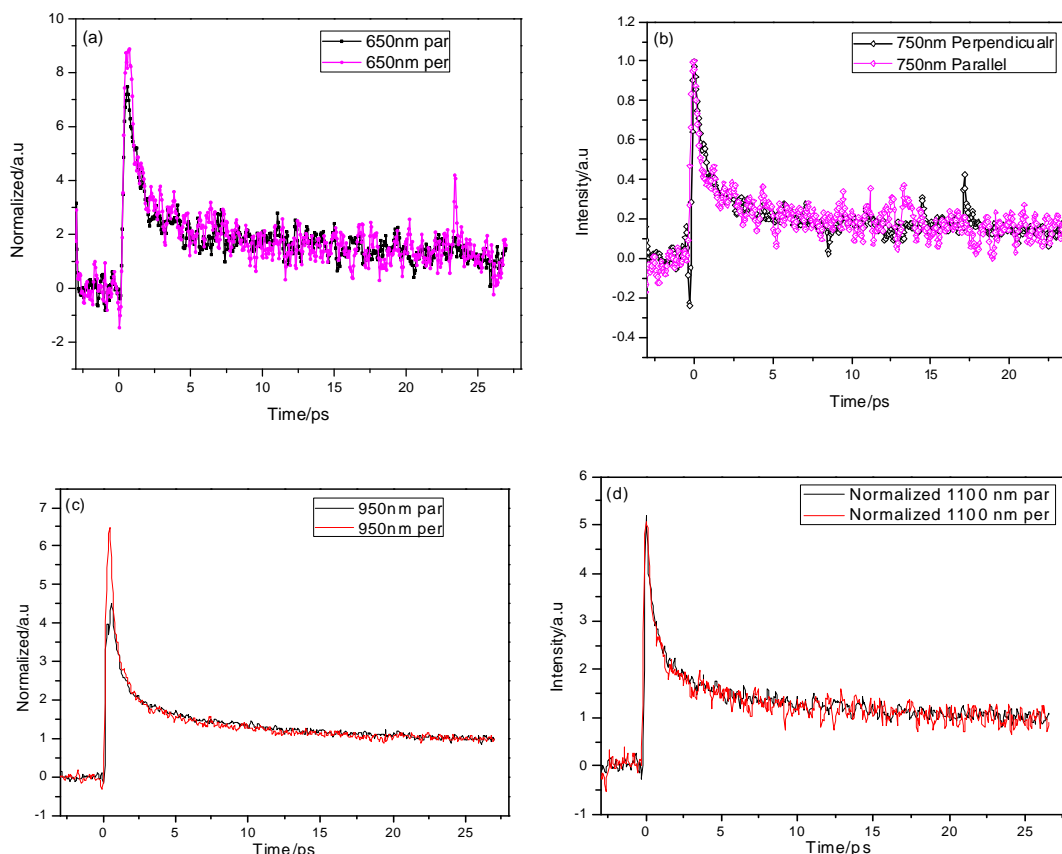


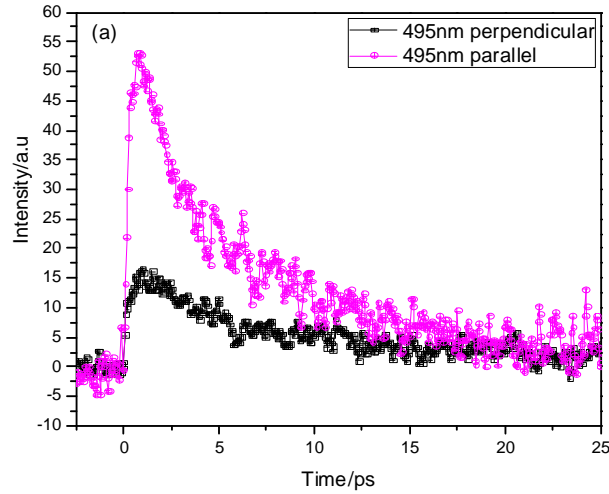
Figure 4-5. Transient dynamics measured at long wavelengths

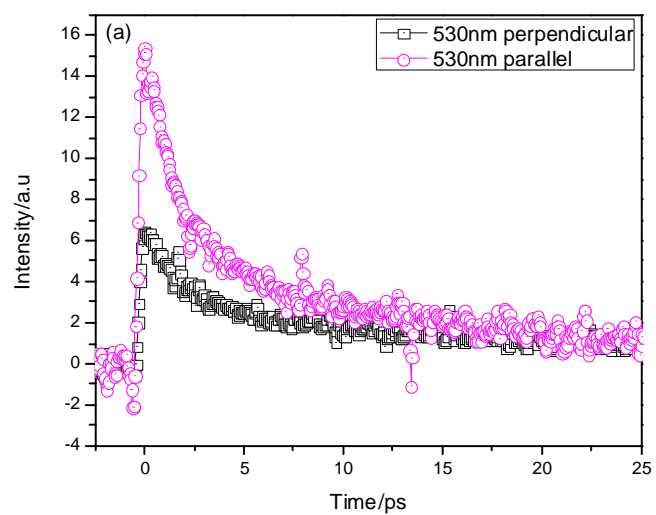
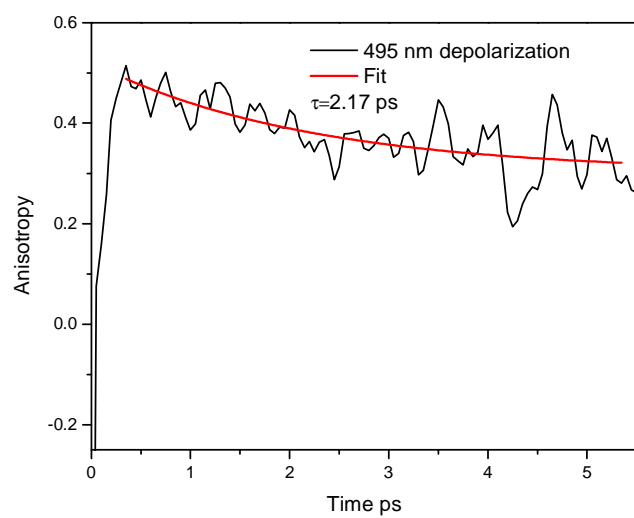
The behavior of the short wavelength, $\lambda < 550$ nm region of spectrum, is dominated by the absorption of the oxidized catechol ligand, cat^+ . As shown in Figure 4-6 (a) both the initial magnitude and decay profiles respond strongly to the polarization of the probe pulse. At $t=0$ the absorption at parallel probe polarization is 2-3 times higher than for crossed polarization indicating that on the time scale of 100 fs, the hole remains localized on the catechol ligand from which the electron was injected. The corresponding values of $R(0)$ are 0.47 at 495 nm and 0.25 at 530 nm, respectively, with the lower value at the

longer wavelength reflecting a larger contribution from instantaneously depolarized absorption of the injected electron. The trace recorded at parallel polarization show fast decay and depolarization appears to be complete approximately 20 ps after excitation. Since rotational diffusion of a body as large as the Ti17cat4 cluster is much slower than that and occurs with > 200 ps, it is safe to say that observed dynamics corresponds to the hole hopping among the four catechols, with each hop between two adjacent sites changing the orientation of the cat $^{+}$ transition dipole moment by $\pm 90^\circ$. Because the noise present in $A(t)$ and $A(t)$ the depolarization trace becomes exacerbated when polarization parameter is calculated, the analysis of $R(t)$ profile was limited to as single exponential fit of the first 5 ps of the decay. The depolarization calculation is based the below equation[19].

Dynamic Depolarization Ratio:

$$R(t) = [OD_{\parallel}(t) - OD_{\perp}(t)] / [OD_{\parallel}(t) + 2OD_{\perp}(t)] \quad (2)$$





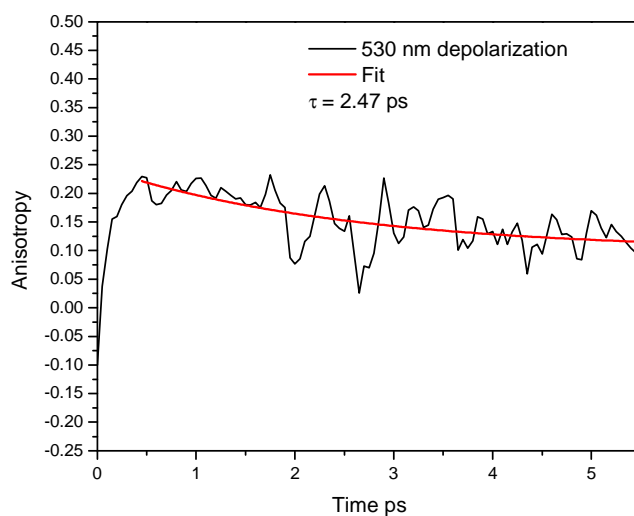


Figure 4-6. Depolarization measurements at short wavelengths in acetonitrile

Table 4-2. Time constants of transient dynamics at 495 and 530 nm

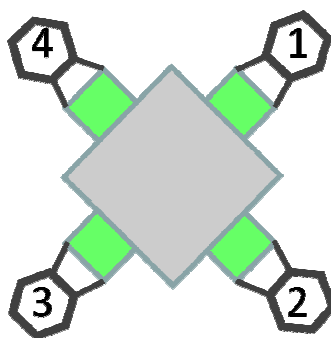
Probe wavelength and polarization	τ_1 (ps)	A_1	τ_2 (ps)	A_2
495 nm \parallel	1.42	0.40	9.03	0.60
495 nm \perp	2.17	0.41	14.4	0.59
530 nm \parallel	2.0	0.64	17.3	0.36
530 nm \perp	3.1	0.64	29.5	0.36

Based on the discussion we can conclude that the depolarization rate induced by the hole hopping is around 2.17 ps, while the depolarization of the electron is so fast that beyond the experiment resolution.

4.2.6 Quantum mechanics calculation of hole hopping dynamics

The quantum mechanics modeling on hole hopping among equivalent ligand sites of Ti17cat4 complements the depolarization measurement. QM simulation was conducted by Victor Batista and Robert Snoeberger from Yale University. The theoretical

calculation and experimental measurements were carried independently. Yale and our group were not aware of one another's results prior to the completion of the calculations and measurements. The initial electronic wave packet representing a hole formed by photo-oxidation of a catechol adsorbate was evolved in time by integrating the time-dependent Schrödinger equation. The geometry of the cluster was obtained by refining the X-ray diffraction crystal structure.[1] The final energy mismatch between the catechol sites in the optimized structure is within the range of ~ 5 meV. If the highest energy site 1 is set as a reference, the relative energies of a hole localized on the remaining catechol sites are -1.8, -5.4 and -2.5 meV for sites 2, 3 and 4, respectively. The energy variation arises due to slight differences in the relaxed geometry of each catechol and its environment at the convergence cut-off of our calculations. This slight disorder most likely gives a realistic image of the surface of Ti17cat4 under ambient conditions. In this simulation, this energy distribution can be taken as a random, instantaneous snapshot of the fluctuating energy landscape of the cluster. Indeed, molecular dynamics modeling by other groups has



Scheme 4-2 Catechol modified cluster

shown that electronic energy levels of adsorbates on the surface of TiO_2 fluctuate by a few tenths of an eV due to thermal motion (at room temperature $k_bT \approx 25$ meV)[17, 18].

The results indicate the oscillating population of each of the four catechol sites during the simulation as shown in Figure 6. The hole was initially fully localized on the highest energy catechol ligand 1. The population in site 1 transfers to the adjacent catechol 2, 3 and 4 on short picoseconds time scale. The unequal population in transferring between each of the catechol adsorbates reflects the differences in the electronic coupling and in the energy mismatch for each pair of catechols. The calculated electronic coupling $|V|$ between catechol 1 and catechol 2 is ~ 2.4 cm $^{-1}$ whereas the coupling between catechol 2 and catechol 3 is ~ 2.9 cm $^{-1}$. Even though the electronic coupling between 2 and 3 is stronger, very little population, $<1\%$, is transferred to 3 during the simulation. This is due to the larger energy mismatch between 2 and 3 compared to 1 and 2. The population of catechol 4 which is adjacent to catechol 1 also remains rather low due to the large energy mismatch between these sites, even though they experience the largest electronic coupling as illustrated by the highest frequency of oscillation, $\tau_{\parallel} = 2.5$ ps. The population at each site oscillates with a regular frequency due to the sustained coherence in the simulation which does not include nuclear relaxation. The simulation shows that the rate for the coherent hole hop between two adjacent catechols taken to be $\frac{1}{2}$ of the oscillation period ranges from ~ 1.2 ps (catechols 1 and 4) to ~ 2.1 ps (catechols 1 and 2), i.e. in remarkably good agreement with the depolarization measurement. Given the simplicity of the model which does not include nuclear relaxation or coupling to a bath, this outcome is very satisfactory.

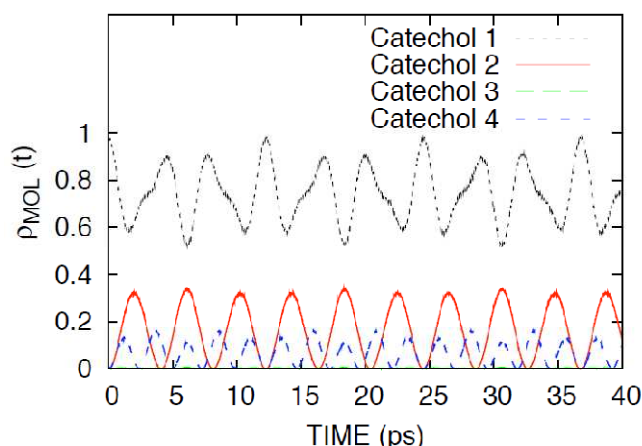


Figure 4-7. Time-dependent occupation of the photogenerated hole on each of the four catechol adsorbates during the first 40 ps of dynamics. The hole was initially localized on catechol 1.

Naturally, the sustained undamped population oscillations shown in Figure 4-7 are the result of the fully coherent model which does not include coupling to the bath and does not allow for nuclear relaxation. In a real system the dephasing and relaxation are rapid and the corresponding oscillations of the polarized spectra are not observed. Nevertheless, it is worthwhile to note that the four-fold symmetry of Ti17cat4 influences the dephasing behavior. Since the transition dipole of the neighboring catechol ligands are mutually orthogonal, each clockwise or counterclockwise hole hop between adjacent sites causes a 90° switch of polarization. Each subsequent hop, whether forward or back, fully restores the original polarization. As a result, the loss of polarization information occurs purely because of dephasing of the rate of the hopping events, unlike in a system with randomly oriented transition dipoles, e.g. in a multichromophore polymer, in which case each hop leads to a random change of polarization.

The modeling performed here corresponds to the low temperature, fully coherent limit. Under these conditions, the system has a rigid nuclear configuration and the hole

propagation dynamics is determined by the electronic couplings between the nearly resonant donor and acceptor sites. Within the semi-classical Marcus theory description[20], this simple model corresponds to the limit where the reorganization energy λ is negligible. Therefore, the system dependent parameters governing the hole transfer rate are the electronic coupling and the driving force

$$k_{ET} = \frac{2\pi}{\hbar} |V|^2 \delta(\Delta G^\ddagger) \quad (3)$$

Where in our approximation $\delta(\Delta G) = 1$ when the driving force $\Delta G = 0$ (a delta function is the limit of a Gaussian with width approaching zero) and the rate is determined by the strength of the electronic couplings $|V|$ between near resonant states of equivalent symmetry.

The rate of thermalized hole hopping in Ti17cat4 can be estimated using the above predictions of the fully coherent, frozen geometry model by substituting a reasonable value of free energy of activation, ΔG^\ddagger , into equation 3. The main component of the activation barrier for the hole hopping in Ti17cat4 is the internal reorganization of the catechol ligand. DFT calculations at B3LYP level yield the $\text{cat} \leftrightarrow \text{cat}^+$ reorganization energy of 1300 cm^{-1} and, correspondingly, $\Delta G^\ddagger = \lambda/4 = 325 \text{ cm}^{-1}$. By taking this value and ignoring all other contributions to the overall reorganization energy, the upper limit for the rate of thermally assisted hole hopping in Ti17cat4 is obtained. At $T = 293 \text{ K}$ the exponential factor $e^{-\Delta G^\ddagger/kT}$ is ~ 0.2 and the corresponding thermal hopping rates are 6-10 ps. Additional components of λ is close to the frequency of the in-plane skeletal modes of the aromatic ring of catechol. This suggests that the initial hot hole hopping in Ti17cat4 is directly linked to the population of these vibrational modes upon electron injection. Once these high frequency modes undergo IVR, only thermally assisted hopping is possible.

Comparing to the hole hopping constant $\tau=2$ ps in Ti17cat4, the hole hopping among the isopropoxide ligands at Ti17 cluster surface will be much faster. Based on the Marcus-Hush equation, the determining factors of electron transfer rate are the electronic coupling of two adjacent ligands, the reorganization energy and the distance of two ligands. For catechol modified Ti17 cluster, it has S_4 symmetry and the cluster diameter is 2 nm. The calculated distance of two catechol is ~ 14.14 Å, while the distance between two isopropoxide ligands is ~ 3 Å. Due to the big difference on the ligands distance, the reorganization energy in Ti17 cluster will be much smaller than in Ti17cat4. For electronic coupling in two different clusters we need to do the calculation. It is difficult to estimate the electronic coupling. If we fix the electronic coupling for these two clusters, the hole hopping rate in Ti17 is much faster than in Ti17cat4 due to the reorganization energy.

4.2.7 The discussion on dynamics of electron transfer, relaxation and recombination

The decay of the charge-separated state of Ti17cat4 is dominated by two regimes. The fast component is assigned to the geminate recombination of the initially formed strongly correlated electron-hole pairs, in which the hole resides at the catechol unit from which the electron was injected. This rapid process accounts for up to 60% of the overall recombination and competes with the hot hole hopping and the IVR. Because of the small size of the core of cluster (~ 1 nm diameter), the electron-hole pair remains more strongly correlated throughout the lifetime of the charge separated state than it is the case for dye-sensitized colloidal metal oxides. Geminate recombination in the latter class of systems is usually minor because of the facile escape of the electrons into the bulk of the particle

and resulting screening of the Coulomb interaction. The remaining charge recombination in the Ti17cat4 cluster is nonexponential with the retrieved time constants showing dependence on the length of the acquisition window. For practical reasons we followed it only to approximately 300 ps. The nonexponential behavior is typical of the dye-sensitized colloidal TiO₂ systems, in which the geminate component is followed by the recombination of the bulk, freely diffusing conduction band electrons and finally by the highly inhomogeneous disappearance of the electrons trapped by defects. The rate of the last process depends on the distribution of the trap depths and often spans a broad range from nanoseconds to milliseconds. Besides from the initial geminate and the subsequent quasi-bulk recombination, it is more difficult to explain the origin of multiexponential decay in the case of the monodisperse Ti17cat4 cluster. The cluster is small enough for the injected electron to rapidly sample its entire volume. A fraction of the long-lived electron-hole pairs which escaped the initial geminate recombination is almost certain to undergo intersystem crossing (ISC) to the triplet state. Such triplet electron-hole pairs may recombine at a slower rate because of the spin selection rules, as long as the spin-orbit coupling is smaller than the singlet-triplet splitting which is determined by the electron-hole exchange interaction.

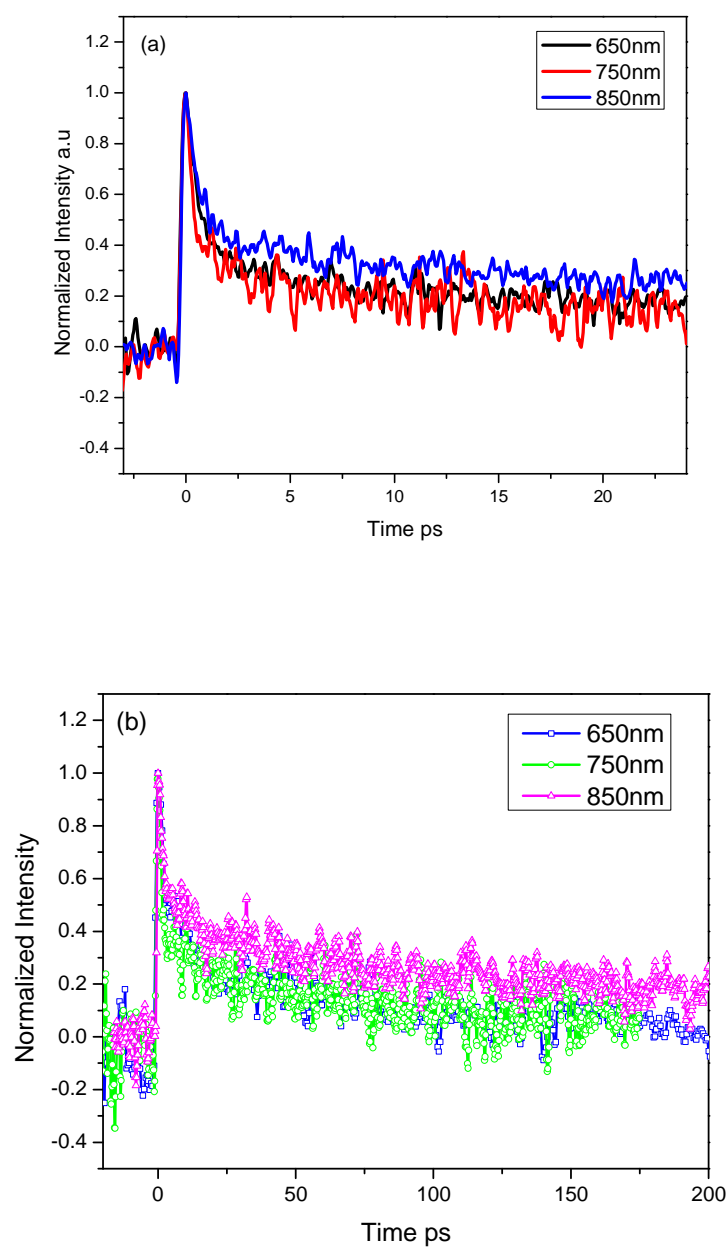


Figure 4-8. Ti17cat4 in acetonitrile : (a) transient dynamics in 25 ps time window, (b) dynamics in 200 ps time window

After fitting a long life component always returns in the long scan transient which does not decay at 300 ps timescale. The longest lived absorption component originates

either from the charge separated species or from the triplet state we have discussed in Chapter 3.

Table 4-3. Multiexponential kinetic parameters for the charge relaxation & recombination measured at different wavelengths and at parallel vs. perpendicular pump-probe polarization.

λ_{probe} (nm)	A_1	τ_1 (ps)	A_2	τ_2 (ps)
650 //	0.65 ± 0.02	0.78 ± 0.04	0.30 ± 0.01	36.8 ± 1.9
650 \perp	0.62 ± 0.02	0.83 ± 0.05	0.25 ± 0.01	44.7 ± 3.6
750 //	0.68 ± 0.04	0.49 ± 0.04	0.30 ± 0.01	29.2 ± 2.0
750 \perp	0.71 ± 0.02	0.84 ± 0.04	0.24 ± 0.01	44.0 ± 3.1
850 //	0.55 ± 0.03	0.83 ± 0.07	0.40 ± 0.01	45.5 ± 3.4
850 \perp	0.64 ± 0.02	0.89 ± 0.05	0.26 ± 0.01	42.5 ± 3.6

Table 4-4. Multiexponential kinetic parameters for the charge relaxation & recombination at a longer time scale.

λ_{probe} (nm)	A_1	τ_1 (ps)	A_2	τ_2 (ps)	A_3	τ_3 (ps)
650 //	0.30 ± 0.13	1.28 ± 0.73	0.40 ± 0.13	7.0 ± 2.1	0.30 ± 0.02	92.9 ± 5.6
650 \perp	0.64 ± 0.10	1.06 ± 0.25	0.25 ± 0.04	15.6 ± 4.2	0.19 ± 0.02	240.4 ± 33.8
750 //	0.53 ± 0.08	0.77 ± 0.22	0.27 ± 0.03	24.0 ± 5.3	0.2 ± 0.03	330.6 ± 87.5
750 \perp	0.37 ± 0.11	1.10 ± 0.44	0.35 ± 0.10	80.2 ± 1.69	0.34 ± 0.01	221.4 ± 9.8
850 //	0.50 ± 0.08	1.71 ± 0.19	0.20 ± 0.02	30.3 ± 4.9	0.30 ± 0.02	385.1 ± 44.9
850 \perp	0.52 ± 0.04	0.81 ± 0.11	0.19 ± 0.02	15.9 ± 2.4	0.30 ± 0.01	293.8 ± 14.3

4.3 Conclusions

Nanometer size molecular polyoxotitanate cluster such as Ti17 and Ti17cat4 offer a unique, well characterized bridge between the realm of small molecule electron donor-acceptor systems and dye-sensitized TiO₂ nanoparticles, which for nearly three decades have been at the center of research on hybrid solar energy conversion materials and interfacial electron transfer.

Ti17cat4 and related molecular polyoxotitanate clusters are excellent models of charge injection and recombination in highly heterogeneous dye-sensitized nanoparticles and mesoporous films of wide band gap semiconductors. Because of the nanometer size of the TiO₂ core and the presence of a quasi band structure, Ti17cat4 is a much closer analogue of the catechol@TiO₂ system than the mononuclear [Ti(cat)₃]²⁻ complex. The study of its photoinduced electron transfer behavior revealed a rich, highly dynamic system, in which hole hopping among degenerate ligand sites, IVR and geminate charge recombination occur simultaneously and compete with each other. The instantaneous electron injection and the lack of clear temporal separation between the subsequent relaxation processes provide a unique testing ground for experiment and modeling alike. Our experiments and simulations show that the initial hot hole hopping is very rapid and occurs with the rate of 1-2 ps. In this time window the system is not fully thermally equilibrated and it is unlikely to follow the classical Marcus theory characterized by a single value of activation energy and a single time and conformation averaged electronic coupling. Once the high frequency skeletal modes of catechol are depopulated and solvent relaxation is complete, both the hole hopping and charge recombination slow down significantly. The respective thermalized rates are approximately 15-20 ps for the former and 25 ps for the latter.

References

1. Benedict, J.B. and P. Coppens, *The Crystalline Nanocluster Phase as a Medium for Structural and Spectroscopic Studies of Light Absorption of Photosensitizer Dyes on Semiconductor Surfaces*. Journal of the American Chemical Society, 2010. **132**(9): p. 2938-2944.
2. Wang, Y., et al., *Comparison of electron transfer dynamics in molecule-to-nanoparticle and intramolecular charge transfer complexes*. The Journal of Physical Chemistry B, 2003. **107**(35): p. 9434-9440.
3. Jakubikova, E., et al., *Interfacial Electron Transfer in TiO₂ Surfaces Sensitized with Ru (II)– Polypyridine Complexes†*. The Journal of Physical Chemistry A, 2009. **113**(45): p. 12532-12540.
4. Lana-Villarreal, T., et al., *A spectroscopic and electrochemical approach to the study of the interactions and photoinduced electron transfer between catechol and anatase nanoparticles in aqueous solution*. Journal of the American Chemical Society, 2005. **127**(36): p. 12601-12611.
5. Coppens, P., Y. Chen, and E. Trzop, *Crystallography and Properties of Polyoxotitanate Nanoclusters*. Chemical Reviews, 2014. **114**(19): p. 9645-9661.
6. Bao, J., et al., *Excitons and Excess Electrons in Nanometer Size Molecular Polyoxotitanate Clusters: Electronic Spectra, Exciton Dynamics, and Surface States*. The Journal of Physical Chemistry B, 2012. **117**(16): p. 4422-4430.
7. Zhai, H.J., et al., *δ Aromaticity in [Ta₃O₃]*. Angewandte Chemie, 2007. **119**(23): p. 4355-4358.
8. Mattsson, A. and L. Osterlund, *Adsorption and photoinduced decomposition of acetone and acetic acid on anatase, brookite, and rutile TiO₂ nanoparticles*. The Journal of Physical Chemistry C, 2010. **114**(33): p. 14121-14132.
9. Lottici, P., et al., *Raman scattering characterization of gel-derived titania glass*. Journal of materials science, 1993. **28**(1): p. 177-183.
10. Moran, P.D., et al., *Vibrational spectra and molecular association of titanium tetraisopropoxide*. Inorganic Chemistry, 1998. **37**(11): p. 2741-2748.
11. Shoute, L.C. and G.R. Loppnow, *Excited-state dynamics of alizarin-sensitized TiO₂ nanoparticles from resonance Raman spectroscopy*. The Journal of Chemical Physics, 2002. **117**(2): p. 842-850.

12. Varaganti, S., et al. *Interfacial charge transfer dynamics in small molecule-modified TiO₂ nanoparticles*. in *SPIE NanoScience+ Engineering*. 2010: International Society for Optics and Photonics.
13. Hilgendorff, M. and V. Sundström, *Dynamics of electron injection and recombination of dye-sensitized TiO₂ particles*. The Journal of Physical Chemistry B, 1998. **102**(51): p. 10505-10514.
14. Balzani, V., et al., *Electron transfer in chemistry*. Vol. 1. 2001: Wiley-VCH Weinheim, Germany.
15. Nawrocka, A., A. Zdyb, and S. Krawczyk, *Stark spectroscopy of charge-transfer transitions in catechol-sensitized TiO₂ nanoparticles*. Chemical Physics Letters, 2009. **475**(4): p. 272-276.
16. Rego, L.G. and V.S. Batista, *Quantum dynamics simulations of interfacial electron transfer in sensitized TiO₂ semiconductors*. Journal of the American Chemical Society, 2003. **125**(26): p. 7989-7997.
17. Abuabara, S.G., L.G. Rego, and V.S. Batista, *Influence of thermal fluctuations on interfacial electron transfer in functionalized TiO₂ semiconductors*, in *Journal of the American Chemical Society*. 2005. p. 18234-18242.
18. Duncan, W.R. and O.V. Prezhdo, *Theoretical studies of photoinduced electron transfer in dye-sensitized TiO₂*. Annu. Rev. Phys. Chem., 2007. **58**: p. 143-184.
19. Rulliere, C., *Femtosecond laser pulses*. 2005: Springer.
20. Sutin, N., *Theory of electron transfer reactions: insights and hindsight*. Prog. Inorg. Chem, 1983. **30**: p. 441-498.

Chapter 5. Exciton Dynamics in Molecular Ti6 Cluster

5.1 Introduction

The smallest cluster investigated in this project is $\text{Ti}_6(\text{OOCCH}_3)_6(\text{OPr}^i)_6$ [Ti_6], MW=1091.16, possessing a similar core-shell structure as Ti_{17} . The compact core contains 6 Ti atoms and 6 O atoms. Two kinds of organic ligands are bound to the Ti atoms, i.e. isopropoxides and acetates which form the organic shell. Each Ti atom adopts 6-fold coordination as shown in the Figure 5-1(side view of the cluster). The acetate ligands are located in the equatorial plane of the cluster and each of them serves as a bridge connecting two neighboring Ti atoms with a carboxylic group. The isopropoxide ligands bind with Ti atoms axially from the top and bottom. The blue atom in the Figure 5-1 highlights the coordination of single Ti atom.

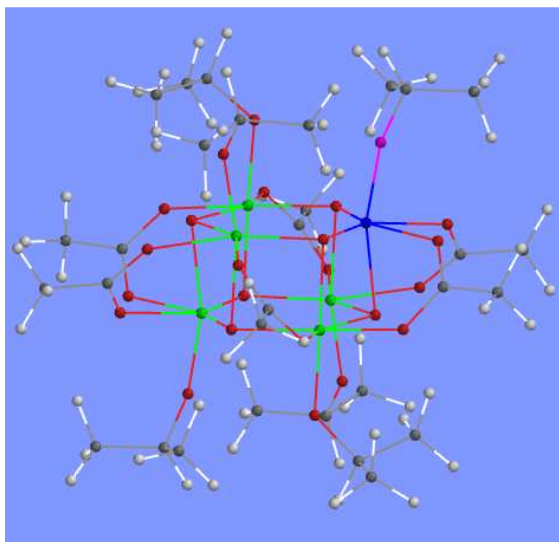


Figure 5-7. Structure of Ti_6 cluster

Because Ti6 has much fewer atoms than Ti17 cluster, Ti6 cluster may possess more molecular-like properties. The surface ligands play a critical role in localizing and stabilizing the excited exciton based on the vibronic structure of fluorescence spectrum. In addition the broad fluorescence spectrum with well defined vibrational peaks establishes the key role of ligands on the optical properties of cluster. Ti6 offers a good opportunity to study the effect of surface modification on the optical properties and dynamics of charge recombination. It also provides an excellent model to carry out quantum chemical calculations. The combination of theoretical methods and the experimental measurements enable us to have an overall understanding of the Ti/O cluster.

First, we have examined the basic ground state optical properties. The Raman spectrum confirms the presence of two kinds of organic ligands on the cluster surface. The combination of UV-Vis spectroscopy and quantum calculations helps to determine that the absorption transition occurs at the interface of Ti6 cluster.

Two well defined absorption bands in the transient absorption spectra of Ti6 are ascribed to different *d-d* transitions. The transient dynamics is homogenous at all wavelengths and indicates a relatively tightly-bound electron-hole pair stabilized by the organic ligands.

5.2 Results and discussion

5.2.1 UV-Vis spectrum

Since the Ti6 core only contains 12 atoms which cannot form the real conduction band as in the TiO₂ nanoparticles, it may have different ground state absorption compared

to Ti17 cluster. The steady state absorption shows Ti6 has band edge absorption at ~340 nm in dibutyle ether, but the onset is lightly blue-shifted in comparison with Ti17. The blue shift is ascribed to the molecular property of Ti6. The similar steady state absorption implies the transition probably occurs at the interface of cluster. In order to determine the transition in Ti6 cluster, the quantum chemical calculation is introduced, and the results indicate the electron in the isopropoxide ligand is excited to the Ti atom to which the ligand bound.

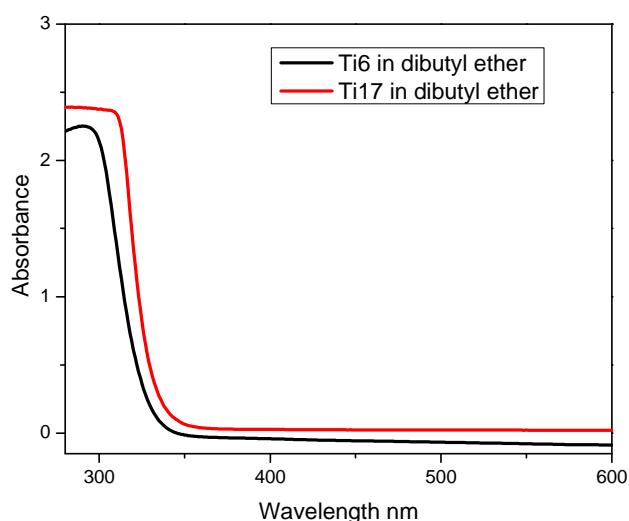
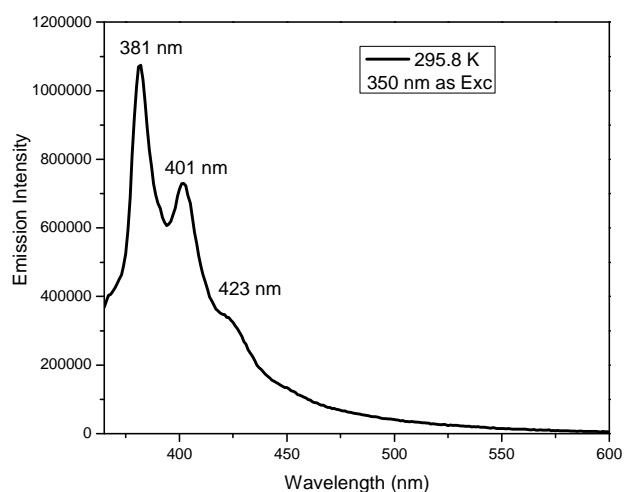


Figure 5-8. UV-Vis spectra of Ti6 (black) and Ti17 (red) in acetonitrile at room temperature

5.2.2 Emission spectrum

The fluorescence spectrum was recorded at room temperature following excitation at 350 nm. It exhibits a molecular character with three clear emission peaks at 381 nm, 401 nm, and 423 nm, respectively; and two more discernible emission peaks at longer wavelength which indicate the emissive exciton couples with certain vibrational modes of

the ligand at the interface. The surface ligands help localize and stabilize the exciton formed at the interface. A deeper analysis on the vibration mode was carried out through determining the separation of vibronic peaks. The frequency difference corresponds to vibrational frequency of a certain mode. The calculated $1305 \pm 50 \text{ cm}^{-1}$ difference from the first two strongest emission peaks presents the most reliable value since the emission peaks turn broad at long wavelengths. This vibrational frequency value obtained from Ti6 is very close to the one we acquired from Ti17 cluster i.e. $1290 \pm 150 \text{ cm}^{-1}$. The close results imply the isopropyl ligand on the cluster surface has a significant influence on dynamics of exciton of both clusters.



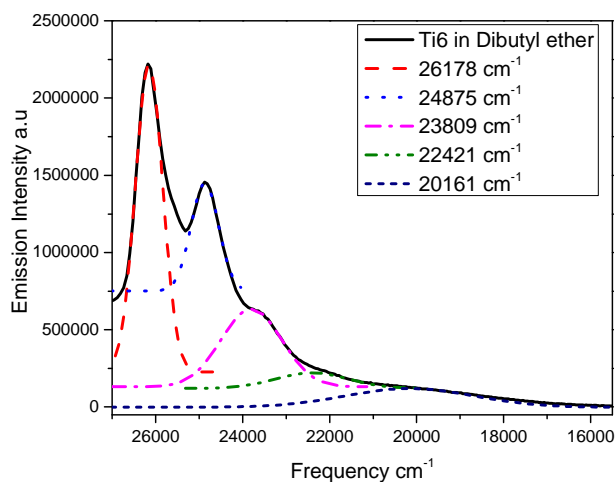


Figure 5-9. Fluorescence spectrum of Ti6 in acetonitrile at room temperature

Table 5-1. Frequency of emission peaks and frequency difference

Vibration peak (cm^{-1})	26178	24875	23809	22421	20161
Frequency Difference (cm^{-1})		1305	1066	1388	2260

The fluorescence spectra of Ti6 measured from 279 K down to 220 K show the emission intensity increases with the decrease of temperature. This can be explained by the reduced perturbation from the thermal motion at low temperatures. The phase transition from solution to solid state occurs around the 220 K, which can be seen from the dramatic drop of fluorescence intensity. The measured intensity drops because upon solidification, the light scattering by the sample dramatically increases. During the temperature decrease there is no shift in emission maximum and no spectrum evolution was observed.

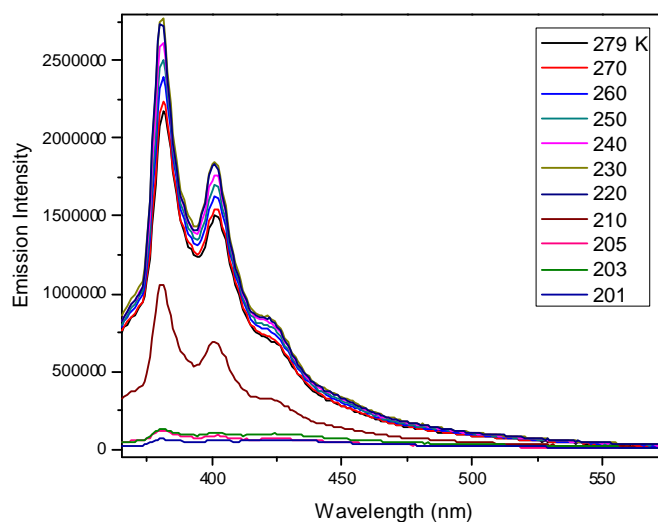


Figure 5-10. Low temperature fluorescence of Ti6 in acetonitrile

5.2.3 Raman spectrum

The Raman spectrum of Ti6 provides us with useful information on the surface ligands. The peak assignment is listed in the Table 5-2. The Raman peaks at 1027 and 1190 cm^{-1} are attributed to the isopropoxide ligand[1, 2], and correspond to the Ti-O mode coupled to C-O stretching and C-H wagging (shown in the Figure 5-5). The characteristic stretching mode of C=O of acetate group at Ti6 surface is red shifted to 1566 cm^{-1} from 1650 cm^{-1} in free acetic acid form[3], the reason for the red shift is that the acetate carbonyl group has less π -character when chelating with Ti atoms of cluster core. The electron is more delocalized in the functional group instead of mostly localizing on O atom as in the free acid. This delocalization averages the electron density which explain the red shift of C=O mode.

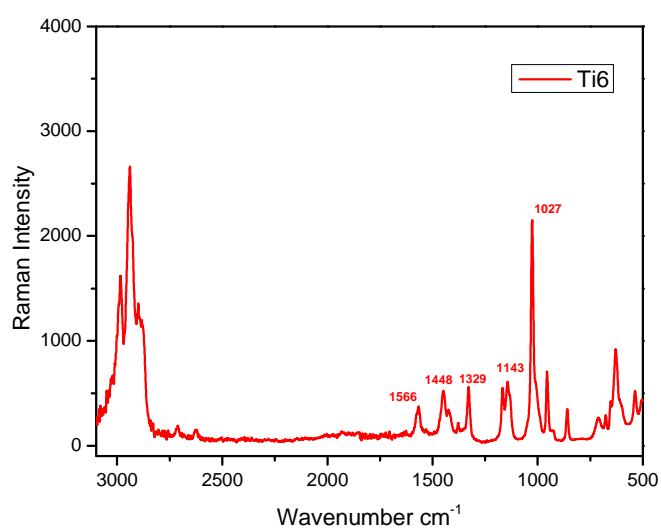


Figure 5-11. Raman spectrum of Ti6

Table 5-2. Assignment of the Raman peaks

1027	ν (C-O) of O ⁱ Pr	1032
1143	ν_{as} (C-C-C) of O ⁱ Pr	1131
1167	ρ_r (CH ₃) of OiPr	1171
1329	δ (CH) of O ⁱ Pr	1328
1380	ν_s (COO ⁻)	1376 1384
1448	δ_{as} (CH ₃) of O ⁱ Pr	1451
1566	ν_{as} (COO ⁻)	1582 1601

5.2.4 The transient absorption spectrum of Ti6

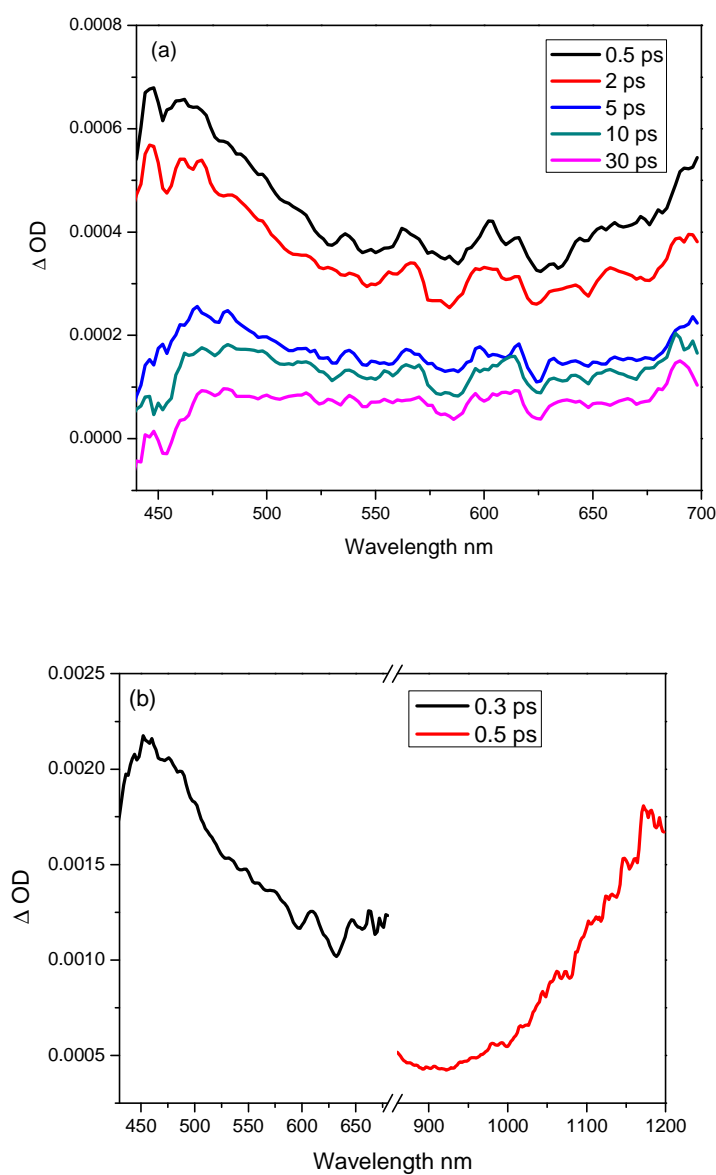


Figure 5-12. Transient absorption spectrum of Ti6 in (a) the visible range and (b) near IR range

The transient absorption spectrum of Ti6 was recorded from 420 to 700 nm region after being excited at 300 nm. The transient absorption spectrum displays a broad absorption band centering around 450 nm (2.76 eV). The maximum absorption position

shifts to long wavelength with decay time, which is ascribed to the vibration relaxation. This electronic transition at visible range corresponds to the d-d interband transition.

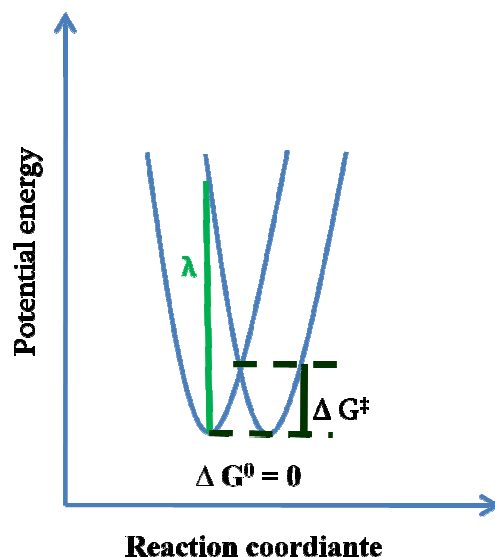


Figure 5-7. Potential energy description of an electron-transfer reaction with $\Delta G^0=0$

The transient absorption extends into IR range and the spectrum displays an absorption band with maximum ~1150 nm. The absorption band centering at 1150 nm is from the intravalence charger transfer (IVCT). The Marcus-Hush theory provided the analysis method for such intramolecular transfer[4-7]. For Guassian-shaped IVCT band,

$$V_{ab} = 2.06 * 10^{-2} \left(\epsilon_{\max} * v_{\max} * \Delta v_{\frac{1}{2}} \right)^{\frac{1}{2}} / (\text{br}) \quad (1)$$

ϵ_{\max} and b denote the maximum molar absorption coefficient of the IVCT band and the degeneracy of the transition, r is the distance between the metal centers. Since the concentration of excited state is unknown in this experiment, we cannot calculate the coupling strength.

$$\Delta G^{\ddagger} = \frac{(\lambda_o + \Delta G^0)^2}{4\lambda_o} \quad (2)$$

Since all the metal atoms are in same environment, the driving force for the electron transfer between two metal atoms is zero, i.e., $\Delta G^0 = 0$ as shown in Figure 5-7, then $\Delta G^\ddagger = \lambda_0/4$. Here the λ_0 corresponds to the maximum transient absorption. The transient absorption spectrum shows the maximum absorption is ~ 1150 nm, so the calculated barrier energy is ~ 0.26 eV by equation 2. This barrier energy is around 10 times higher than k_bT of room temperature. The electron transfer rate not only depends on the activation energy but more on electronic coupling between initial and final electronic states. Because $k_{ET} \propto |\langle \varphi_i | H | \varphi_f \rangle|^2 = |V_{if}|^2$, electronic coupling has a strong influence on the ET rate. In Ti6 cluster, the distance of Ti-Ti is ~ 3 Å, and the electronic states before and after ET are same for Ti-Ti, so the coupling is likely to be large. Based on the semi-classical Marcus Hush theory, $k_{ET} = |V_{el}|^2 \exp\left(-\frac{(\Delta E^0 - \lambda)^2}{4\lambda k_B T}\right) = |V|^2 \cdot e^{-10}$ should be large.

Based on the discussion on the transient absorption of cluster, we propose the energy level diagram of Ti6 cluster. After being excited, the electron in S_1 state either experiences the transition to even higher excited state or the intravalence charge transition to neighbored metal atom.

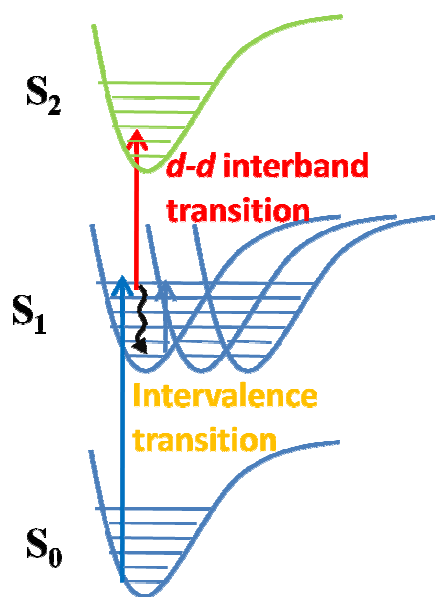


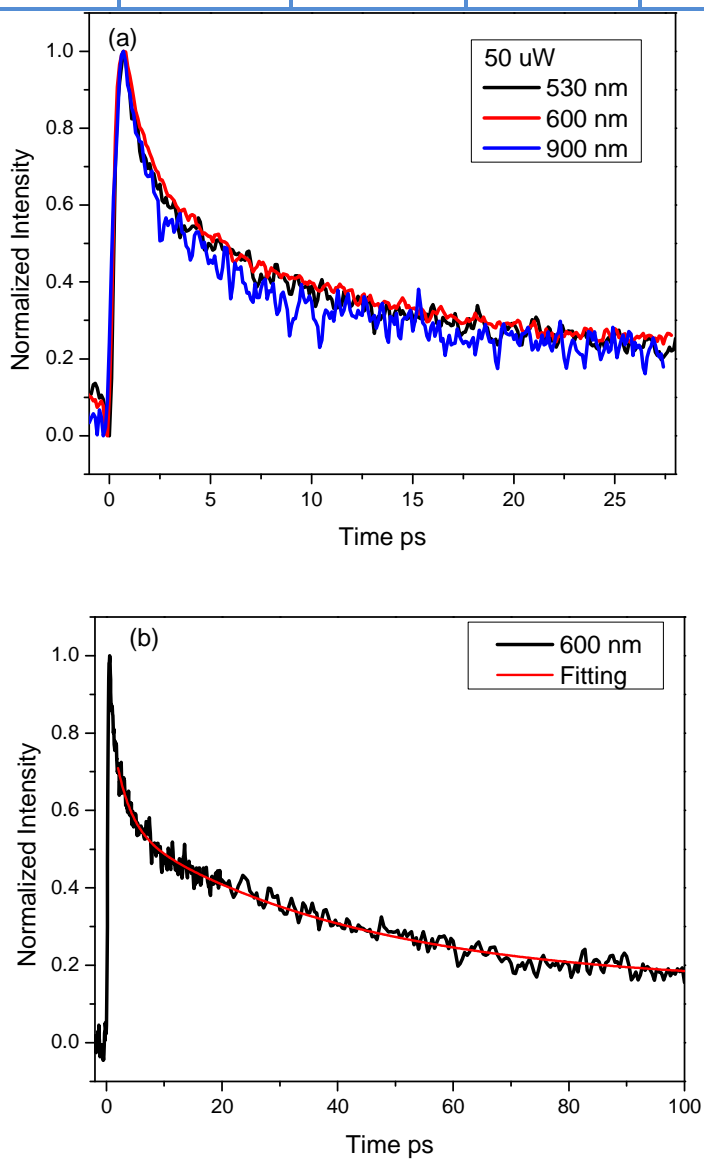
Figure 5-8. The electronic absorption diagram of Ti6

5.2.5 The transient absorption dynamics at different probe wavelengths

The transient absorption spectra of Ti6*, i.e. the excited state of Ti6, decay homogeneously, as shown in Figure 5-6a, which is consistent with the transient dynamics measured at different probe wavelengths shown in Figure 5-9, the dynamics behave very similar at 530, 600 and 900 nm. The kinetics in the 0-30 ps time window, which was examined most extensively, is dominated by two components, $\tau_1=1.14$ ps and $\tau_2=9.18$ ps, which together constitute ~ 80% of the overall decay (Figure 5-9 and Table 5-3). Since the data were collected in the “magic angle” configuration and the spectral evolution is minor, these rates reflect purely the population decay. The fastest picoseconds rate most likely corresponds to the geminate recombination of the initial electron-hole pairs which did not fully equilibrate with the phonon modes of the TiO core of the cluster. The surviving excitons decay with the rate τ_2 which is consistent with exciton recombination characterized by vibrational cooling.

Table 5-3. Exciton decay parameters measurement for Ti6 in dibutyl ether, excitation at 300 nm

τ_1 (ps)	A_1	τ_2 (ps)	A_2	τ_3 (ps)	A_3	A_∞
1.14 ± 0.06 ps	0.32 ± 0.01	9.18 ± 0.12 ps	0.48 ± 0.01	40.78 ± 0.80	0.11 ± 0.01	0.09 ± 0.01

**Figure 5-9.** Absorption dynamics of Ti6 at 530, 600, 900 nm in (a) 30 ps time window; and (b) the absorption dynamics at 600 nm in 100 ps time window

A 100 ps scan window helps us to determine the third decay time, $\tau_3 = 40.78$ ps, which we ascribe to the recombination of the fully relaxed, surface-stabilized exciton.

Fitting of the long scan transient dynamics always gives the component which does not decay at 100 ps time scale. The last component constitutes ~9 %. This may be caused by the presence of small amounts of impurities; it is plausible that the longest lived absorption component originates from the T_1 triplet state of the cluster.

The decay of the excited state of Ti6 follow a multi-exponential function which is similar to that of Ti17 cluster, but the decay rates and the corresponding amplitudes exhibit differences, which reflects both the similarity and the distinct character of the two clusters. For Ti6 the first two components decay slower than the corresponding components in Ti17, this dynamic difference would be linked to the molecular vs. nanoparticle-like behavior [8] .

5.2.6 Excitation power dependence of transient absorption dynamics

The transient dynamics measured at different excitation power shows the dependence on the excitation intensity. When the pump power changed within 50 to 250 μW , the normalized transient dynamics display same kinetic decay. But when the excitation power is more than 300 μW , the dynamics decay faster than that at low excitation intensity, moreover the traces at different probe wavelength also have different dynamic behaviors. The reason for that could be the two photon effect which induces the exciton annihilating[9-11].

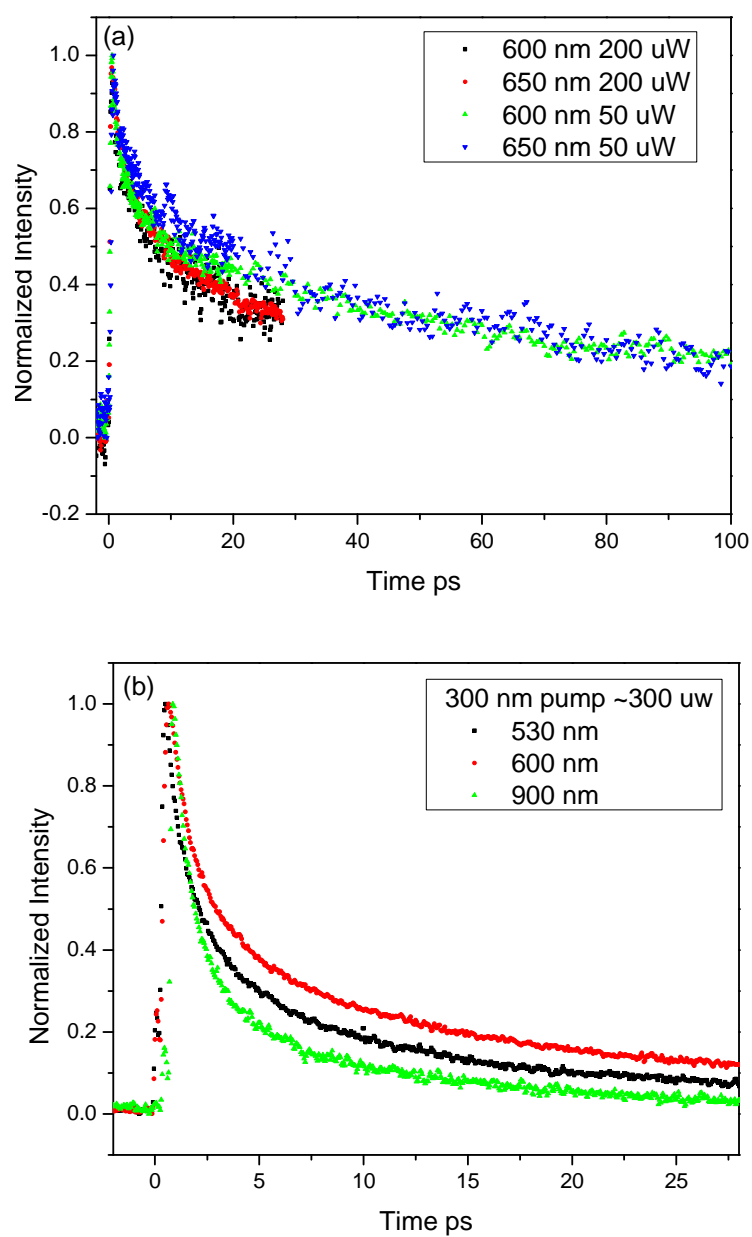
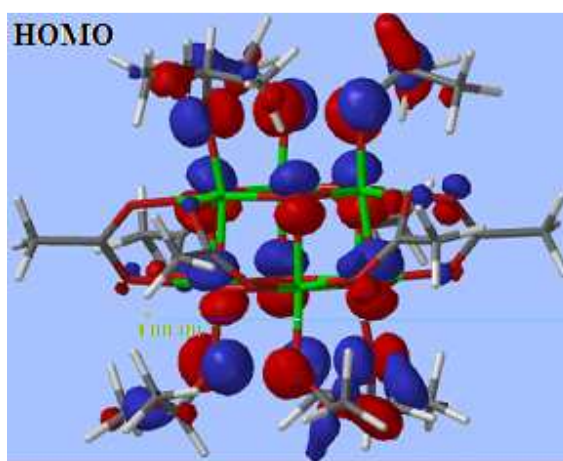


Figure 5-9. Excitation power dependence of transient dynamics at different probe wavelengths : (a)the normalized dynamics of 600 and 650 nm at 50 and 200 μW pump power, in 30 and 100 ps time window; (b)the transient dynamics of 530, 600 and 900 nm at 300 μW pump power.

5.2.7 Calculations on the Ti6 cluster

In order to theoretically explore the electron transfer at the interface of Ti6 cluster, the structure optimization and HOMO, LUMO calculations were carried using Spartan10. The configuration of Ti6 cluster was obtained by refining the X-ray crystal structure by geometry optimization with a semi-empirical method at PM3 level. The calculation on HOMO orbital indicates electron mostly locates on the oxygen atom of isopropoxide ligand and oxygen atom of the core, while the electron density locating on oxygen of acetate group is relatively low. The results demonstrate isopropoxide ligand has a much stronger binding with the Ti center than the acetate ligand. The electron density calculation on the LUMO orbital suggests that the absorption transition occurs from the oxygen of isopropyl group to the Ti atom, for the electron density on the oxygen experiences a huge decrease, and at same time the electron density inside of the cluster core increases a lot.



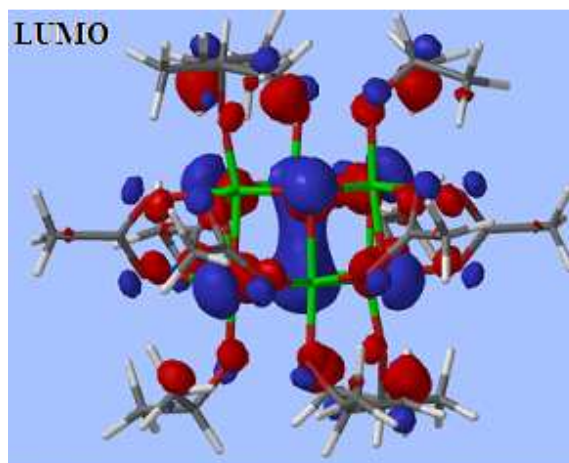


Figure 5-10. The calculated HOMO and LUMO orbitals of Ti6 cluster

Calculation results provide valuable insights to better understand the ground state absorption and the dynamic behavior of electron on the excited state.

5.3 Conclusions:

The Ti6 cluster exhibits primarily molecular characteristics. A series of clear vibrational peaks in the emission spectrum indicates a strong coupling between emission exciton and vibration mode of surface ligands, which also explains why the Ti6* is better stabilized than in Ti17 cluster. The close value of frequency difference from Ti6 and Ti17 clusters points to the fact that the isopropyl ligand on the two clusters has a significant influence on stabilization of exciton behavior. The specific vibration modes of Ti6 in Raman spectrum further confirm the existence of isopropoxide and acetate ligands on the surface.

The transient absorption spectra help us to establish the molecular transition diagram in Ti6 cluster. The excited electron experiences the d-d interband transition, the intervalence and vibrational absorption in Ti6 cluster. A multi-exponential function is

needed to fit the recombination dynamics of Ti6. The two fast components, 1.1 and 9 ps, accounting for ~80% of the total components, are mostly from recombination of the initial excitons and the relaxed ones by the surface ligands. The slower component ~42 ps is assigned to the decay of the fully relaxed exciton.

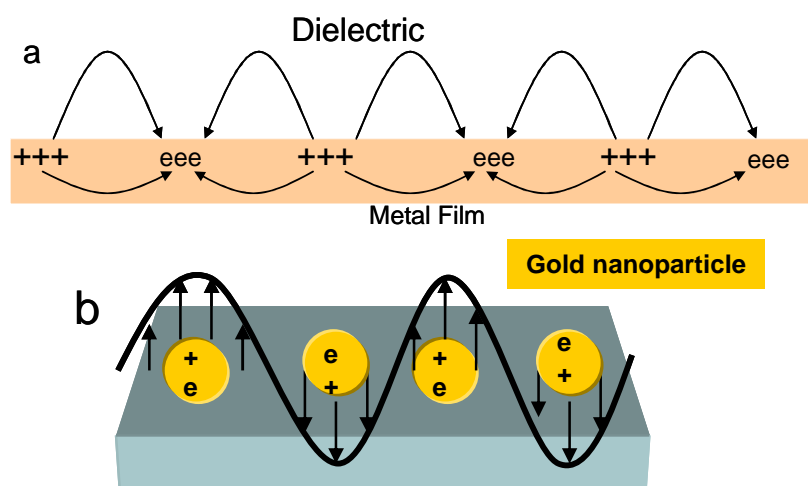
References

1. Moran, P.D., et al., *Vibrational spectra and molecular association of titanium tetraisopropoxide*. Inorganic Chemistry, 1998. **37**(11): p. 2741-2748.
2. Karatchevtseva, I., et al., *Crystallization of TiO₂ powders and thin films prepared from modified titanium alkoxide precursors*. Journal of the American Ceramic Society, 2008. **91**(6): p. 2015-2023.
3. Nakabayashi, T., K. Kosugi, and N. Nishi, *Liquid structure of acetic acid studied by Raman spectroscopy and ab initio molecular orbital calculations*. The Journal of Physical Chemistry A, 1999. **103**(43): p. 8595-8603.
4. Hush, N., *Intervalence-transfer absorption. Part 2. Theoretical considerations and spectroscopic data*. Prog. Inorg. Chem, 1967. **8**(391): p. 12.
5. Hush, N., *Homogeneous and heterogeneous optical and thermal electron transfer*. Electrochimica Acta, 1968. **13**(5): p. 1005-1023.
6. Marcus, R., *On the Theory of Oxidation - Reduction Reactions Involving Electron Transfer. II. Applications to Data on the Rates of Isotopic Exchange Reactions*. The Journal of Chemical Physics, 1957. **26**(4): p. 867-871.
7. Marcus, R.A., *On the theory of oxidation - reduction reactions involving electron transfer. I*. The Journal of Chemical Physics, 1956. **24**(5): p. 966-978.
8. Scholes, G.D. and G. Rumbles, *Excitons in nanoscale systems*. Nature materials, 2006. **5**(9): p. 683-696.
9. Klimov, V., et al., *Optical gain and stimulated emission in nanocrystal quantum dots*. Science, 2000. **290**(5490): p. 314-317.
10. Klimov, V.I., et al., *Quantization of multiparticle Auger rates in semiconductor quantum dots*. Science, 2000. **287**(5455): p. 1011-1013.
11. Valkunas, L., Y.-Z. Ma, and G.R. Fleming, *Exciton-exciton annihilation in single-walled carbon nanotubes*. Physical Review B, 2006. **73**(11): p. 115432.

Chapter 6 Enhancement of Fluorescence of P3HT Films on Nanostructured Gold Substrates

6.1 Introduction

Fluorescence is widely employed in optical devices, microscopy image, biology, medical research and diagnosis. All these applications require strong and stable fluorescence. Therefore improving fluorescence sensitivity to the limit of single-molecule detection remains a great challenge. Fluorescence is an example of spontaneous emission process. Spontaneous emission occurs when the excited electron in atom, molecule or ion undergoes a transition to a state with a lower energy (e.g. the ground state or intermediate energy level) and emits light. Since E. M Purcell first reported that the spontaneous emission could be modified through the coupling between the emitter and an external electromagnetic field[1], researchers have carried out extensive fundamental research and developed corresponding technological applications based on this phenomenon. One significant strategy to achieve fluorescence enhancement is the surface-enhanced



Scheme 6-1. Schematic diagrams: (a) flat metal surface plasmon; (b) localized plasmon of gold nanoparticle

fluorescence (SEF), it is also called metal-enhanced fluorescence (MEF). The SEF technique is based on designing and tailoring of metallic nanostructures placed in the vicinity of the emitter in order to modify the electromagnetic (EM) field around the fluorophore, and increase the near-field coupling between the emitter and metallic surface plasmons.

Surface plasmons (SP) are collective electrons/holes oscillation confined in the metal surface, and at the interface between any two materials with different refractive indexes, i.e. metal-air, metal-glass. Localized plasmons occur when the dimension of the metal nanostructure is comparable or less than the incident wavelength. **Scheme 6-1** shows the surface plasmon and localized metal plasmon. Since SP and localized plasmon are highly sensitive to the structure and the surroundings, researchers can manipulate plasmons through controlling the geometry of the nanostructures.

Plasmonic surfaces with localized and propagating surface plasmons are efficient SEF substrates. The strong localized electromagnetic field induced by the metallic nanostructures increases fluorescence efficiency, and decrease the excited state lifetime of the emitter through the increased coupling between the fluorophore and the electromagnetic field of the nanostructure. Furthermore, the presence of the surface plasmon enhances the electronic energy transfer (or intermolecular energy transfer) rate through the enhanced dipole-dipole interaction which is also associated with the localized electromagnetic field. As a result, a wide range metal nanostructures have been developed to enhance emission of fluorophores, such as continuous metal thin films, nanoparticles[2], nanotubes[3], nanorods[4] and nanowires. Currently the most commonly used noble metals are Au, Ag and Pt, because the surface plasmon oscillation

modes formed on noble metal structures can absorb, emit and scatter light in the visible region. SEF efficiently expands the sensitivity and applications of the fluorophore in clinical fields and single molecule imaging[5].

The mechanism of fluorescence enhancement has been studied in different fluorophores and metallic nanostructure systems. Recently, many fluorescent materials such as QDs, organic molecules and polymers have been studied as the SEF targets. Some of these have high fluorescence quantum yields. We chose P3HT to study the SEF effect at different metallic substrates. P3HT is the acronym for poly (3-hexylthiophene), Figure 6-1 shows its structure. P3HT is extensively used as the active layer in organic solar cells due to its low fabrication cost, easy solution processing and mechanical flexibility. Since the quantum yield of P3HT is very low, only around 2% in solid state [6], our goal here is to explore the fluorescence enhancement and convert P3HT from a poor emitter into a good one, thus increasing its practical significance.

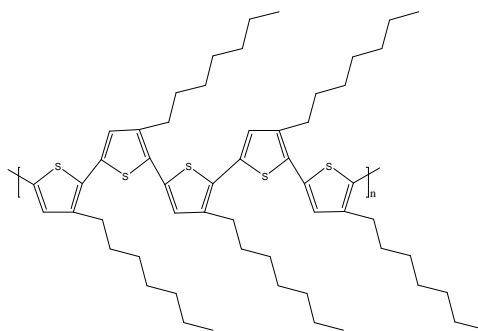


Figure 6-1. The structure of P3HT

As described in the equations, the quantum yield for solid P3HT film is mostly determined by κ_{rad} (radiative rate), κ_{EET} (electronic energy transfer or Förster resonance energy transfer), and κ_{ET} (electron transfer, or fluorescence quenching) constants. The decay rate change of different processes is related to the electromagnetic field of

nanostructure in proximity of emitter. Firstly the EM field enhances the excitation rate, at same time the emission rate also is enhanced as described in equation 3 and 4.

$$\Phi = \frac{\kappa_{rad}}{\kappa_{rad} + \kappa_{non-rad}} \quad (1)$$

and

$$\kappa_{non-rad} = \kappa_{IC} + \kappa_{EET} + \kappa_{ET}$$

$$\kappa_{EET} \propto E^2 \approx \left(\frac{\mu_D \mu_A}{R_{DA}^3} \right)^2 \quad (2)$$

$$\kappa_{exc} \propto |\mu \cdot E|^2 \quad (3)$$

$$\kappa_{rad} = \frac{1}{\tau_{rad}} \propto |\mu|^2, \quad f \propto \mu^2 \quad (4)$$

For the ET process there is no strong evidence to show that it will or will not be enhanced by surface plasmons, but it contributes a lot to the fluorescence decay especially when the emitter is very close to the metallic nanostructure. Other non-radiative processes such as the internal conversion also will influence the quantum yield, but the internal conversion rate is much related to the molecular structure, depends on the overlap of the electronic wave function, so the change of EM environment or the surface plasmon has little influence on it, thus it is considered as constant generally. Hence the quantum yield of P3HT film depends on the change of κ_{ET} , κ_{EET} and κ_{rad} as the Equation 5 describes. The quantum yield can be re-written by:

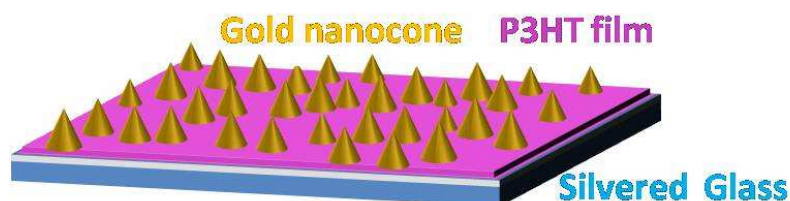
$$\Phi = \frac{\gamma \kappa_{rad}}{\gamma \kappa_{rad} + \gamma \kappa_{EET} + \kappa_{ET} + \kappa_{IC}} \quad \gamma = \frac{\kappa_{rad}}{\kappa_{rad}^0} = \frac{\mu_{effective}^2}{\mu_0^2} \quad (5)$$

γ is enhancement factor, it is the ratio of radiative rate with and without metallic nanostructure present. Our goal is to explore the influence of different solid metallic nanostructures on the same fluorescent material, and to improve the sensitivity of fluorescence detection through this project study.

Table 6-1. Samples on different metallic substrates

Sample 1	P3HT film on silver surface
Sample 2	P3HT film on silver surface with gold nanocones
Sample 3	P3HT film on rough gold surface (Klarite)

In this chapter we report extensive time-resolved fluorescence measurements which have been carried out to investigate the fluorescence enhancement on three different metallic nanostructure substrates. We named the P3HT film on three substrates as sample 1 to sample 3. Sample 1 and sample 2 are P3HT films spin cast on smooth silver surface (50 nm, supplied by Dr. O'Carroll group), the difference is gold nanocones oriented on P3HT film through alumina template method on sample 2. Sample 3 as shown in Figure 6-2 is P3HT film prepared with same method on rough commercial Klarite which is a substrate used for Surface Enhanced Raman spectroscopy (SERS). We observed the enhanced fluorescence intensity of P3HT on these three metallic substrates through the time-resolved fluorescence measurements. The lifetimes of P3HT films are reduced to tens of ps from 400 ps which corresponds to the P3HT film on glass surface[7].



Scheme 6-2. Schematic diagram of P3HT film with gold nanocone on silver

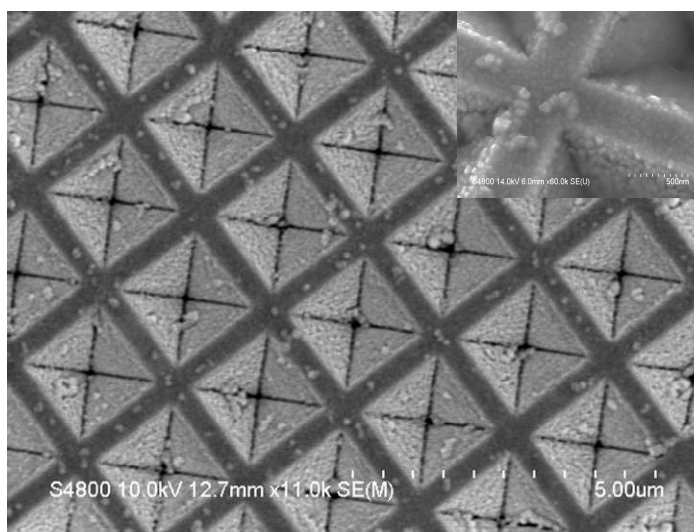


Figure 6-2. SEM image of Klarite

The spectrum shape of time resolved fluorescence of sample 2 and 3 at same specific time displays big difference which shows that the resonance surface plasmons from the substrate with Au NCs differs from that of rough gold surface of Klarite. Through comparison of the results we have a better understanding on the relationship between the resonance surface plasmon and metal structures, and their effect on the κ_{et} , κ_{exc} and κ_{rad} .

A big blue shift was observed in fluorescence spectrum of P3HT film with Au NCs on it. It resulted from the fast-dynamics surface enhanced fluorescence (FDSEF)[8], the total decay rate is comparable to the internal conversion rate due to the broad surface plasmon resonance from the gold NCs. Another very important observation on sample 2 is that it did not display the evolution progression between two emission bands recorded in P3HT film on silica[7]; the possible reason could be the emission from lower vibration level is much less populated due to the increased radiative decay. The enhancement factor

at different wavelength can be read from the slopes of decay kinetics, the high enhancement occurs at different frequency for Klarite and gold NCs substrates.

The fluorescence time profiles of varying thicknesses film on different metallic substrates demonstrate that the electron transfer accounts for a large part of the emission decay when the fluorophore is in contact with metallic surface. The distance dependence of electron transfer is relatively stronger than that of radiative processes.

6.2 Results and discussion

6.2.1 P3HT film on glass

6.2.1.1 The ground state absorption spectrum

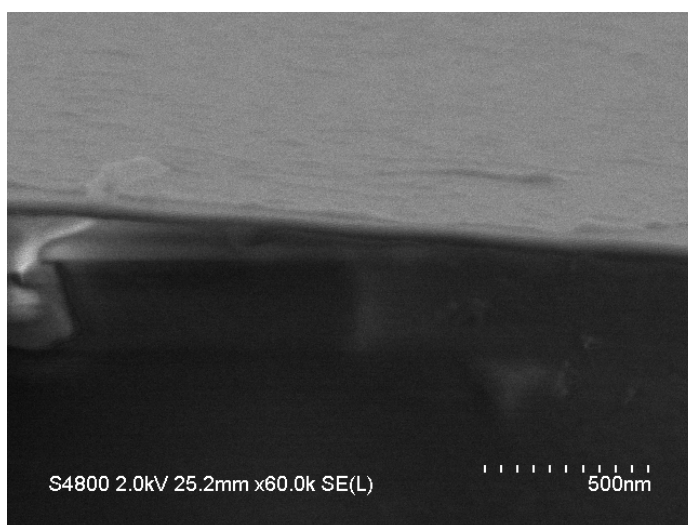


Figure 6-3. The SEM image of P3HT film on glass

The P3HT film was prepared from a 2 mg/ml chlorobenzene solution by spin coating. The SEM image indicates the formed polymer surface is relatively smooth; the thickness of the film is homogeneous and approximately 50 nm.

The steady-state absorption of P3HT on glass displays a shoulder at ~600 nm as shown in Figure 6-4a the red line, and the maximum absorption is around 550 nm which

was assigned to the π - π^* interband transition. Compared to P3HT in solution, the absorption band of the film exhibits a red shift. In addition, the film shows absorption structure at 600 and 550 nm, which was attributed to the configuration (H aggregates) formed on the glass substrate that is different from its flexible state in solution.

The emission spectrum was recorded with excitation at 490 nm. The spontaneous emission is low and the fluorescence spectrum has two broad bands corresponding to the 0-0, 0-1 transitions of C=C stretching vibration, the emission shape is similar to the fluorescence spectrum of P3HT in solution.

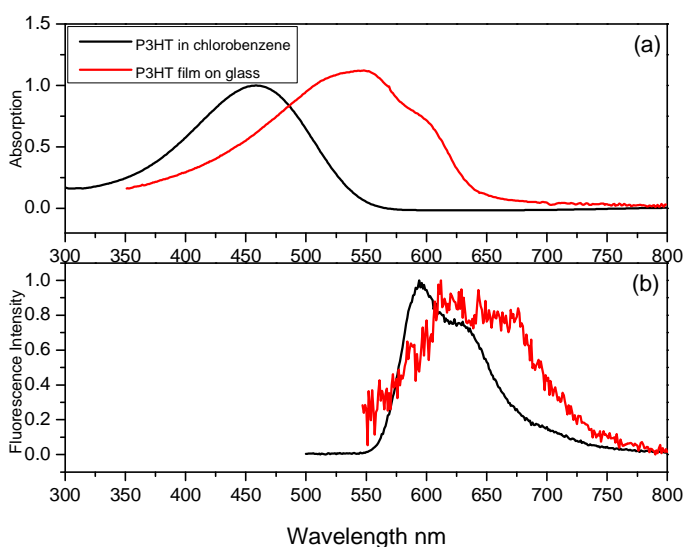


Figure 6-4. The steady-state absorption (a) and fluorescence spectra (b) of P3HT in chlorobenzene and a 50 nm P3HT film on glass

6.2.1.2 The fluorescence decay profiles of varying thickness P3HT films on glass

Femtosecond Kerr-gated fluorescence microscopy is a powerful technique; it not only considerably improves the time resolution for fluorescence measurements down to the sub-100 fs domain, it can also supply a 2D time-related fluorescence images

simultaneously. Due to the high time resolution this technique allows us to have even closer look at the fluorescence evolution. After being excited at 490 nm, the fluorescence light together with scattered light was focused onto the Kerr material, a slice of silica (0.5 mm) where it overlaps with the 800 nm gate beam spatially and temporally. The rotated fluorescence pass through the third objective and is detected by a CCD camera. The residual scattering and gate light were blocked by the second polarizer and a band pass filter (Please refer to the experiment setup in the Experiment Chapter).

We used femtosecond fluorescence microscopy to measure the fluorescence dynamics of the P3HT film on silica, silver and Klarite surface. Since there is a very weak enhancement effect on glass surface compared to the metallic nanostructures, the P3HT film on the glass can serve as the reference sample to study the fluorescence enhancement of P3HT films on other metallic nanostructures, and the distance dependence of radiative and electron transfer processes varying with the film thickness on different substrates.

Figure 6-5 shows that for a 30 nm P3HT film its emission decay profile displays an increasing process and constant emission intensity during 5 ps time scale. The fluorescence dynamics of 10 nm P3HT film on the glass shows much weaker fluorescence signal at time zero compared with that of a 30 nm film.

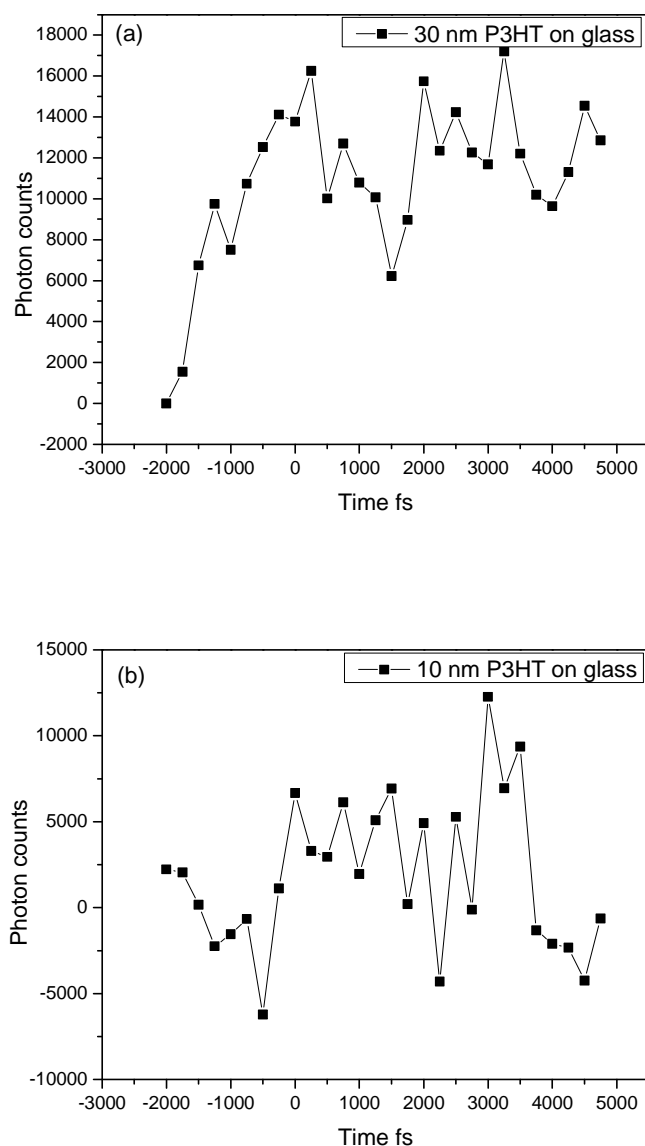


Figure 6-5. Time-resolved fluorescence: (a) 30 and (b) 10 nm P3HT films on glass

6.2.2 P3HT film on smooth silver surface

6.2.2.1 The steady-state absorption spectrum

As displayed in **Figure 6-6**, the steady-state absorption spectrum of P3HT film on silver shows a broad absorption band with maximum absorption at 546 nm which is

consistent with the P3HT film on glass, that can be explained by the similar aggregation of P3HT formed on these two substrates. The transition corresponds to the π - π^* interband absorption[7]. While with Au NCs oriented on the P3HT film it exhibits a much more broader absorption band with similar absorption maximum at 546 nm and extending 250 nm beyond the absorption edge of P3HT/Ag, the broad absorption originates both from the enhanced absorption of P3HT, the plasmon resonance and scattering by gold nanocones[9-15].

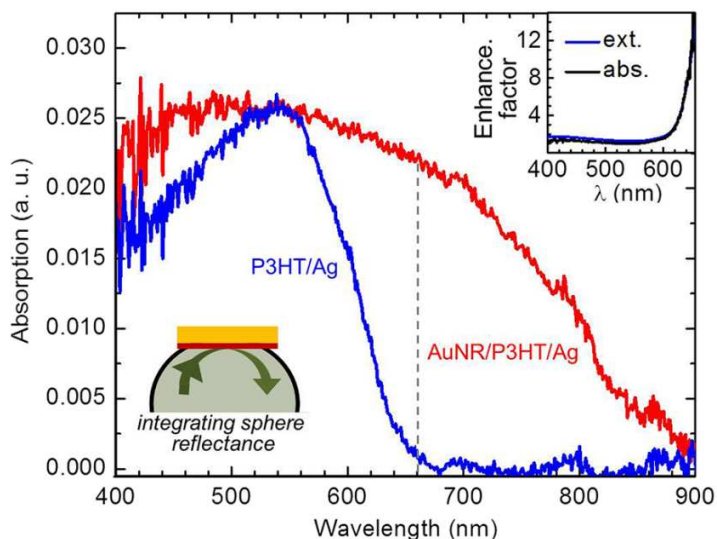


Figure 6-6. Absorption spectrum of P3HT on silvered glass (blue line) and with gold NCs (red line)[9]

6.2.2.2 The fluorescence dynamics of P3HT films on flat silver surface

Under same preparation and measurement conditions, the fluorescence of the P3HT film on silver shows an instantaneous rise of signal and reduced lifetime in comparison with the film on silica. A double exponential function was used to fit the decay of the 30 nm film on silver. The result shows the fluorescence intensity loses ~80% in less than 2 ps. The fast component $\tau_1=0.20$ ps is attributed to the accelerated radiative decay and the

electron transfer from P3HT molecules to the silver surface; the second time constant $\tau_2=2.2$ ps could be assigned to the radiation from the localized exciton. Most importantly, the fluorescence results clearly demonstrate the fluorescence enhancement from the resonance surface plasmon.

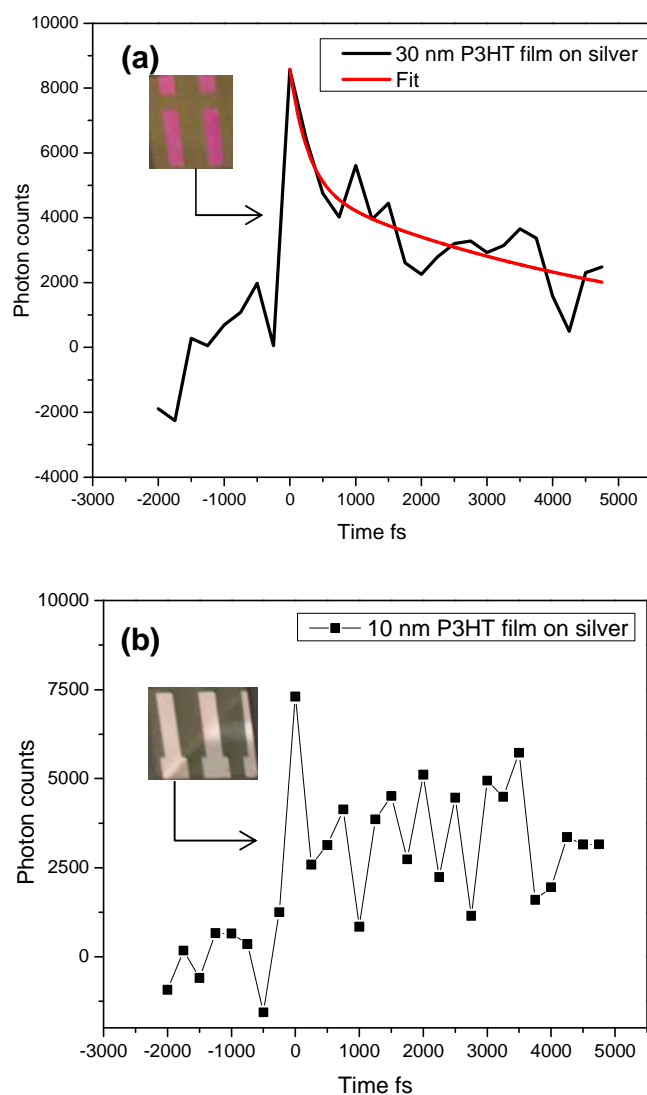


Figure 6-7. Fluorescence dynamics of (a) 30 and (b) 10nm P3HT film on silver

Table 6-2. Decay parameters of fluorescence dynamics of 30 nm P3HT film on silver

	A_1	τ_1	A_2	τ_2	y_0
Without Au NC	0.33 ± 0.18	0.20 ± 0.23	0.47 ± 0.11	2.2 ± 0.8	0.2

6.2.2.3 The competition process between radiative and electron transfer

The fluorescence dynamics of films of varying thickness on silver substrates provides information on the competition process between the radiative decay and the fluorescence quenching induced by electron transfer, as shown in **Figure 6-7**. The 10 nm P3HT film shows rapid increase and decrease in fluorescence intensity, we could not observe the normal decay process due to the overwhelming contribution from electron transfer. The fluorescence decay from 30 nm film exhibits the enhanced emission intensity, and the fluorescence decay can be fitted by single exponential function. It is obvious that the quenching process dominates the fluorescence decay in 10 nm film; while in 30 nm film the contribution from radiative process exceeds the quenching process. The resonance surface plasmons have a strong influence on the electron transfer process, especially when the fluorophore-metal distance is in the regime of the near-field coupling which leads to accelerated electron transfer. However, the distance dependence of ET rate is more sensitive than radiative decay. The quenching rate yields a $1/d^4$ dependence on the distance, and there have been many studies on the distance dependence of fluorescence quenching in metal nanoparticle systems [16-21]. We can conclude that the quenching process dominates the decay when the spacer layer is less than certain thickness, but with the thickness increasing the radiative process began to be the predominate one. Based on the experimental results we propose the distance dependence of emission and electron transfer processes as shown in Figure 6-8. The simulated radiative and quenching rate

based on the fluorescence dynamics shows that the quenching process is the predominant one when $d < 15$ nm, conversely radiative decay contributes more than quenching process when $d > 15$ nm.

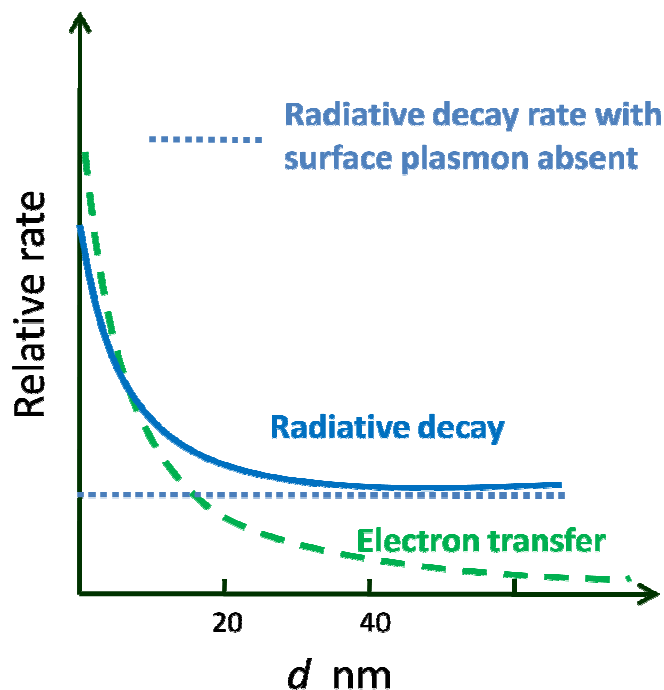


Figure 6-8. Simulated relative radiative and quenching rate as a function of distance between P3HT and silver film

After the fast radiative and quenching processes there still some long lifetime component left even in the 10 nm film. Limited by the 5 ps time window we could not obtain the exact time constant for the slow component. The long lifetime component only accounts for 20%, which is assigned to the relaxed exciton lifetime. The lifetime of exciton in P3HT film on glass is around 470 ps which is much longer than tens picoseconds estimated from our measurements. The lifetime of relaxed exciton under the

effect of surface plasmons also was highly enhanced. Another possible reason may relate to the molecule conformation, and from the polaron state [6].

6.2.3 P3HT film with gold nanocone array (Au NC) on silvered glass

6.2.3.1 SEM image of gold NCs/P3HT/silver

Scheme 6-2 shows the assembly of P3HT film with Au NCs on silvered glass. Figure 6-9 displays the top view of Au NCs and alumina template, the Au NCs locates in the lower part and the template is in the upper part of image. The diameter of Au NCs oriented on 50 nm P3HT film is ~ 100 nm and the preparation detail of Au NCs can be found in the literature[9]. Consistently, the diameter of the template hole is ~ 100 nm which is same to that of the prepared Au NCs. The height of nanocone is around 100 nm, and the space between any two nanocones is 50 to 100 nm. The fluorescence dynamics of varying thickness P3HT with and without Au NCs have been studied. The film thickness ranges from 30 to 50 nm.

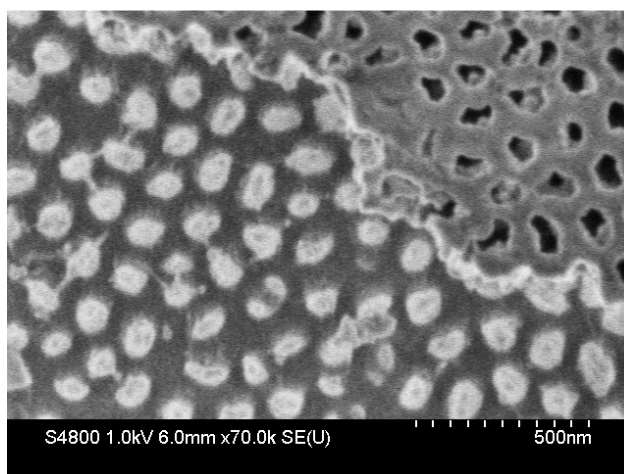
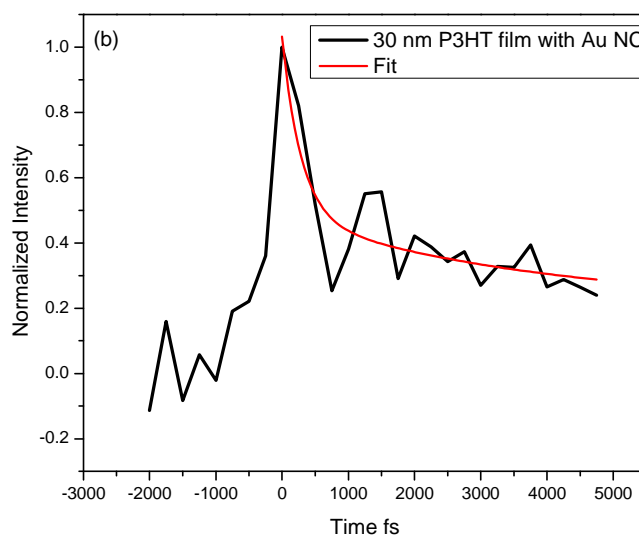
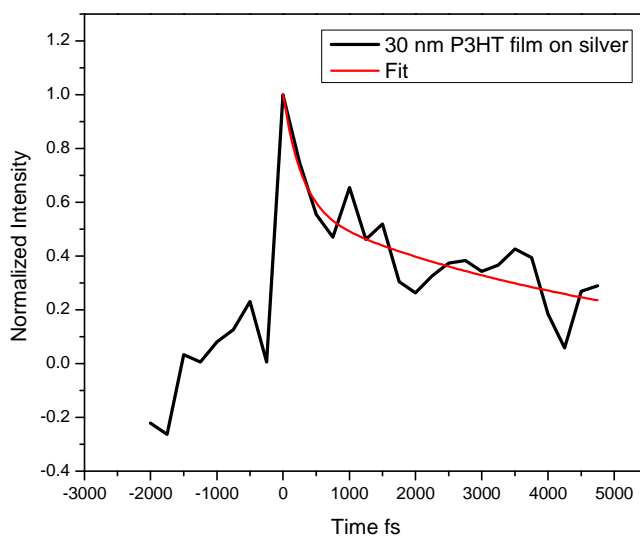


Figure 6-9. SEM image of the top view of gold NCs (the lower part) and Al_2O_3 template (the upper part)

6.2.3.2 Time-resolved fluorescence dynamics of 30 nm P3HT with and without gold NCs



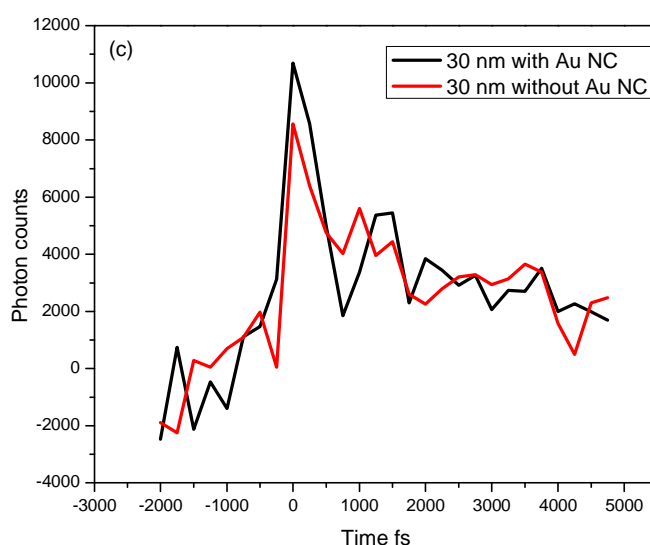


Figure 6-10. The fluorescence decays of 30 nm P3HT film on silver (a) with and (b) without 100 nm Au NC on it

Table 6-3. Time constants for 30 nm P3HT film with and without Au NCs

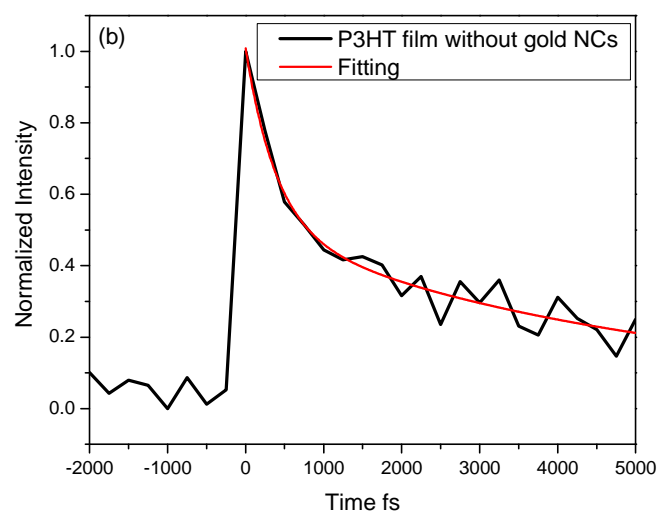
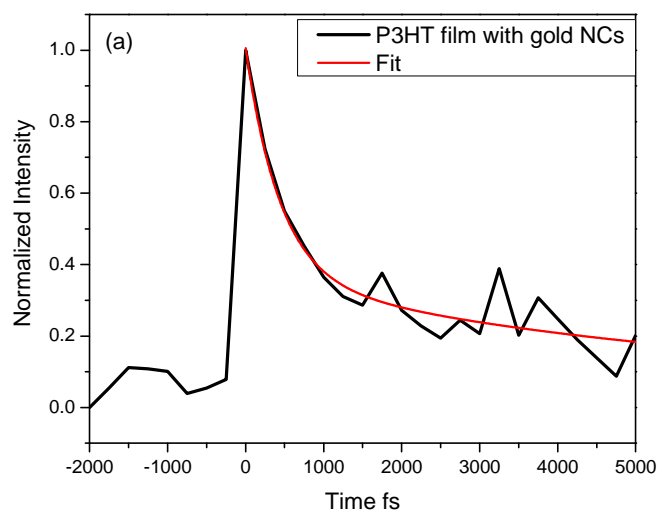
	A_1	τ_1 (ps)	A_2	τ_2 (ps)	y_0 (fixed)
With Au NC	0.54 ± 0.15 54%	0.29 ± 0.16	0.25 ± 0.13 25%	3.8 ± 2.5	0.21
Without Au NC	0.33 ± 0.18 33%	0.20 ± 0.23	0.47 ± 0.11 47%	2.2 ± 0.8	0.20

The fluorescence of 30 nm P3HT films with Au NCs presence and absence are both enhanced, but the fluorescence dynamics of P3HT film with gold NCs exhibits even stronger fluorescence intensity and faster decay compared with that of film without Au NCs as shown in Figure 6-10. The fitting results of double exponential function of two fluorescence traces manifest stronger enhancement from localized plasmon. Although the fastest time constants are same from these two samples, the percentage of fast component has a 21% increase in comparison to film without Au NCs, which demonstrates the

localized electromagnetic field from Au NCs is responsible for the fastest component increase.

6.2.3.3 Time-resolved fluorescence dynamics of 50 nm P3HT with and without gold NCs

Figures 6-11a and b show the fluorescence time profiles of 50 nm P3HT film with and without vertically-oriented Au NCs on it. The instantaneous increase of fluorescence and fast decay indicate the strong fluorescence enhancement on 50 nm P3HT films. Similarly to 30 nm films with and without Au NCs, the fluorescence intensity of 50 nm P3HT film with NCs at time zero is ~3000 counts higher than that with NCs absent. As shown in Table 6-4 the time constants of fastest component for the 50 nm film with and without Au NCs are very close, but the corresponding compositions are 64.0% and 49.4 % for Au NCs present and absent, respectively. Around 16% increase was observed for the fluorescent molecule in 50 nm P3HT film locating close to the localized Au NCs. The fitting results from 50 nm films provide the evidence that the stronger enhancement occurs with Au NC presence.



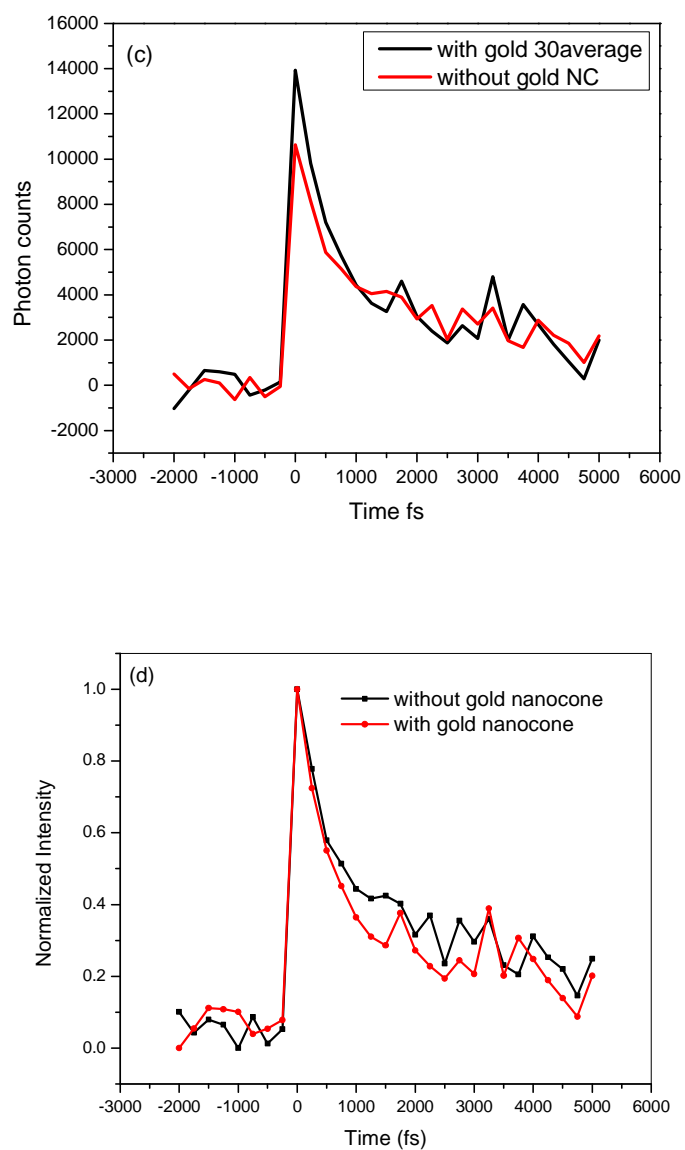


Figure 6-11. The fluorescence decay of 50 nm P3HT film on gold film (a) with and (b) without 100 nm Au NCs on it, (c) the comparison of original fluorescence data and (d) the normalized emission decays

Table 6-4. Time constants comparison of 30, 50 nm P3HT film with and without Au NCs.

	A_1	τ_1	A_2	τ_2	y_0 (Fixed)
30 nm without Au NC	0.33 ± 0.18 33%	0.20 ± 0.23	0.47 ± 0.11 47%	2.2 ± 0.8	0.20
50 nm without Au NC	0.50 ± 0.10 49.4%	0.39 ± 0.12	0.46 ± 0.07 45.6%	4.81 ± 1.18	0.05
30 nm film with Au NC	0.54 ± 0.15 54%	0.29 ± 0.16	0.25 ± 0.13 25%	3.8 ± 2.5	0.21
50 nm with Au NC	0.64 ± 0.11 64.0%	0.44 ± 0.14	0.31 ± 0.10 30.0%	5.49 ± 3.02	0.06

The time constants comparison of 30 and 50 nm films shown in Table 6-4 provide two important conclusions. One is that the time constants from 30 nm films are a bit faster than its counterpart in 50 nm films. This can be explained by the different distance dependence of radiative and electron transfer processes, the ET process contributes more to the decay in 30 nm thickness film. The other important information is that the fastest component counts more in 50 nm films than its counterparts in 30 nm films. The reason for that could be the contribution of radiative process is more from a 50 nm film than a 30 nm film.

Based on the results of the fluorescence enhancement on varying thickness films with and without gold NCs, we can see the fluorescence efficiency was enhanced by the presence of the gold nanocones which was ascribed to the increased density of the optical field at the transition frequency (photonic mode density, PMD) around the P3HT film. The fluorescence enhancement brought by Au NCs is even stronger compared to that without NCs. Although the P3HT surface is reduced by 15-18% due to the introduction

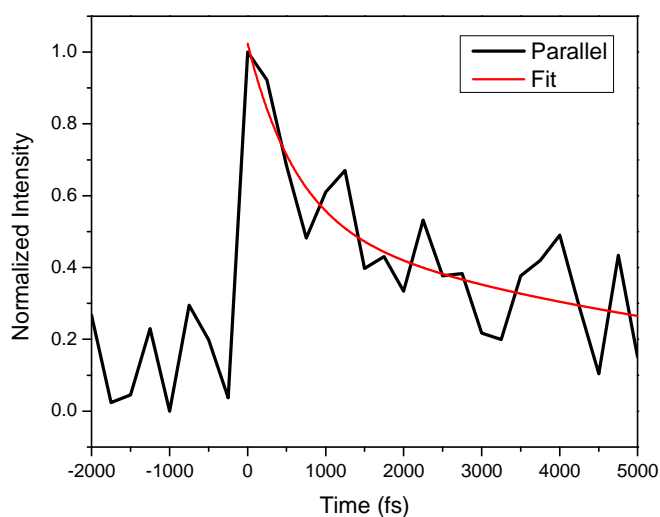
of gold NCs which at same time increases the electron transfer rate to gold nanostructures. We still observed ~ 15-20% increase in fastest component composition.

6.2.3.4 Fluorescence anisotropy measurement

In order to study the interchain, intrachain energy transfer, and the effect of surface plasmon on these processes, we conducted the fluorescence anisotropy measurements on the P3HT film with Au NCs. The emission polarization-sensitive measurements are conducted through setting the polarization plane of excitation as parallel or perpendicular to the polarization of gate beam. The molecules will be excited firstly when their absorption transition dipole moments are aligned with the same polarization plane as excitation, so anisotropy is highest at the excitation moment. In the solid P3HT state, the free molecular motion and rotation are limited, and the orientation of the transition dipole moment changes mostly through the intermolecular energy transfer[7] or intramolecular process which is associated with inter-chain or intra-chain interaction. The energy transfer through dipole-dipole interaction induces depolarization, and the anisotropy decreases with time which is disturbed by the energy transfer process. When the polarization of excitation is perpendicular to gate beam, the decay is determined by the rate of emission dipole moment reorientate to that polarization. The results are shown in Figure 6-12, the emission time profile measured at parallel and perpendicular polarization show a similar depolarization progression at 50 nm P3HT film with gold nanocone on it. The fitting results for the two polarization dependent decays are very close to each other as shown in Table 4. The obtained time constants are also similar to the counterparts of emission measured at the magic angle. The most plausible explanation is the energy

transfer rate being enhanced due to the localized surface plasmon. Banerji and his colleagues measured the anisotropy of P3HT films on silica. The anisotropy from films is ascribed to the exciton hopping between neighboring polymer chains. Another possible reason for that could be the assembly of P3HT molecules in film is random, which results in the anisotropy.

The presence of the metal surface plasmon[22] and the localized plasmon[23-26] can modify/reorient the transition dipole moment of the P3HT to increase the energy transfer rate between neighboring polymer chains. This accelerates the depolarization process. The enhanced fluorescence of P3HT film on silver surface with gold NCs demonstrates the accelerated radiative and electron transfer processes. In addition, the electronic energy transfer process also is accelerated.



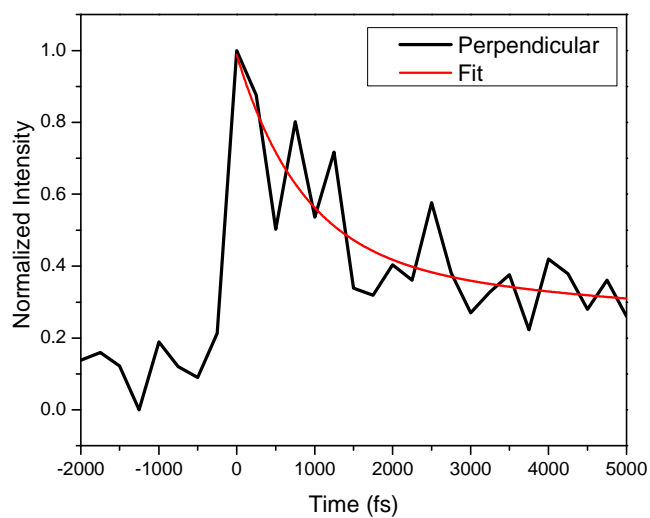


Figure 6-12. Anisotropy measurement of 50 nm P3HT film with Au NCs on silver modified glass

Table 6-5. The fitting parameters for polarization-sensitive measurement

	A_1	τ_1 (ps)	A_2	τ_2 (ps)	y_0 (fixed)
Parallel	0.47 ± 0.30	0.6 ± 0.6	0.45 ± 0.31	5.01 ± 4.90	0.10
Perpendicular	0.56 ± 0.46	0.84 ± 0.86	0.21 ± 0.48	6.53 ± 22.79	0.21

6.2.3.5 Time-resolved fluorescence spectra

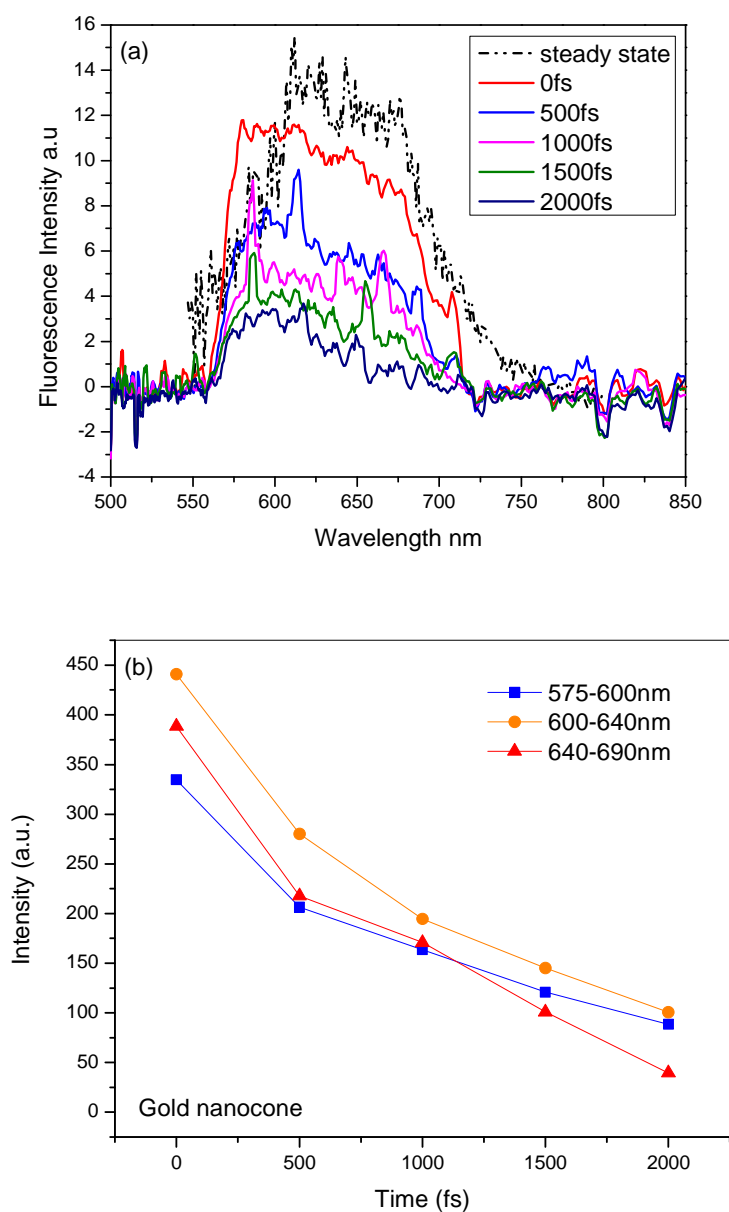


Figure 6-13. (a) Time-resolved fluorescence spectrum of 50 nm P3HT with Au NC at different time; (b) the decay kinetics based on the time-resolved emission spectra

The time-resolved emission spectrum covering the region from 585-725 nm provides us with significant information related to the earliest ~100 fs processes after photoexcitation. The ultra-fast fluorescence spectra show 0.5 ps evolution, and the shape of emission spectrum did not change much during the following 2 ps time period; only

the intensity decreased with time. Compared to the steady state emission spectrum, the time-resolved fluorescence spectra show the presence of Au NCs enhancing the emission at short wavelengths.

The emission modification of P3HT film with gold NCs shows ~ 25 nm blue shift with respect to its free-space emission on silica as shown in Figure 6-13a. The blue shift in emission spectrum resulted from a process known as fast dynamic surface-enhanced fluorescence (FDSEF) [27, 28]. So far only a few reports are available on the spectral modification [8, 28-30]. The fast dynamic surface plasmon resonance (FDSPR) process is related to the surface plasmon resonance and hot spot density of the media, the high localized near-field density from the metal nanostructure affects the electronic dynamics of fluorophore molecule, which makes the total decay rate comparable to the internal relaxation rate, then the emission transition occur from the vibrational state $S_1(\omega_v)$ instead of the $S_1(\omega_s)$ leading to the blue shift in emission. Another evidence supporting the point is we did not observe the evolution process involved between 0-0 and 0-1 transitions of C=C stretching vibration mentioned in Banerji's paper, and they used 500 nm light as the excitation wavelength. The reason for this can be explained by the increased radiative decay resulting in much less electron population on the vibration state $S_1(\omega_0)$. In our case the gold nanocones display a broad surface plasmon resonance which can be seen from the enhanced absorption which extends to IR region.

When the localized surface plasmon resonance (LSPR) energy matches with the transition energy between two levels, it increases the excitation rate and radiative decay rate, which resulted in the internal relaxation rate comparable or slower than $k_{\text{rad}} + k_{\text{non-r}} + k_{\text{ET}}$, then we observed emission spectrum shift to blue side.

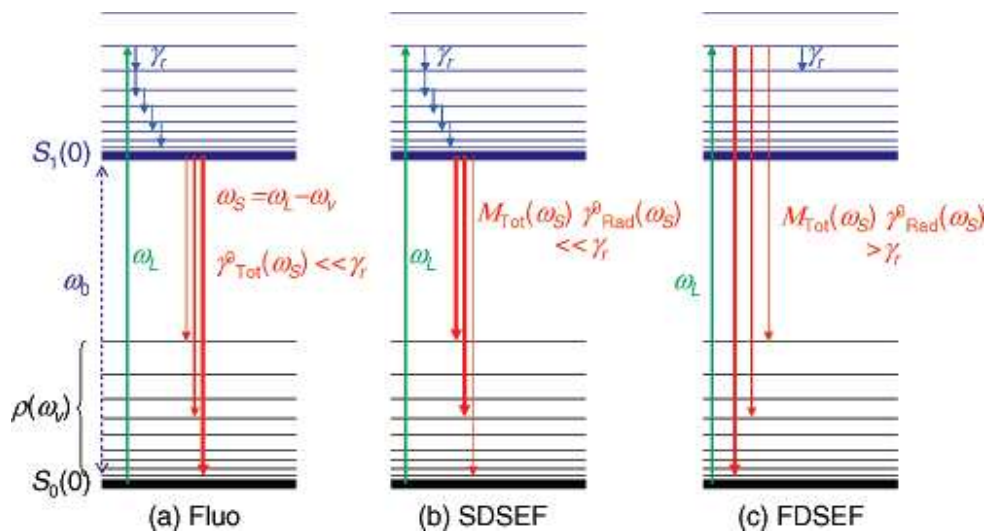


Figure 6-14. Simplified Jablonski diagrams: (a) Standard fluorescence, (b) Surface-enhanced fluorescence in slow dynamic regime, (c) Surface-enhanced fluorescence in fast dynamic regime [26]

The emission spectrum at 0.5 ps shows that its emission intensity was reduced to 50% of the maximum at 0 fs, which ascribed to the enhanced radiative and the electron transfer process as previous discussion. The following decay is relatively slower than the initial 0.5 ps, and the surviving electrons may experience the relaxation and localization to form singlet excitons and hop among the neighboring P3HT molecules.

In order to study the emission decay rate at different wavelengths, we divided the fluorescence spectrum into three wavelength ranges (575-600 nm, 600-640 nm and 640-690 nm), plot the integrated of luminescence intensity vs. time. The results are shown in Figure 6-13b. The slope and intensity change of each curve provide qualitative information on the wavelength dependence of fluorescence enhancement. There exist two distinctive decay rates during 2 ps for all three wavelength ranges, and they have the similar decay trend. A relatively sharp decay occurs within the earliest 0.5 ps and

followed by a slow decay. The dynamics of 640-690nm region decays fastest among three ranges, and the dynamics for 580-600 nm is the slowest. These contrasting rates imply that the long wavelength emission is more enhanced which is consistent with enhanced absorption of the same sample. As shown in the inset of Figure 6-6 the absorption enhancement factor for P3HT film with Au NCs on silver increase rapidly above 600 nm.

6.2.4 Results and discussion on the fluorescence enhancement of P3HT film on Klarite

6.2.4.1 SEM results

Figure 6-1 displays the surface morphology of Klarite. The surface is very rough, with gold nanoparticles spread randomly on the surface. The detailed surface structure in Figure 6-15 shows the surface was formed from tightly packed gold nanoparticles (~50 nm), and the cross-sectional SEM image of P3HT on Klarite substrate allows us to have a closer view of the polymer film. 5~10 nm thickness P3HT film rests on top of the ~100 nm gold layer. Due to the roughness of the surface, the contact between P3HT and the gold surface may vary from the top to the bottom of the pyramids. This feature plays a critical role in fluorescence enhancement because of the distance dependence of fluorescence enhancement. On the other hand, the physical contact between the film and the gold substrate gives rise to fluorescence quenching through interfacial electron transfer.

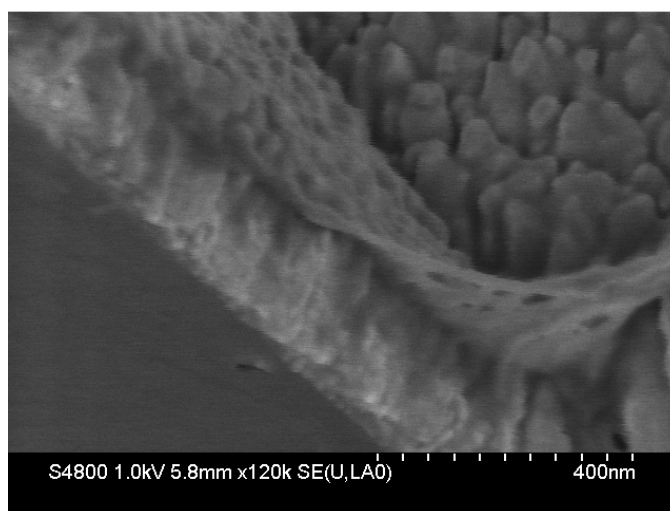


Figure 6-15. The SEM image of the cross-section of Klarite with P3HT film on it

6.2.4.2 Fluorescence lifetime measurement results and discussion

The same concentration solution and spin-coating procedure were used for Klarite substrates and glass slides. The contact angle of P3HT solution is different for glass and gold surface which results in the thickness variation under same preparation conditions. With the excitation at 490 nm, the emission time profile of P3HT film on Klarite indicates the instantaneous fluorescence. The inset in Figure 6-16 shows the extremely fast rise within < 50 fs. The emission experienced the accelerated decay which leads to $\sim 80\%$ fluorescence intensity lost during 1 ps scale. A double exponential function was employed to fit the emission time profile. The fastest component 0.31 ps accounts for 66.0% and the slow component 4.34 ps is about 24.0%. The fast component is assigned to accelerated radiative emission and the electron transfer from P3HT to gold substrate, and the second time component corresponds to the relaxation of surviving excitons. The time constants did not show a big change in comparison to the their counterparts in P3HT film deposited on silica [28], but the percentage of the first two time components is up to

90 percent of the whole intensity for P3HT on Klarite. The results reflect the fluorescence enhancement by the Klarite surface.

Table 6-6. The fitting parameters for 20 nm P3HT film on Klarite

	A_1	τ_1 (ps)	A_2	τ_2 (ps)	y_0
P3HT film on Klarite	0.68 ± 0.08 68.0%	0.31 ± 0.08	0.23 ± 0.07 23%	4.34 ± 1.92	0.09

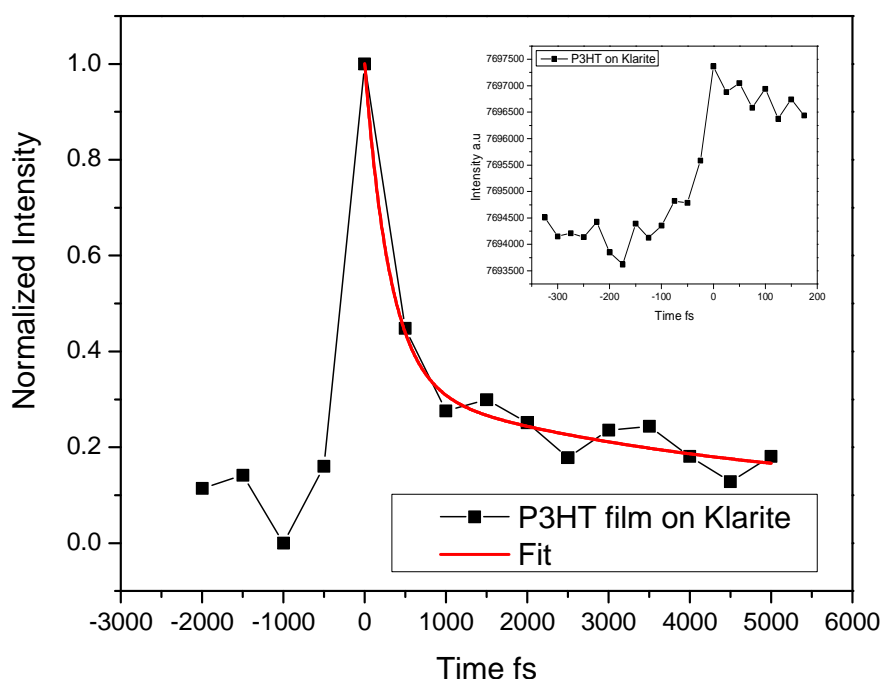


Figure 6-16. The fluorescence dynamics of P3HT film on Klarite, inset is the fluorescence rise profile

The fluorescence enhancement is intimately associated with surface structure of Klarite, e.g. the rough surface, pyramid structures and the randomly spread gold nanoparticles as shown in SEM image of Klarite substrate, which help create abundant curvature and produce the localized plasmon. Those induce a modification on photonic mode density in vicinity of the emitter molecules. This surface characteristics provides advantages over a flat metal surface; the multi photonic modes will more efficiently

increases the near-field coupling between fluorophore molecules and surface plasmon. The strong coupling between the fluorophore and local plasmon explain the enhanced fluorescence quickly decay to the baseline during several picoseconds.

The enhancement is not related to the dimension of the pyramids. The dimensions of pyramids are in the micron scale which cannot produce the localized plasmon as the metallic nanostructures do, but the existence of pyramids provides more surface area, curvature and high light-scattering properties.

6.2.4.3 Dependence of the fluorescence enhancement on the film thickness

In order to see the distance dependence of radiative and electron transfer process on Klarite, similarly we measured the fluorescence dynamics of varying thickness P3HT on it. The film thickness of 5 layers is approximately 10 nm as shown in Figure 6-15. For the 2 layers film its thickness is estimated ~5 nm. The sample with 2 layers P3HT does not show the emission decay due to the strong fluorescence quenching. The 4 layers sample displays the enhanced fluorescence intensity and fast decay. The fluorescence dynamics results on different thickness film demonstrate again that the competition between radiative and electron transfer process, which shows different distance dependence of two processes.

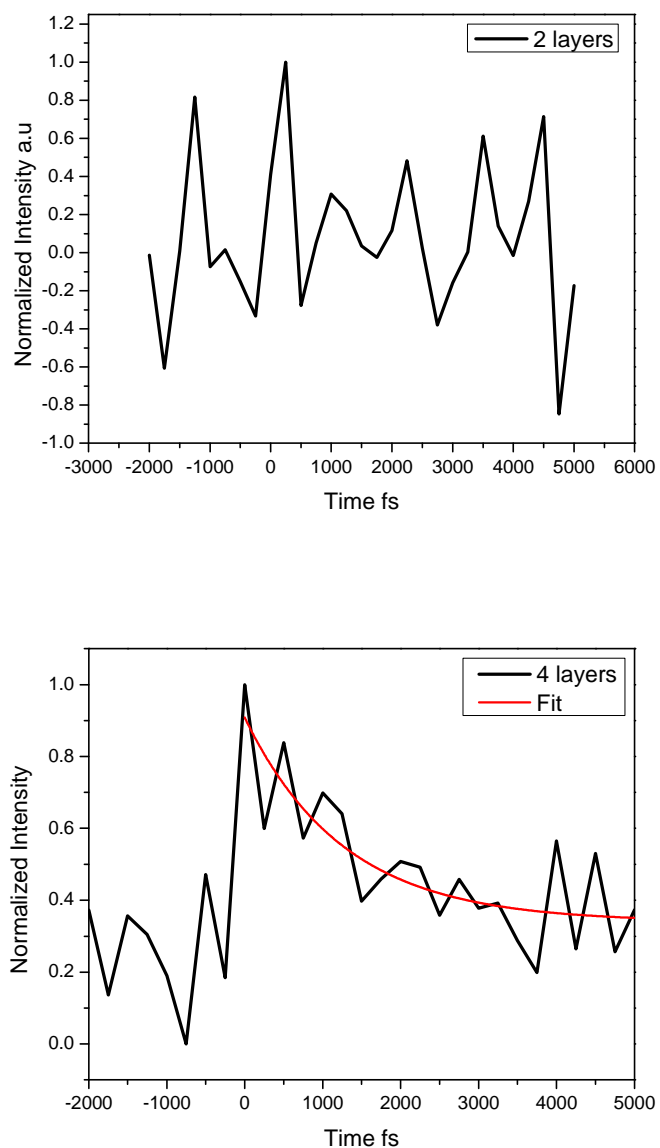


Figure 6-17. Fluorescence decay profiles of various P3HT films on Klarite.

Table 6-7. Time constant of 4 layers P3HT film

	A	τ (ps)	y_0
4 layers	0.76 ± 0.12	1.27 ± 0.53	0.12 ± 0.08

6.2.4.4 Time-resolved fluorescence spectra of P3HT film on Klarite

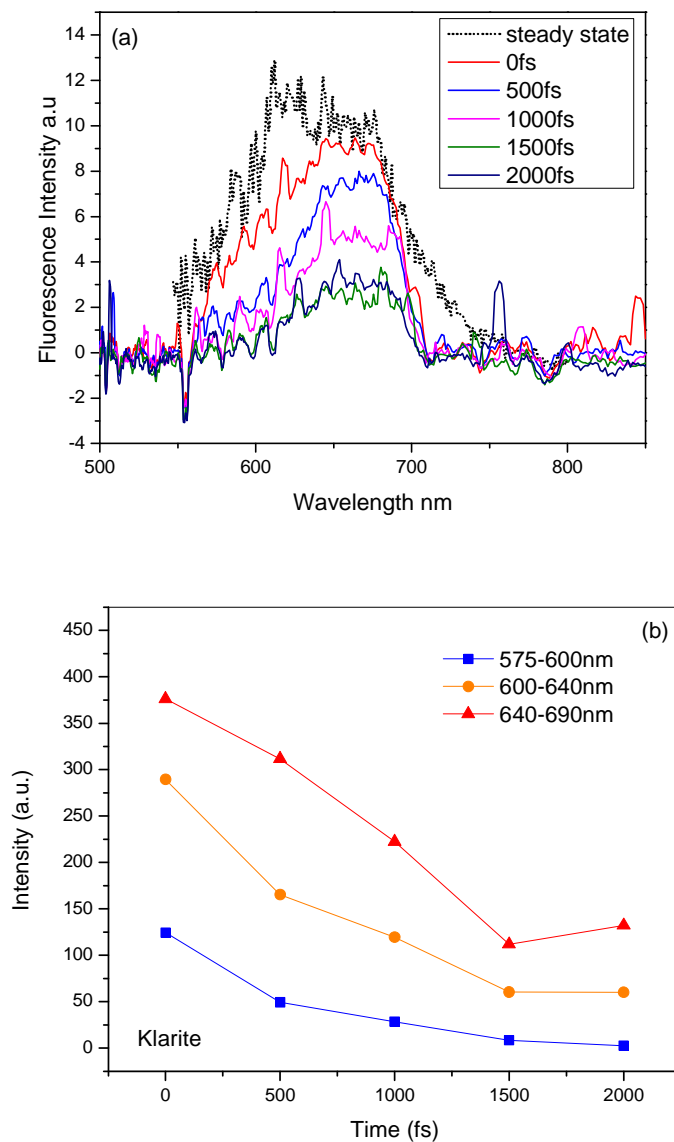


Figure 6-18. (a) Time-resolved fluorescence spectrum of P3HT on Klarite at different times; (b) the decay kinetics based on the emission spectra

Table 6-8. Fluorescence kinetics of P3HT film on Klarite

	0-0.5 ps	0.5-1.5 ps	> 1.5 ps
Intensity change 640-690 nm	375-313 (16.5 %)	313-125 (50.1%)	33.4%
Intensity change 600-640 nm	288-162 (43.8%)	162-63(34.4%)	21.8%
Intensity change 575-600 nm	125-50 (60%)	50-25(20%)	20%

The time-resolved fluorescence spectrum shows a broad emission band with a maximum at 655 nm assigned to 0-1 transition of C=C stretching vibration, which has a similar shape as P3HT film on silica. At time zero, the fluorescence spectrum shows almost the same emission intensity at 640-690 nm range, and the shape of the emission spectrum formed during ~1 ps is a little slower than the fluorescence evolution of film with Au NCs present. In order to study the emission decay rate at different wavelengths, we divided the fluorescence spectrum into three wavelength ranges (575-600 nm, 600-640 nm and 640-690 nm) and the fluorescence kinetics was obtained by plotting the integrated intensity versus time.

The kinetics plotted during 2 ps suggests that at least two time components exist. This is consistent with the fluorescence time profile results and they both show a ~80% intensity decrease within 2 ps. The emission spectrum at different times provides information on the exciton behavior at different wavelengths and the evolution of the spectrum shape. Those emission intensities and decay rates at corresponding wavelength ranges allow us to analyze the wavelength dependence of fluorescence enhancement on Klarite.

The three kinetics traces give a similar trend at the first glance, while with a careful comparison we can see the 640-690 nm and 600-640 nm traces exhibit three time-dependent progressions, a fast decay during early 500 fs and a little slower process from 500 to 1500 fs, then an even slow stage after 1500 fs. For the 640-690 nm trace the slope increased after 0.5 ps and its slopes changed only a little bit within 1.5 ps. The processes occurring in the earliest 0.5 ps may be related to the electron transfer and direct electron-hole recombination. During 0.5-1.5 ps vibration relaxation, exciton localization and exciton hopping may be involved and the following exciton recombination is assigned to the decay after 1.5 ps. The wavelength dependence of emission intensity change with time reflects Klarite enhancement at different wavelenths as shown in Table 6-6. During earliest 0.5 ps the amplitude decreased ~60% of original intensity at 575-600 nm area, while it just decreased 16.5% for 640-690 nm. The following 0.5 to 1.5 ps the amplitude changes account for 20 and 50.1% for 575-600 and 640-690 nm, respectively. The different emission intensity changes among two wavelength ranges demonstrate the fluorescence is more enhanced at higher frequencies.

The time-resolved fluorescence spectra on different substrates reflected the influence of surrounding environment on fluorophore emission. In contrast to Klarite, the emission of the P3HT film with Au NCs presence has been more strongly enhanced at long wavelengths.

6.2.4.5 Time-resolved fluorescence images

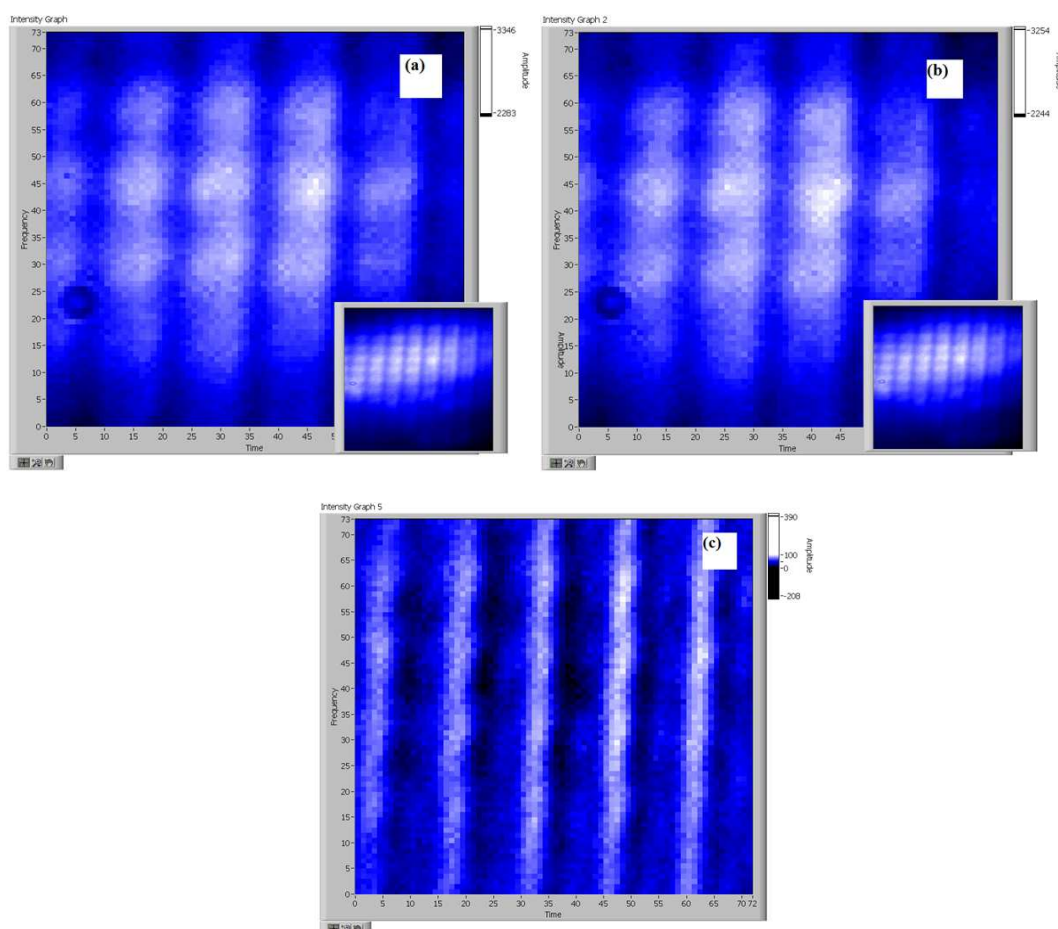


Figure 6-19. The microscope image of P3HT on Klarite at time: (a) 0 ps; (b) 2 ps and (c) the difference image

The spatial resolution of our fluorescence microscope is $0.5\ \mu\text{m}$, we can clearly observe the patterns on Klarite from the focusing image which is the inset of Figure 6-19 a and b. Combination with the high time resolution it offers us the opportunity to observe the emission change at different decay time. The images of P3HT film on Klarite were taken at time zero (Figure 6-19a) and 2 ps (Figure 6-19b) after excitation at 490 nm and exposing for 70 seconds. Figure 6-19c was difference image of a and b image. The amplitude bar locating on top right corner of each image allows us to compare the decay rate from different areas of the substrate. The difference image indicates that a big contrast in decay rate between the pyramids and ridges, which implies that the

fluorescence decay in the pyramids is slower than at the ridges. This result can be explained by the plasmonic nanoantenna. The width of the ridge is approximately 400 nm, and the ridge surface has an angle with the facet of the pyramids, so it is plausible that the edges work as an electric field antenna. The surface plasmon around the “antenna” is stronger than that within the pyramids, and the fluorescence of P3HT is more enhanced at these sites. The delayed fluorescence could not result from the pyramid morphology. The ridges are excited 3.33 fs earlier because they are ~ 1 μm above the bottom of the pyramids. For the same reason, the fluorescence from the ridges arises 3.3 fs earlier. Therefore, the overall time difference resulting from the surface topography is ~ 6.7 fs. This time difference is well beyond our system’s resolution of ~ 100 fs.

6.2.4.6 Comparison of enhanced fluorescence on two substrates

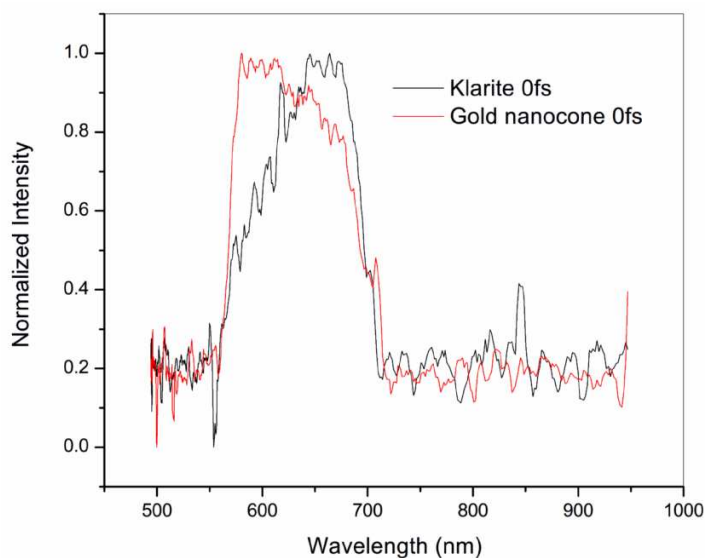


Figure 6-20. Comparison of the emission spectra of P3HT on different substrates.

The two substrates possess unique metallic nanostructures: Klarite surface is composed of 50 nm gold nanoparticles and pyramids pattern, while the silver substrate

prepared from metal evaporation is a relatively flat metal surface, and the gold nanocones oriented on P3HT film provide the localized surface plasmon. The surface plasmon properties are directly associated with the substrates.

Both gold nanostructures show fluorescence enhancement effects. The enhanced fluorescence exhibits different features due to the varying local electric field or the local surface plasmon resonance experienced by the fluorophore molecule. The surface plasmon resonance is very sensitive to the shape and size of novel metal nanostructure on the substrate. The first pronounced difference in the P3HT fluorescence spectrum of the two metallic substrates is their maximum emission band as shown in Figure 6-20. The maximum emission is ~ 600 nm for P3HT film with gold NCs, while the highest emission is around 660 nm for P3HT film on Klarite. In addition, the fluorescence spectrum from the former substrate shows 25 nm blue shift in comparison with the steady state fluorescence spectrum.

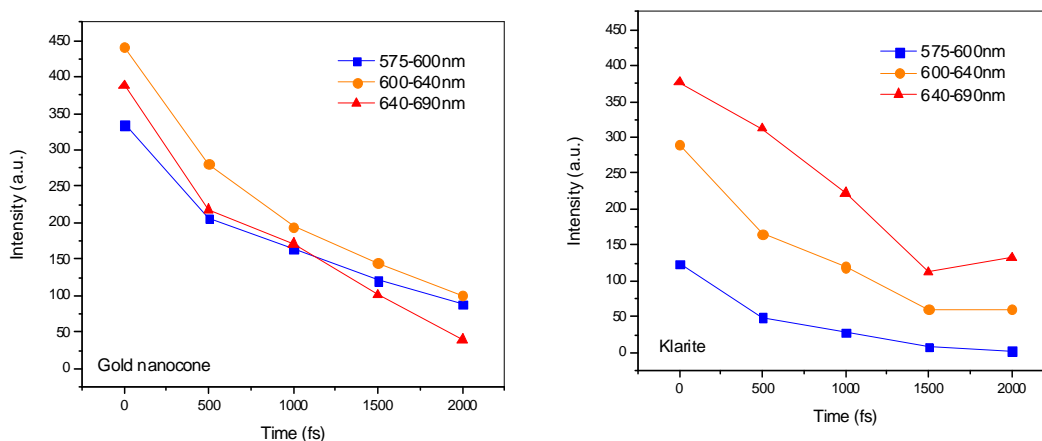


Figure 6-21. Comparison of fluorescence kinetics of P3HT film on: (a) silver and (b) Klarite

A second difference can be seen from the time-dependent fluorescence decay kinetics, i.e. the integrated emission intensity and decay rate. Gold NC/P3HT/Ag exhibits stronger

fluorescence and faster decay than that on Klarite in whole spectrum range. The possible reason for this could be from the different surface plasmon resonance.

Conclusion:

In this chapter we have discussed the factors that affect the fluorescence enhancement of P3HT film, such as different nanostructures, surroundings and the thickness of P3HT film. Through measuring the fluorescence dynamics and the time-resolved fluorescence spectra we observed the enhanced fluorescence intensity and reduced fluorescence lifetime on both metallic substrates. At same time, the fluorescence also exhibits different features from two different substrates, the introduction of gold nanocones strongly modified the excited state decay rate and the emission spectrum as a result of fast-dynamics SEF regime. The fluorescence dynamics of various thickness films with gold nanocones help us confirm the quenching process plays a big role in emission decay. In contrast to gold NC/P3HT/Ag, film on Klarite displays a maximum emission around 650 nm, and the quenching is the dominant process when only two layers of P3HT on it. These results are associated with the different surface morphologies or the nanostructures. The enhanced fluorescence intensity from the Klarite is attributed to the rich curvature originating from its rough surface; however, the shape of gold NC provides multiple surface plasmon modes which enhances the fluorescence decay even more.

References

1. Purcell, E.M., *Spontaneous emission probabilities at radio frequencies*. Physical Review, 1946. **69**: p. 681.
2. Zhao, J., et al., *Interaction of plasmon and molecular resonances for rhodamine 6G adsorbed on silver nanoparticles*. Journal of the American Chemical Society, 2007. **129**(24): p. 7647-7656.
3. Sarkar, S., et al., *Giant Increase in the Metal-Enhanced Fluorescence of Organic Molecules in Nanoporous Alumina Templates and Large Molecule-Specific Red/Blue-Shift of the Fluorescence Peak*. Nano Letters, 2014. **14**(10): p. 5973-5978.
4. Ni, W., et al., *Coupling between molecular and plasmonic resonances in freestanding dye– gold nanorod hybrid nanostructures*. Journal of the American Chemical Society, 2008. **130**(21): p. 6692-6693.
5. Weiss, S., *Fluorescence spectroscopy of single biomolecules*. Science, 1999. **283**(5408): p. 1676-1683.
6. Cook, S., A. Furube, and R. Katoh, *Analysis of the excited states of regioregular polythiophene P3HT*. Energy Environ. Sci., 2008. **1**(2): p. 294-299.
7. Banerji, N., et al., *Ultrafast Relaxation of the Poly(3-hexylthiophene) Emission Spectrum*. The Journal of Physical Chemistry C, 2011. **115**(19): p. 9726-9739.
8. Le Ru, E., et al., *Mechanisms of spectral profile modification in surface-enhanced fluorescence*. The Journal of Physical Chemistry C, 2007. **111**(44): p. 16076-16079.

9. Yu, B., et al., *Light-management in ultra-thin polythiophene films using plasmonic monopole nanoantennas*. Applied Physics Letters, 2012. **101**(15): p. 151106.
10. Mohammadi, A., V. Sandoghdar, and M. Agio, *Gold nanorods and nanospheroids for enhancing spontaneous emission*. New Journal of Physics, 2008. **10**(10): p. 105015.
11. O'Carroll, D.M., C.E. Hofmann, and H.A. Atwater, *Conjugated polymer/metal nanowire heterostructure plasmonic antennas*. Advanced Materials, 2010. **22**(11): p. 1223-1227.
12. Jain, P.K. and M.A. El-Sayed, *Plasmonic coupling in noble metal nanostructures*. Chemical Physics Letters, 2010. **487**(4): p. 153-164.
13. Schuck, P., et al., *Improving the mismatch between light and nanoscale objects with gold bowtie nanoantennas*. Physical Review Letters, 2005. **94**(1): p. 017402.
14. Halas, N.J., et al., *Plasmons in strongly coupled metallic nanostructures*. Chemical Reviews, 2011. **111**(6): p. 3913-3961.
15. Taminiau, T., et al., *Optical antennas direct single-molecule emission*. Nature Photonics, 2008. **2**(4): p. 234-237.
16. Reineck, P., et al., *Distance and wavelength dependent quenching of molecular fluorescence by Au@ SiO₂ core-shell nanoparticles*. ACS nano, 2013. **7**(8): p. 6636-6648.
17. Bharadwaj, P. and L. Novotny, *Spectral dependence of single molecule fluorescence enhancement*. Optics Express, 2007. **15**(21): p. 14266-14274.

18. Lakowicz, J. and Y. Fu, *Modification of single molecule fluorescence near metallic nanostructures*. Laser & Photonics Reviews, 2009. **3**(1 - 2): p. 221-232.
19. Anger, P., P. Bharadwaj, and L. Novotny, *Enhancement and quenching of single-molecule fluorescence*. Physical Review Letters, 2006. **96**(11): p. 113002.
20. Dulkeith, E., et al., *Fluorescence quenching of dye molecules near gold nanoparticles: radiative and nonradiative effects*. Physical Review Letters, 2002. **89**(20): p. 203002.
21. Dulkeith, E., et al., *Gold nanoparticles quench fluorescence by phase induced radiative rate suppression*. Nano Letters, 2005. **5**(4): p. 585-589.
22. Marocico, C.A. and J. Knoester, *Effect of surface-plasmon polaritons on spontaneous emission and intermolecular energy-transfer rates in multilayered geometries*. Physical Review A, 2011. **84**(5).
23. Chung, H.Y., P.T. Leung, and D.P. Tsai, *Enhanced Intermolecular Energy Transfer in the Vicinity of a Plasmonic Nanorice*. Plasmonics, 2010. **5**(4): p. 363-368.
24. Kucherenko, M.G., T.M. Chmereva, and D.A. Kislov, *Energy transfer in molecular systems at the surface of metal solids and nanoparticles*. High Energy Chemistry, 2010. **43**(7): p. 587-591.
25. Yu, Y.-C., et al., *Plasmon-mediated resonance energy transfer by metallic nanorods*. Nanoscale research letters, 2013. **8**(1): p. 1-7.
26. May, V., J. Megow, and I. Zelinskyi. *Excitation energy transfer in molecular complexes: transport processes, optical properties and effects of nearby placed*

- metal nano-particles*. in *SPIE Photonics Europe*. 2012: International Society for Optics and Photonics.
27. Bingi, J., et al., *Plasmonically Tunable Blue-Shifted Emission from Coumarin 153 in Ag Nanostructure Random Media: A Demonstration of Fast Dynamic Surface-Enhanced Fluorescence*. Plasmonics, 2013. **9**(2): p. 349-355.
 28. Itoh, T., et al., *Excitation laser energy dependence of surface-enhanced fluorescence showing plasmon-induced ultrafast electronic dynamics in dye molecules*. Physical Review B, 2013. **87**(23): p. 235408.
 29. Ringler, M., et al., *Shaping emission spectra of fluorescent molecules with single plasmonic nanoresonators*. Physical Review Letters, 2008. **100**(20): p. 203002.
 30. Zhao, L., et al., *Plasmon-induced modulation of the emission spectra of the fluorescent molecules near gold nanorods*. Nanoscale, 2011. **3**(9): p. 3849-3859.